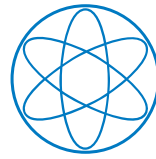Technische Universität München   Physik Department   MPQ

Photon-Mediated Quantum Information Processing with Neutral Atoms in an Optical Cavity

Stephan T. Welte

Dissertation

Technische Universität München

Max-Planck-Institut für Quantenoptik

Photon-Mediated Quantum Information Processing with Neutral Atoms in an Optical Cavity

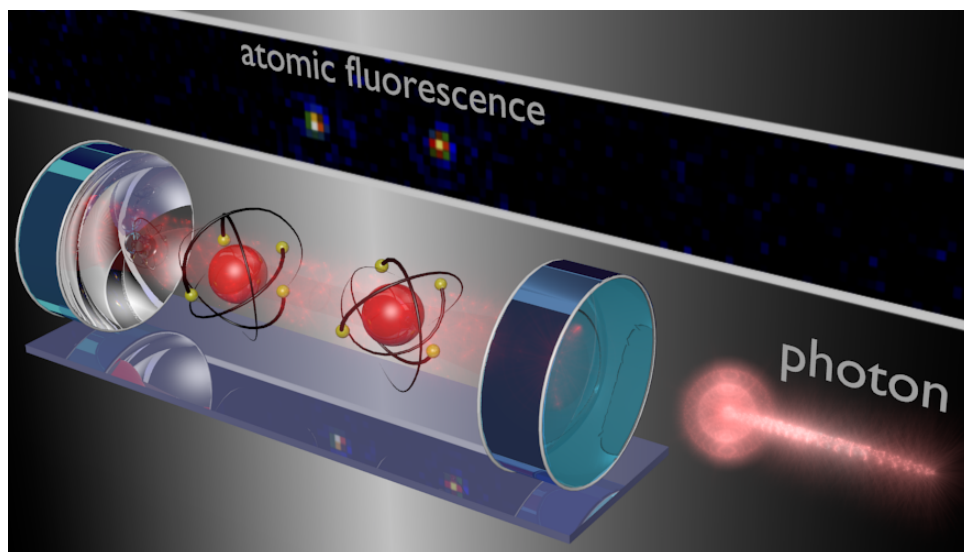## Stephan T. Welte

Vollständiger Abdruck der von der Fakultät für Physik der Technischen Universität München zur Erlangung des akademischen Grades eines

Doktors der Naturwissenschaften (Dr. rer. nat.)

genehmigten Dissertation.

Vorsitzender :   Univ.-Prof. Dr. Wilhelm Zwerger

Prüfer der Dissertation :   1. Hon.-Prof. Dr. Gerhard Rempe
                           2. Univ.-Prof. Jonathan J. Finley, Ph.D.

Die Dissertation wurde am 18.04.2019 bei der Technischen Universität München eingereicht und durch die Fakultät für Physik am 09.09.2019 angenommen.

Abstract

Neutral atoms coupled to optical cavities constitute a promising platform for the realization of a quantum network. Local processing of quantum information in the nodes of such a network is a challenging task and requires the controlled coupling of several stationary matter qubits trapped inside the same cavity. This coupling allows for the experimental implementation of quantum logic gates, the basic building blocks of a quantum computer. In this thesis, two techniques to simultaneously couple two neutral atoms inside one cavity will be presented. Both techniques rely on the reflection of light pulses from the atom-atom-cavity system. The underlying coupling mechanism relies on a naturally occuring phase shift that depends on the states of the two atoms as well as the polarization state of the reflected light. The first technique, dubbed *quantum state carving*, allows for the generation of maximally entangled states employing an inherently probabilistic and heralded protocol. The protocol requires the reflection of two light pulses in succession. Two projective measurements remove undesired parts of the atom-atom state until a maximally entangled state is eventually generated. The second technique allows for the implementation of a universal deterministic quantum gate between the two atoms that is triggered via the reflection of a single photon. The gate mechanism does not rely on the spatial distance between the two atoms as long as they strongly couple to the cavity mode. It is furthermore platform independent and could be implemented with other types of logical qubits in cavities. In future applications, the gate can be applied in an entanglement swapping protocol in a quantum repeater.

Kurzfassung

Neutralatome in optischen Resonatoren stellen eine vielversprechende Plattform für den Bau von Quantennetzwerken dar. Die lokale Verarbeitung von Quanteninformation in den Knoten eines solchen Netzwerks ist eine Herausforderung und setzt die kontrollierte Kopplung mehrerer stationärer Qubits, die in einem Resonator gefangen sind, voraus. Diese Kopplung ermöglicht die experimentelle Realisierung von Quantenlogikgattern, den Grundbausteinen eines Quantencomputers. In dieser Arbeit werden zwei Methoden für die simultane Kopplung zweier Neutralatome in einem Resonator vorgestellt. Beide Techniken beruhen auf der Reflexion von Photonen am Resonator, der die Atome enthält. Der Kopplungsmechanismus beruht auf einem natürlich auftretenden Phasenschub-Mechanismus, der von den Zuständen der zwei Atome und der Polarisation des reflektierten Lichts abhängt. Die erste Technik, auch *Quantum state carving* genannt, ermöglicht die Erzeugung maximal verschränkter Zustände mittels eines probabilistischen und angekündigten Protokolls. Das Protokoll beruht auf der aufeinanderfolgenden Reflexion zweier optischer Pulse. Zwei projektive Messungen entfernen ungewünschte Anteile des Zustands bis ein maximal verschränkter Zustand erzeugt ist. Die zweite Methode ermöglicht die experimentelle Realisierung eines universellen, deterministischen Atom-Atom-Quantengatters, das durch die Reflexion eines einzelnen Photons ausgeführt wird. Der Gattermechanismus hängt nicht vom räumlichen Abstand der beiden Atome ab, solange diese stark an die Resonatormode koppeln. Er ist weiterhin unabhängig von der verwendeten experimentellen Plattform

und könnte mit anderen Implementierungen logischer Qubits durchgeführt werden. In zukünftigen Anwendungen kann das Gatter in einem *entanglement swapping* Protokoll in einem Quantenrepeater verwendet werden.

List of Publications

- A photon-photon quantum gate based on a single atom in an optical resonator
B. Hacker*, S. Welte*, G. Rempe, S. Ritter
Nature **536**, 193-196 (2016).

- Recheneinheit für zwei Photonen
S. Ritter, B. Hacker, S. Welte, G. Rempe
Physik in unserer Zeit **47 (6)**, 268-269 (2016).

- Cavity Carving of Atomic Bell States
S. Welte*, B. Hacker*, S. Daiss, S. Ritter, G. Rempe
Physical Review Letters **118**, 210503 (2017).

- Photon-Mediated Quantum Gate between Two Neutral Atoms in an Optical Cavity
S. Welte, B. Hacker, S. Daiss, S. Ritter, G. Rempe
Physical Review X **8**, 011018 (2018).

- Deterministic creation of entangled atom-light Schrödinger-cat states
B. Hacker, S. Welte, S. Daiss, A. Shaukat, S. Ritter, L. Li, G. Rempe
Nature Photonics **13**, 110-115 (2019).

- Single-Photon Distillation via a Photonic Parity Measurement Using Cavity QED
S. Daiss, S. Welte, B. Hacker, L. Li, G. Rempe
Physical Review Letters **122**, 133603 (2019).

Contents

1. Introduction

The turn of the 20$^{\text{th}}$ century marked the starting point for the development of quantum theory. In 1900, Max Planck formulated the law of black-body radiation assuming a model of quantized energy exchange between an idealized black body and an electromagnetic radiation field in thermal equilibrium [1]. In the following decades, quantum theory was developed further and questioned by influential physicists like Bohr [2], de Broglie [3], Einstein [4], Heisenberg [5], Schrödinger [6] and many others. In various cases, these physicists envisioned gedanken experiments like the Schrödinger cat experiment [6] without the possibilities of performing such experiments in the laboratory with single particles like atoms and photons. In fact, Schrödinger wrote in 1952: '*...we never experiment with just one electron or atom or (small) molecule. In thought-experiments we sometimes assume that we do; this invariably entails ridiculous consequences...*' [7]. New tools were needed to perform the gedanken experiments devised by the founding fathers of quantum mechanics. A prime example for such a new tool is the laser, which was invented by Theodore Maiman in 1960 [8] and allowed to perform a variety of novel experiments. Nowadays, the laser with all its different practical implementations has far-reaching applications in everyday life.

In the decades following Maiman's invention, it was demonstrated that single charged atomic ions could be stored in traps, manipulated with laser light and observed with a camera [9]. The rapid development of the trapped ion experiments [10] later even allowed for the observation of quantum jumps as envisioned by Bohr [11, 12]. In contrast to Schrödinger's view [7], results like these showed that it was indeed possible to isolate and manipulate single quantum particles. Around the same time, experimental physicists also began to study the interaction of single photons with single neutral atoms. Microwave photons were stored in a high-quality resonator while highly excited atoms in Rydberg states flew through the resonator and interacted with the photons for tens of microseconds [13]. Landmark experiments like the collapse and revival in a one-atom maser [14] or the study of decoherence of a Schrödinger-cat state [15] could be performed. Parallel to these developments the trapping and cooling of neutral atoms was investigated. It was observed that atomic clouds, illuminated with properly tailored laser light, could reach extremely low temperatures. The magneto-optical trap (MOT) was invented, and the necessary cooling mechanisms were subject to extensive theoretical and experimental analysis [16–19]. Although initially applied to atomic ensembles, these techniques were later employed for trapping and cooling of a single neutral atom in a high-finesse optical cavity for macroscopic timescales of several seconds [20].

Early in the 1980s, when many groups around the world were working on the control and the manipulation of ions, atoms and photons, the parallel development of a new research field called *quantum computation* was pushed forward by physicists around Feynman [21]

and Deutsch [22]. It was found that a well controlled quantum system, dubbed *quantum computer*, could theoretically be employed to perform special computation and simulation tasks faster than a classical computer. In the 1990s mathematicians and theoretical physicists began to explore the potential software running on an envisioned quantum computer. First quantum algorithms for the prime factorization of large numbers [23] and the effective search of large databases [24] were developed by Shor and Grover, respectively. For the experimental implementation of these algorithms, elementary logic operations, namely *quantum gates* are necessary. Cirac and Zoller realized that properly controlled trapped ions could potentially be used as quantum bits (qubits) and their collective motion could be employed as a bus to perform the required quantum logic operations. This insight led to the first proposals to perform quantum gates tailored for the trapped ion platform [25, 26]. These ideas were implemented only a few years afterwards [27–29] and offered the possibility to explore the potential of quantum computing in the laboratory [30]. Other experimental platforms like superconducting qubits [31, 32], optical photons [33–37], nitrogen-vacancy centers [38] and neutral atoms [39, 40] followed in quick succession and realized novel techniques to perform quantum gates for quantum information processing (QIP).

To qualify as a proper platform for quantum computation, any possible candidate system must fulfill the five criteria formulated by DiVincenco [41]. These criteria comprise: A scalable system, the ability to perform qubit initialization and readout, the availability of a universal set of quantum gates, and long coherence times compared to the operation time of the quantum gates. DiVincenco defined two further criteria necessary for quantum communication in a quantum network. These criteria are the ability to interconvert stationary to flying qubits and the ability to transmit the flying qubits to a specified location [41]. The experiments reported in this thesis [42, 43] are located in the field of quantum computation. They show how two atomic qubits trapped in an optical cavity can be initialized in their ground states, read out simultaneously, and how a novel mechanism can be employed to achieve both a universal gate operation and entanglement generation between them. The gate operation time is two orders of magnitude faster than the coherence time of the qubits. The fact that the employed atoms are addressed globally in this work is a technical limitation that can be overcome in the future with an addressing system as already demonstrated in the same experimental platform [44] for a different purpose. The results achieved in this thesis therefore show that neutral atoms trapped in an optical cavity represent a promising platform for quantum computation in the spirit of the DiVincenco criteria. Additionally, the system has the potential to be embedded into a quantum network as the demonstrated atom-atom gate is executed via the reflection of a single photon propagating in a quantum channel. Recently, it has been demonstrated that neutral atoms in an optical cavity fulfill DiVincenco's criteria for quantum communication [45, 46]. Therefore, this platform is suitable for both local quantum computation and for quantum communication in a network. The presented results have applications in both of these areas of research.

The field of quantum networks was emerging in parallel with the development of small quantum computers. These networks [45, 47] offer a wide variety of applications ranging from quantum key distribution (QKD) [48] and quantum communication [49] to quantum teleportation [50]. Furthermore, distributed quantum computing [51–53] can be realized by connecting small quantum computers via mobile qubits. Such an architecture allows for

overcoming the technical difficulties which arise, when scaling up the number of qubits in a quantum computer [54]. All these fascinating prospects have fuelled the dream to ultimately realize a quantum internet on a global scale [55]. As a preliminary step towards this goal, Chinese scientists launched a satellite into space in August 2016. The satellite allows to distribute entangled photons through the atmosphere and to perform QKD between ground stations in China and Austria [56, 57]. However, the satellite-based approach is not the only way to distribute keys between two remote parties. Fiber-based networks can be implemented and the problem of optical transmission losses can be addressed by employing trusted network nodes between the sender and the receiver [58]. Such a network architecture was recently implemented in China with 32 trusted nodes between the cities of Beijing and Shanghai [59]. Inside a trusted node, projective measurements on the transmitted photons are performed such that classical information in the form of a series of bits is generated. Since classical information can be copied, this architecture of a quantum network is in principle prone to eavesdroppers. Therefore it was envisioned to build a network architecture that exclusively relies on quantum principles [55, 58], like entanglement [60] and quantum teleportation [61], to transmit quantum information via a quantum repeater [62, 63]. A way to implement such pure quantum networks relies on an architecture where stationary memory qubits [64] located in the nodes are connected via quantum channels capable of transferring mobile qubits. These networks can be implemented with quantum technology platforms such as nitrogen-vacancy centers [65, 66], quantum dots [67], ions or neutral atoms [68]. The possibility to coherently manipulate single neutral atoms and to couple them to an optical cavity to constitute a network node makes this system particularly suitable for future long-distance quantum networks with optical photons propagating in the network channels [68]. Over the last years, the atom-cavity platform was developed steadily and a versatile toolbox was established, which comprises basic building blocks for quantum computation and communication applications. The demonstration of a quantum controlled-NOT gate between an optical photon and a single trapped atom in a cavity [69] opened up the possibility to process quantum information in a hybrid system and even transfer the qubit state of the atom onto a flying photon and vice versa [46]. Following this direction of resesearch, a swap gate between a neutral atom coupled to a microsphere resonator and a photonic qubit was realized recently [70] utilizing a single-photon Raman interaction mechanism [71, 72]. All these experiments employed one single atomic qubit coupled to a resonator.

To extend the toolbox already available, it is essential to increase the number of qubits per network node. A multi-qubit node, with the ability to perform local gate operations and the connection to a quantum channel, would allow for distributed quantum computing [51–53]. The result of a local quantum computation inside a network node could be mapped onto photonic qubits [46] and transferred to a different node where further processing could be performed. Multi-qubit network nodes also play an important role in the ongoing effort to build a quantum repeater [62]. Here, it is necessary to implement quantum repeater stations between two remote network nodes as transmission losses hamper the direct distribution of entangled photons and the no-cloning theorem [73] forbids the amplification of quantum information. Therefore, it was suggested to build quantum repeater stations made of a cavity containing two qubits [74]. To generate entanglement between two qubits in remote nodes, the repeater station is placed halfway between the remote nodes. In an initial step, entanglement between one of the remote qubits and one qubit in the repeater station is

generated. Furthermore, entanglement is generated between the remaining remote qubit and the other qubit in the repeater station. Once these steps are completed, entanglement swapping can be performed. The application of single-qubit rotations in combination with a two-qubit quantum gate at the repeater station facilitates the generation of entanglement between the two remote qubits, a prerequisite for quantum teleportation. Such an intracavity two-qubit quantum gate suitable for entanglement swapping was proposed early on [75, 76].

The experiments described in this thesis demonstrate the implementation of a network node containing two atomic qubits and the experimental realization of the photon-mediated atom-atom gate mechanism proposed in [75, 76]. It is demonstrated that quantum information can be processed locally in a two-qubit node that has a connection to an optical quantum channel. Two-qubit nodes were also investigated in the field of trapped ions. Here, experiments with two intracavity ions have have been performed and entanglement between those ions has been generated in a probabilistic and heralded protocol [77] and with the Mølmer-Sørensen gate [78]. In comparison to these experiments, in this work the interaction mechanism between the two atoms relies on their collective coupling to a common cavity mode in the optical domain. A related idea was employed in the field of superconducting qubits operating in the microwave domain where two transmon qubits were dispersively coupled to the same transmission line resonator [79]. In these experiments, the exchange of virtual photons between the two qubits allowed for the coherent transfer of quantum states.

The common coupling of the two atoms to the optical mode of a Fabry-Pérot resonator is employed in two variations in this thesis. It is used for the generation of entanglement and furthermore for the implementation of a quantum gate without the necessity of individual atom addressing. The investigated coupling methods both rely on the reflection of optical pulses from the atom-atom-cavity system. The first method, dubbed *quantum state carving*, performs projective measurements on the two-atom state to generate the entanglement in a probabilistic and heralded way. Quantum state carving with two atoms in a cavity was proposed theoretically in 2003 [80] and is realized experimentally in this work. The second method describes a deterministic universal quantum gate executed by the reflection of a single photon.

The thesis is outlined as follows: In chapter 2, the experimental platform with neutral atoms in the optical cavity is presented. In this chapter the necessary toolbox for atom trapping, cooling, the manipulation of the internal electronic degrees of freedom and the state detection is introduced. These tools are applied in chapter 3 to outline the technique of quantum state carving. Experimental results as well as limitations for the obtained fidelities and efficiencies are presented and discussed in detail. In chapter 4, the atom-atom quantum gate is presented. Results characterizing the gate performance as well as the experimental error budget are discussed.

2. Atom-Cavity System for Quantum Gate Applications

2.1. Theory: Tavis-Cummings Hamiltonian

The experiments described in this thesis were performed with a high-finesse cavity setup that will be described in this chapter. The Hamiltonian modelling the coupling of an atom to a single mode of an optical cavity was formulated in the Jaynes-Cummings model [81]. After application of the rotating wave approximation, the Hamiltonian in the Schrödinger picture can be written in the form

$$
\begin{aligned}
H_{\mathrm{JC}} &= H_{\mathrm{a}} + H_{\mathrm{c}} + H_{\mathrm{int}} \\
&= \hbar\omega_a\sigma^+\sigma^- + \hbar\omega_c a^\dagger a + \hbar g(a\sigma^+ + a^\dagger\sigma^-)
\end{aligned}
\tag{2.1}
$$

where ω_c is the frequency of the optical field. The field annihilation and creation operators are denoted as a and $a^\dagger$, respectively. The operators $\sigma^+ = |e\rangle\langle g|$ and $\sigma^- = |g\rangle\langle e|$ are the creation and annihilation operators of internal atomic excitations and ω_a is the atomic transition frequency. The Hamiltonian consists of three terms. The first term H_a describes the energy stored in atomic excitations. The second term H_c describes the energy stored in the optical cavity field. The third term H_{int} describes the interaction between the atom and the cavity field. If the interaction is switched on, energy can coherently be exchanged between the atom and the cavity mode. Half the rate describing this energy exchange is denoted by g, the atom-cavity coupling strength.

The Jaynes-Cummings Hamiltonian is a powerful tool of cavity quantum electrodynamics (QED) that can predict a number of phenomena which have also been observed experimentally. These phenomena include Rabi oscillations in the coupled system and the existence of discrete energy levels with an energy spacing that scales with the square root of the number of quanta in the system, the Jaynes-Cummings ladder. This square root behavior is a fundamental property allowing for the observation of the photon blockade effect in optical cavities [82–84]. Furthermore, the phenomenon of collapse and revival, where a cavity mode is initially populated with a Poissonian or Bose-Einstein photon number statistics is predicted by the Jaynes-Cummings Hamiltonian. This feature was observed with Rydberg atoms coupled to a superconducing microwave cavity [14].

The Jaynes-Cummings Hamiltonian can be extended to the Tavis-Cummings Hamiltonian describing $N > 1$ identical atoms coupled to the same cavity mode [85]. In the Schrödinger picture, this Hamiltonian can be written as

$$
H_{\mathrm{TC}} = \hbar\omega_a \sum_{i=1}^{N} \sigma_i^+\sigma_i^- + \hbar\omega_c a^\dagger a + \hbar \sum_{i=1}^{N} g_i(a\sigma_i^+ + a^\dagger\sigma_i^-).
\tag{2.2}
$$

The interaction part of the Tavis-Cummings Hamiltonian can be rewritten in the form $H_{\mathrm{TC}} = \hbar \sum_{i=1}^{N} |g_i| (\sigma_i^+ e^{i\phi_i} a + \sigma_i^- e^{-i\phi_i} a^\dagger)$. The sum in the Tavis-Cummings Hamiltonian is performed over all atoms in the cavity mode. The coupling strength g_i can vary from atom to atom and is described by a complex number with a phase ϕ_i and an absolute value $|g_i|$. In an earlier work from our group [44, 86], the case of two atoms was investigated. It was found that the phase difference $\Delta\phi$ depends on the positions of the atoms in the trapping potential, the wavelength of the trap and the wavelength of the atomic transition. Depending on the respective phase difference, situations of constructive and destructive interference can occur. This phase difference [44, 87] cannot be observed with a laser that probes the interaction of the atoms with the cavity mode via a cavity transmission or reflection measurement. Both for the case of an odd and an even number of trapping sites between the two atoms, they will align in the same way with respect to the local electric field. Neuzner points out [44] that in this case, the phase terms $e^{i\phi_i}$ can be removed with a gauge transformation. Only by probing the atoms with a transversal laser beam, the phase difference can be accessed. The probing of an atom pair with a transversal laser for fluorescence state detection will be investigated in section 2.4.3.2.

In this thesis, an atom pair ($N = 2$) is trapped quasi-permanently inside an optical Fabry-Pérot cavity [88] with a mirror distance of 486 μm. The cavity is stabilized with a Pound-Drever-Hall locking scheme [89] using a 771 nm laser beam. The purpose of this laser beam is twofold. On the one hand, it is employed to stabilize the cavity length via a measurement of the transmitted signal and an active feedback on a piezo tube that controls the cavity length. On the other hand, it serves as a blue-detuned repulsive trapping potential for the atoms. It has a different wavelength than the cavity mode and the atomic transition wavelength at 780 nm. An additional beam with laser light of this wavelength is also transmitted through the cavity. The 780 nm light will address the D_2 line of the employed rubidium atoms (^{87}Rb). The two beams form a spatially varying beating pattern inside the resonator. At the center of the cavity, a node of the 771 nm laser coincides with an antinode of the 780 nm laser. At this point, the blue-detuned 771 nm trap confines the atoms at the point of maximal coupling strength g between the atom and the cavity. If the atom is moved along the cavity axis, it can be trapped at any node of the 771 nm beam. Due to the beating pattern, a spatial position exists which is 16.2 μm away from the cavity center, where two nodes of both laser fields overlap. Here, the coupling strength assumes a minimum. To achieve the highest possible coupling strength, the atoms should therefore be trapped as close as possible to the center of the cavity mode.

For the implementation of a two-qubit gate it is necessary to trap a pair of atoms in the cavity mode. According to the Tavis-Cummings model, the exchange rate of energy between the atoms and the cavity increases with $\sqrt{N}$ where N is the number of coupling atoms inside the cavity mode. To explain this scaling property, consider the situation where a single excitation E is present in a coupled system of an ensemble of N atoms and a cavity [90]. The excitation can be transferred between the ensemble and the cavity field. As an initial boundary condition, one may assume that the excitation is initially stored in the cavity field. The atoms are considered as two-level systems consisting of the ground state $|g\rangle$ and the excited state $|e\rangle$ while the cavity is tuned into resonance with this

transition. The combined atom-light state where all the atoms initially occupy the ground state g can be written as

$$|E = 1\rangle_{N,cav} = |g_1,...,g_N\rangle\,|1\rangle_{cav}\,. \tag{2.3}$$

On the other hand, if the excitation is initially stored in one of the atoms, the combined state becomes

$$|E = 1\rangle_{N,\text{ensemble}} = |E_N\rangle\,|0\rangle_{cav} \tag{2.4}$$

where $|E_N\rangle = \frac{1}{\sqrt{N}}(|e,g,...,g\rangle + |g,e,g,...,g\rangle + \cdots + |g,...,g,e\rangle)$. In this situation, the single excitation is stored in one atom out of the ensemble of N atoms, but it is not known in which one. The entangled superposition state $|E_N\rangle$ consisting of all possible combinations is called a Dicke state or W state [91]. The exchange rate $g(N)$ between the atoms and the cavity mode is defined as the matrix element

$$g(N) = \langle E = 1|_{N,\text{ensemble}}\,H_{\text{int}}\,|E = 1\rangle_{N,cav} \tag{2.5}$$

where H_{int} is the interaction term in the Tavis-Cummings Hamiltonian defined in equation 2.2. Evaluating this matrix element yields $g(N) = \sqrt{N}g$. Thus, for an atom pair with $g_1 = g_2 = g$, a total exchange rate of $\sqrt{2}g$ between the atoms and the cavity is expected. The $\sqrt{N}$ behavior of the coupling strength can only be observed if all of the atoms from the ensemble couple equally to the cavity mode. However, the single atom coupling strength $g(\mathbf{r})$ depends on the spatial position $\mathbf{r}$ of the atom in the cavity and can be expressed as

$$g(\mathbf{r}) = \sqrt{\frac{\omega_c}{2\epsilon_0 V\hbar}}\mu_{\text{ge}}\psi_{cav}(\mathbf{r}). \tag{2.6}$$

Here, ω_c is the frequency of the chosen transition, ϵ_0 is the vacuum permittivity and V is the mode volume of the cavity. For a classical Fabry-Pérot cavity, V can be expressed as

$$V = \frac{\pi}{4}w_0^2 \cdot l \tag{2.7}$$

where w_0 denotes the cavity mode waist and l the cavity length. Furthermore, μ_{ge} is the dipole matrix element of the atomic transition. The coupling constant is modulated spatially with the field distribution inside the resonator $\psi_{cav}(\mathbf{r})$. To achieve high values of g, a small mode volume V of the cavity and a high transistion strength are needed. Also, the atoms have to be placed at antinodes of the cavity mode. A way to measure the coupling strength of one or two atoms to the cavity mode will be presented in section 3.4.1.

2.2. Choice of the Atomic Qubit

The implementation of a quantum gate requires the suitable choice of a pair of qubit states. Long-lived ground states are beneficial as this property contributes to the stability of the qubit. The atomic species employed in this thesis is ^{87}Rb, an alkaline metal with one valence electron. A detailed level scheme of the D_2 line of ^{87}Rb is shown in the appendix A. The nuclear spin of $I = 3/2$ couples to the electron spin $S = 1/2$ which gives rise to two hyperfine states $|F = 1\rangle$ and $|F = 2\rangle$ associated with the ground state $5^2S_{1/2}$. Here, F
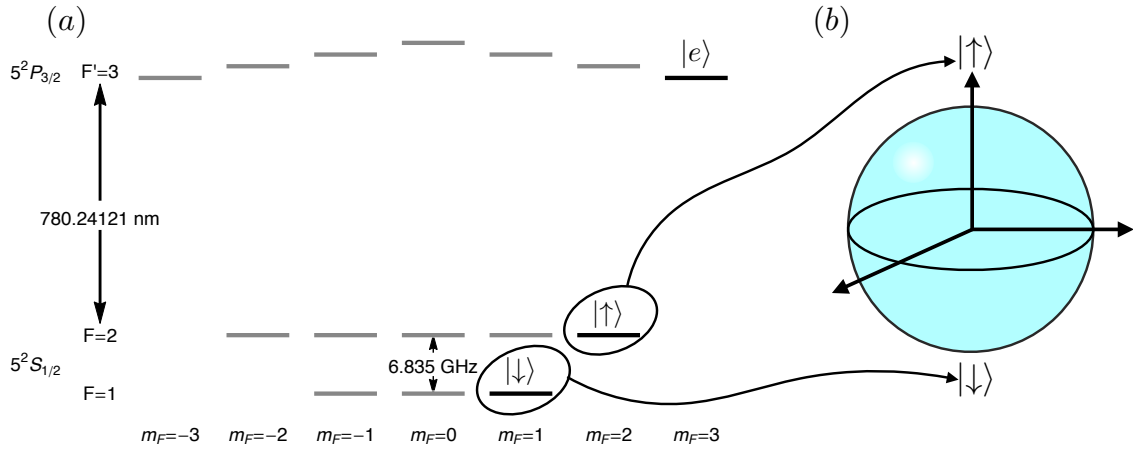
Figure 2.1.: Atomic level structure and Bloch sphere. (a) Level scheme of the employed ^{87}Rb atoms (D_2 line). The F states split into magnetic Zeeman m_F substates. Two of these substates are the qubit basis states $|\uparrow\rangle := |F{=}2, m_F{=}2\rangle$ and $|\downarrow\rangle := |F{=}1, m_F{=}1\rangle$. The excited state $|e\rangle = |F'=3, m_F=3\rangle$ will serve as an additional state that allows to couple the atom in the state $|\uparrow\rangle$ to a resonant cavity mode (see section 2.5). Due to a light shift imprinted by a linearly-polarized red-detuned trapping laser at 1064 nm, the degeneracy of the Zeeman levels in the $|F'=3\rangle$ manifold is lifted [44]. (b) Bloch sphere of the atomic qubit with the state $|\uparrow\rangle$ on the north pole and the state $|\downarrow\rangle$ on the south pole.

denotes the total angular momentum consisting of nuclear spin I, electron spin S and the orbital angular momentum L. Written in a vector notation, the total angular momentum can be expressed as $\mathbf{F} = \mathbf{J} + \mathbf{I}$ where $\mathbf{J} = \mathbf{L} + \mathbf{S}$ is the total angular momentum of the electron [92]. The two hyperfine states $|F = 1\rangle$ and $|F = 2\rangle$ are separated energetically by a microwave transition of 6.835 GHz [92]. Via the application of a magnetic field, the hyperfine state manifolds can be split into $2F + 1$ magnetic Zeeman states with quantum numbers m_F where $-F \leq m_F \leq F$. Two of these Zeeman states, namely $|\uparrow\rangle := |F{=}2, m_F{=}2\rangle$ and $|\downarrow\rangle := |F{=}1, m_F{=}1\rangle$ will serve as the basis states of the logical qubit inscribed in the atoms. The D_2 line of ^{87}Rb with the relevant qubit states is shown in figure 2.1.

The two qubit states are the outermost states in the two respective Zeeman manifolds and thus sensitive to fluctuating magnetic fields. When the magnetic field changes, the qubit transition frequency changes by $3{\times}0.7$ MHz/Gauss [92], three Larmor quanta. The fluctuations of the surrounding magnetic field limit the qubit coherence time to $\approx 200\,\mu$s. As typical experimental protocols have a duration on the order of $10\,\mu$s, the decay of coherence over the employed protocol time is not severe and can be neglected to first order. Circular polarization components of the laser light employed for trapping the atoms would lead to a differential ac-Stark shift of the qubit levels. If the atoms move in the trap, this would lead to a reduction of the coherence time. The circular trap components were carefully eliminated with polarizers and waveplates to minimize this effect [93,94]. Although the employed qubit is susceptible to fluctuating magnetic fields, it has an outstanding advantage. The optical transition from the upper qubit state $|\uparrow\rangle$ to the excited state $|e\rangle := |F' = 3, m_F = 3\rangle$ is a cycling transition and has the highest dipole matrix element of all possible transitions on the D_2 line of ^{87}Rb. This property is beneficial because the atom-cavity coupling rate g linearly depends on this dipole matrix element as can be seen

from equation 2.6. The optical cavity that contains the qubit is tuned to the transition $|\uparrow\rangle \rightarrow |e\rangle$ and therefore the upper qubit state will couple to the cavity via this transition and the highest possible value of g is achieved. As outlined in section 2, the coupling strength g also depends on the position of the atom in the trap. Only when it is trapped exactly at the cavity center, g reaches its maximum. If the qubit is prepared in the state $|\downarrow\rangle$, the atom does not couple to the cavity because it is 6.835 GHz detuned. Thus, the state $|\downarrow\rangle$ can be considered as a non-coupling state while the state $|\uparrow\rangle$ is coupling to the cavity. This property of the chosen qubit is essential for the experiments described in this thesis.

Also, qubit superposition states of $|\uparrow\rangle$ and $|\downarrow\rangle$ can be prepared where the atom is in a coherent superposition of the coupling and the non-coupling state. The preparation of such superposition states can be performed by means of a Raman laser pair as outlined in section 2.4.2.

2.3. Experimental Setup

The cavity employed for the experiments described in this thesis was implemented in the 'QGate' setup in 2009 by Christian Nölleke and Holger Specht [95,96]. A schematic showing the trap configuration and examplary EMCCD pictures of atoms between the cavity mirrors is shown in figure 2.2. It is a high-finesse cavity ($\mathcal{F} \approx 6 \times 10^4$ at $\lambda = 780.24$ nm) comprised of two highly reflecting mirrors with reflectivities R_1=99.99% and R_2=99.9994% with a radius of curvature of $r_M = 5$ cm. The asymmetric character of the cavity allows to outcouple light preferentially in one direction through the mirror with the lower reflectivity. Due to the two different mirror reflectivities, the cavity transmission on resonance is 10.3%. In the case of a symmetric cavity, a transmission of 100% can be achieved. The cavity has a length of $l = 486\,\mu$m. From the radius of curvature of the mirrors r_M and l, the cavity mode waist w_0 can be calculated according to $w_0 = \sqrt{\frac{\lambda l}{\pi}\left(\frac{p_1 p_2(1-p_1 p_2)}{(p_1 + p_2 - 2p_1 p_2)^2}\right)^{1/4}} = 29\,\mu$m where $p_1 = p_2 = 1 - l/r_M$ and $\lambda = 780.24$ nm. The length of the cavity can be controlled by applying a voltage to a piezo tube containing the cavity mirrors. An active cavity length stabilization is achieved with a feedback voltage supplied to the piezo tube in a Pound-Drever-Hall locking technique. The feedback signal is derived from a measurement of the transmission of a diode laser (Toptica TA Pro) at 770.94668 nm through the cavity. The laser itself is frequency stabilized to a frequency comb via a beatlock. For the Pound-Drever-Hall stabilization of the cavity onto the locking laser, sidebands at a frequency of 27.2 MHz are modulated onto the optical beam via a fiber-based electro-optical modulator (EOM). The Pound-Drever-Hall technique allows to lock the cavity with a frequency stability of $\sigma_\nu \approx 0.15$ MHz. The transmission signal oscillates with a characteristic frequency of 10 kHz, the first mechanical mode of the piezo tube used for adjusting the cavity length [93]. The frequency stabilization of the cavity is an important prerequisite for the implementation of the logic gate between two intracavity atoms and for the quantum state carving technique. The phase shift in the atom-atom-light state associated with a reflection of a photon from the cavity depends on the detuning between this photon and the cavity mode and therefore also on the cavity stability. The locking laser is far detuned from the atomic resonance on the D_2 line of ^{87}Rb at 780.24 nm. In the described experiments, the cavity is tuned
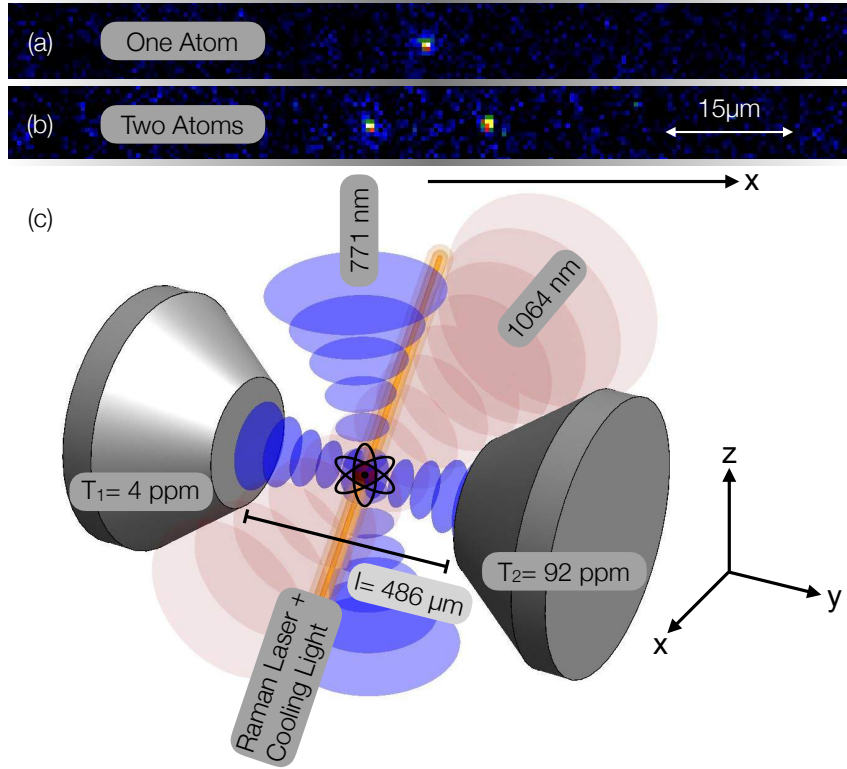
Figure 2.2.: Cavity trap geometry. The upper insets (a) and (b) show two EMCCD (electron multiplying charge-coupled device) camera pictures of atoms trapped between the cavity mirrors. The fluorescence light is imaged onto the EMCCD with an objective located above the cavity center (positive z axis in (c), objective not shown here). Examples of a single atom and an atom pair are shown in (a) and (b), respectively. A single atom is actively positioned to the center of the cavity mode via a galvanometric scanner shifting the position of the red-detuned trap. For an atom pair, the center of mass is positioned to the center of the cavity mode. The distance between two atoms is not actively controlled and varies probabilistically from pair to pair. However, the EMCCD camera pictures allow to apply a preselection of the atom pairs for suitable interatomic distances. The experimentally applied upper bound for the interatomic distance is $12\,\mu\mathrm{m}$. The lower part of the figure (c) shows the two Fabry-Pérot cavity mirrors (conically shaped gray objects). The cavity is single-sided with mirror transmissions of $T_1 = 4\,\mathrm{ppm}$ and $T_2 = 92\,\mathrm{ppm}$. Three standing wave beams cross at the cavity center. A red-detuned $1064\,\mathrm{nm}$ beam is oriented along the x direction. Furthermore two blue-detuned traps at $771\,\mathrm{nm}$ are oriented along the y and z direction. A Raman laser pair impinging from the side of the cavity (orange beam) allows to manipulate the atomic qubit coherently. Cooling light is impinging onto the atoms in the same spatial mode. A more detailed sketch of the experimental setup is shown in the appendix B.

into resonance with the $|F{=}2, m_F{=}2\rangle \rightarrow |F'{=}3, m_F{=}3\rangle$ transition. Note that this is the transition $|\uparrow\rangle \rightarrow |e\rangle$ introduced in section 2.2.

To load atoms into the cavity mode, a magneto-optical trap (MOT) is employed. The prepared cloud of cold atoms is transferred between the cavity mirrors with a far-off-resonance trap (FORT) [97] at a wavelength of $1064\,\mathrm{nm}$, focussed halfway between the position of the MOT and the center of the cavity. Once the atoms arrive in the cavity, three optical lattices

are switched on, two at 771 nm along the cavity axis and in the vertical direction and one at 1064 nm in the horizontal plane, vertical to the cavity axis. The spatial orientation of these standing waves is shown graphically in figure 2.2. The atoms are held in this 3D configuration for a time on the order of a few seconds before they are lost from the trap and a new MOT is created to reload the next atom. To cool the atoms in the trap, two cooling beams are impinging onto the atoms from the side. They are counterpropagating and impinge onto the atoms in the same spatial mode as the Raman laser beams (orange beam in figure 2.2). Due to their perpendicular linear polarization, the two counterpropagating beams form spatially varying polarization pattern suitable for Sisyphus cooling [88]. The two beams also contain repumping light on the atomic $|F = 1\rangle \rightarrow |F' = 2\rangle$ transition. To avoid parametric heating and thus atom loss, the power of the intracavity trap is stabilized actively. In this particular trap configuration it was demonstrated that Raman sideband cooling can be employed to transfer single atoms into the three-dimensional ground state of the trapping potential [98]. A 5 ms interval of Raman sideband cooling is sufficient to populate this ground state with a probability of $(89 \pm 2)\%$. In the experiments described in this thesis, ground state cooling was not employed as the described entanglement and gate mechanisms for the two atoms are insensitive to atomic motion. The storage time of the atoms is limited by the background pressure in the vacuum system to approximately a minute. The storage time also strongly depends on the experimental protocol and the laser beams applied to the atom. Especially the application of a state detection beam on resonance with the $|\uparrow\rangle \rightarrow |e\rangle$ transition leads to heating and thus to a decrease of the storage time. For the quantum gate and the quantum state carving protocol, the two-atom storage time is typically 5 s. To position the atoms in the cavity mode, a galvanometric scanner allows to rotate a glass plate in the beam path of the 1064 nm standing wave trap. Employing this technique, the phase of the red-detuned standing wave trap can be moved back and forth and thus the center of mass of the atom pair can be actively positioned with submicron precision to the center of the cavity mode [99]. The atoms are observed with an imaging system consisting of a high NA objective (NA=0.40) and an EMCCD camera. Typical camera pictures of a single atom and an atom pair are shown in the upper inset in figure 2.2.

For the case of an atom pair, the interatomic distance is not actively controlled. Due to the beating pattern between the 771 nm dipole trap on the cavity axis and the 780 nm cavity mode, the maximal coupling between the atoms and the cavity is established at the cavity center. If the atoms are trapped away from this point, the rate g decreases and assumes a minimum at a distance 16.2 μm from the cavity center. Therefore, the data for two-atom experiments are preselected such that only atom pairs with an interatomic distance below 12 μm are considered such that each individual atom is no more than 6 μm away from the cavity center.

For the case of a single atom, the relevant cavity QED parameters are $(g,\kappa,\kappa_{\mathrm{r}},\gamma) = 2\pi(7.8, 2.5, 2.3, 3.0)$ MHz. Here, g is the atom-cavity coupling rate. As outlined in section 2.1, this rate scales with the square root of the number of coupling atoms N. For the case of $N = 2$ atoms, g increases to $g = \sqrt{2} \times 7.8$ MHz ≈ 11 MHz. Furthermore, κ describes the total cavity field decay rate while κ_{r} describes the field decay rate through the outcoupling mirror. The high ratio $\eta_{\mathrm{esc}} = \kappa_r/\kappa = 0.92$ is the escape propability of light through the outcoupling mirror. The total cavity field decay rate κ is the sum of three contributions, namely the decay rate through the outcoupling mirror κ_r, the decay rate through the other

cavity mirror κ_t and the parasitic loss rate due to scattering of light on the mirror surface and absorption in the mirror coating κ_m. Hence, $\kappa = \kappa_r + \kappa_t + \kappa_m$. The losses T_r, T_t and L_m associated with these three decay channels are related to κ via

$$\kappa = \kappa_r + \kappa_t + \kappa_m = \frac{c}{4l}(T_r + T_t + L_m), \tag{2.8}$$

where c is the speed of light. An important quantity describing the spectral properties of a Fabry-Pérot cavity is the cavity finesse $\mathcal{F}$. The finesse is defined as the ratio between the free spectral range ν_{FSR} and the cavity linewidth Δ_ν. For high-finesse cavities, the approximation

$$\mathcal{F} = \frac{\nu_{\mathrm{FSR}}}{\Delta_\nu} \approx \frac{2\pi}{T_r + T_t + L_m} \tag{2.9}$$

holds. Inserting the respective parameters yields a finesse of $\mathcal{F} \approx 6 \times 10^5$.

The atomic dipole decay rate is denoted by γ. In terms of the dipole matrix element μ_{ge} and the transition frequency ω_c, it can be expressed as

$$\frac{\gamma}{2\pi} = \frac{\mu_{ge}^2 \omega_c^3}{6\pi\hbar\epsilon_0 c^3}. \tag{2.10}$$

Inserting the corresponding parameters [92] for the transition from $5^2\mathrm{P}_{3/2}$ to $5^2\mathrm{S}_{1/2}$, one finds $\gamma/(2\pi) = 3\,\mathrm{MHz}$.

For the following chapters, it is convenient to define the single atom cooperativity C, a parameter quantifying the ratio of the relevant rates in the system. The single atom cooperativity is defined by

$$C := \frac{g^2}{2\kappa\gamma} = 4.1. \tag{2.11}$$

In the case of N atoms coupling to the cavity mode, the cooperativity grows linearly as $N \times C$. Since the rate g dominates all other decay rates in the system, the coupled system operates in the strong coupling regime. The total cavity decay rate κ is dominated by the decay rate through the outcoupling mirror κ_r. The ratio of these two quantities is $\eta_{\mathrm{esc}} := \kappa_r/\kappa = 0.92$. This ratio is the probability that an intracavity photon leaves the cavity through the outcoupling mirror and plays a crucial role in the experiments described in this thesis. At the output port of the cavity, single-photon detectors (SPDs) are employed to collect light coupled out of the cavity. These detectors (brand: Perkin-Elmer/Excelitas) have a quantum efficiency of 55%. The photon click pulses from these detectors are later digitized and evaluated with a computer. Waveplates in front of the respective detectors facilitate a polarization-resolved measurement of the light in the reflection mode of the cavity.

2.4. Experimental Toolbox

For applications in quantum information processing, the precise control of the atomic qubits trapped in the cavity mode is necessary. Therefore, an experimental toolbox that allows the experimenter to actively control the atoms is needed. The toolbox consists of three necessary ingredients.

- **Initialization**: First, the atoms must be initialized in a well defined state via optical pumping. This state will serve as a starting point for the desired protocol to follow. The process to initialize atoms in a desired state will be described in section 2.4.1.

- **State manipulation**: After the initialization, the experimenter needs coherent control over the atomic state. To this end, a pair of Raman lasers is employed. The setup and operation principle of these Raman lasers will be outlined in section 2.4.2.

- **State detection**: Eventually, a method for readout of the atomic state is required. In this thesis, a method for the simultaneous readout of two atoms was developed. This method is explained in section 2.4.3.

2.4.1. Optical Pumping of Two Atoms

For any quantum information processing application, a mechanism that initializes the employed qubits in a well defined state is a necessary prerequisite. For the specific case of two atomic qubits, natural choices for such initial states are $|\uparrow\uparrow\rangle$ or $|\downarrow\downarrow\rangle$. The state $|\uparrow\uparrow\rangle$ can be prepared by optical pumping of the two atoms via application of the right-circular pump laser on the transition $|\uparrow\rangle \rightarrow |e\rangle$ along the cavity axis and the repump laser on the $|F = 1\rangle$ to $|F' = 2\rangle$ transition (see appendix A) impinging perpendicularly onto the cavity axis. In the case of a single atom, this pumping technique allows to prepare the state $|\uparrow\rangle$. The pumping of two atoms into the state $|\uparrow\uparrow\rangle$ has a subtlety to it. Once one atom is pumped to the state $|\uparrow\rangle$, it strongly couples to the cavity and prevents additonal pump light from entering the cavity and pumping the second atom. This phenomenon is also relevant for the measurement of a normal mode spectrum for two atoms in section 3.4.1. A way around this problem is to detune the two atoms from the cavity resonance by a few MHz during the pumping process via the application of an ac-Stark shift induced by the 1064 nm trap laser. In this scenario, the cavity will not become completely blocked for the pump light even if a coupling atom is present. After the pump process, the atoms are tuned back into cavity resonance by another change of the ac-Stark shift. After the successful preparation of the state $|\uparrow\uparrow\rangle$, the state $|\downarrow\downarrow\rangle$ can be obtained through the execution of a π pulse via a pair of Raman lasers (see section 2.4.2). This state can be heralded via the application of a short laser pulse on the $|\uparrow\rangle \rightarrow |e\rangle$ transition impinging perpendicularly onto the cavity axis and a measurement of the atomic fluorescence collected in the cavity mode. If no fluorescence is observed, the state $|\downarrow\downarrow\rangle$ was generated successfully. Preparation fidelities for $|\downarrow\downarrow\rangle$ of 99% were achieved with this method.

It turned out that for the quantum state carving protocol in chapter 3, in some cases an initial antiparallel configuration of the two atoms is required. Ideally, one of the states $|\uparrow\downarrow\rangle$ or $|\downarrow\uparrow\rangle$ should therefore be generated. With laser beams addressing the two atoms simultaneously, it is not possible to generate either of these antiparallel states. However, it is possible to prepare an incoherent mixture of the form $\frac{1}{2}(|\uparrow\downarrow\rangle \langle\uparrow\downarrow| + |\downarrow\uparrow\rangle \langle\downarrow\uparrow|)$. This can be accomplished by applying the pump laser while the atoms are resonant with the cavity mode. Only one atom can be pumped initially. Afterwards, a π pulse is applied to transfer this atom to the state $|\downarrow\rangle$. The remaining atom can be transferred into the state $|\uparrow\rangle$ in a
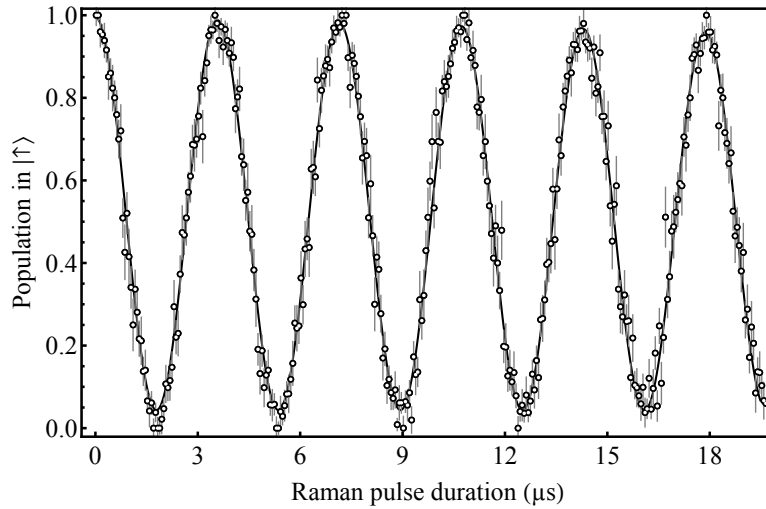
Figure 2.3.: Atomic state manipulation with the Raman laser pair. Example of Rabi oscillations driven in the atomic qubit consisting of the states $|\uparrow\rangle$ and $|\downarrow\rangle$. On two-photon resonance, a Rabi frequency of 280 kHz was achieved as can be extracted via a sinusodial fit with a Gaussian envelope (solid line). The decay of the oscillation amplitude over time is mainly due to magnetic field fluctuations acting on the magnetically sensitive qubit. This measurement was performed on two-photon resonance to observe a maximal visibility of the oscillatory signal.

second pump interval. Eventually, one atom will occupy $|\uparrow\rangle$ and one $|\downarrow\rangle$ in an incoherent mixture of the two possibilities.

2.4.2. Raman Laser Setup

To manipulate the internal electronic degree of freedom of the atoms and thereby control the atomic qubit, a pair of Raman lasers is employed. The Raman laser setup is described in detail in [93] and [100]. Here, a summary of the working principle and the experimental techniques for the manipulation of the qubit states is given.

In a two-photon process, the two Raman lasers can coherently transfer population between the two states qubit $|\uparrow\rangle$ and $|\downarrow\rangle$. The frequency difference of the two beams can be tuned to the hyperfine splitting of 6.835 GHz which is the transition frequency of the qubit. Both Raman beams originate from the same laser oscillator and sidebands at 6.515 GHz are modulated via a fiber based electro-optical modulator supplied with a microwave signal. The fine tuning to the hyperfine splitting is accomplished with an additional acousto-optical modulator. The two laser beams co-propagate in the same spatial mode (orange beam in figure 2.2) and have linear, but mutually orthogonal polarizations. They impinge onto the atoms from a direction perpendicular to the cavity axis. The Raman beams are $\Delta = 131$ GHz red-detuned from the D1 line of ^{87}Rb. It is convenient to define the cavity axis as the quantization axis of the atom-cavity system (the y axis in figure 2.2). A small magnetic field of 0.18 Gauss is applied along this direction. One of the Raman beams is linearly polarized parallel to this quantization axis and can therefore drive π transitions in the atoms such that the magnetic quantum number m_F is not changed. The other
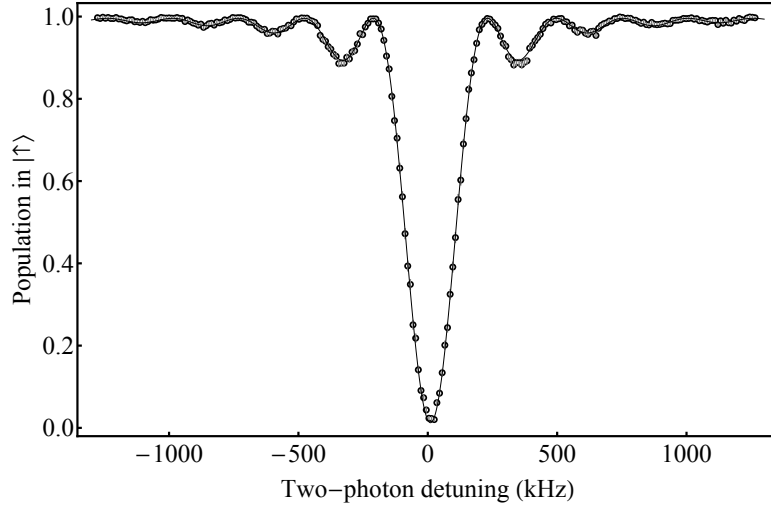
Figure 2.4.: Application of a π pulse. The atom is initialized in the state $|\uparrow\rangle$ before a π pulse is applied. If two-photon resonance is established, the entire population is transferred into the state $|\downarrow\rangle$. A scan of the two-photon detuning reveals the typical side peaks corresponding to the Fourier spectrum of the rectangular-shaped pulse applied to the atom.

Raman beam is polarized perpendicular to the cavity axis and can thus drive coherent superpositions of σ^+ and σ^- transitions where the magnetic quantum number is raised or lowered by one, respectively. The purpose of the Raman lasers is full coherent control over the atomic qubit based on the states $|\uparrow\rangle$ and $|\downarrow\rangle$ defined in section 2.2. With the pair of Raman lasers, it is possible to drive Rabi oscillations between these states. For the particular choice of Δ and the laser powers emitted from a diode laser, typical Rabi frequencies are on the order of hundreds of kilohertz.

Figure 2.3 shows an example of Rabi oscillations of a single atom driven with the Raman laser pair. For this measurement, the atom was initialized in the state $|\uparrow\rangle$ via optical pumping before a Raman pulse of variable length was applied. As outlined above, the optical pumping is realized with a right-circularly polarized pumping laser resonant with the cavity mode. The pumping process typically lasts for 200 µs until the state $|\uparrow\rangle$ is prepared with 99% fidelity. For the measurement of Rabi oscillations, a Raman pulse of variable length is applied to the atom after the pumping stage. Figure 2.3 shows the population in the state $|\uparrow\rangle$ as a function of this Raman pulse duration. To implement single atom qubit gates, a Raman pulse of defined pulse area can be applied to the atom by choosing an appropriate pulse length, laser power and phase.

It is important to note that the applied rectangular pulses have spectral sidebands which depend on the duration of the applied pulse. In order not to drive undesired Raman transitions in the atoms, it is essential to move the other involved Zeeman levels out of resonance with these sidebands. An example of such an undesired transition is the one from $|F = 1, m_F = 1\rangle$ to $|F = 2, m_F = 0\rangle$. To prevent the driving of these transitions, a magnetic field is applied along the cavity axis to get rid of the degeneracy of the m_F

sublevels. As an example, figure 2.4 shows the population in the state $|\uparrow\rangle$ after the application of a π pulse in $4\,\mu s$ as the two-photon detuning is scanned. Only in the case where two-photon resonance is established, the entire population can be transferred from the state $|\uparrow\rangle$ into the state $|\downarrow\rangle$. A linear scan of the two-photon detuning reveals the typical side peaks in the spectrum which can be associated with the Fourier transform of the employed square-shaped pulse. This spectrum has the form of a squared sinc function. If the undesired transitions are energetically tuned in such a way that no population transfer can take place, only the desired transition between $|\uparrow\rangle$ and $|\downarrow\rangle$ is driven. For this, the transition frequencies of the undesired transitions have to be tuned such that they coincide with the frequencies where the Fourier transform of the applied square pulse vanishes. The tuning of the respective transition frequencies for a given pulse length is achieved by changing the applied magnetic field appropriately.

2.4.3. State Detection of Two Atoms

After the application of a sequence of Raman pulses to execute a desired protocol with the atomic qubits residing in the cavity, the qubits can be read out with state detection light.

There are two ways to perform such a state detection measurement. The first method relies on probing the cavity transmission. Due to the coupling of atoms to the cavity mode, the transmission of the system strongly depends on the number of atoms in the coupling state. The second method relies on the detection of fluorescence photons collected in the cavity mode. Atoms in the $|\downarrow\rangle$ state will not scatter light into the cavity mode while atoms in the $|\uparrow\rangle$ state do.
The two methods were both used in previous experiments [101] where they were employed on a single atom in the cavity. In this work, a combined state detection method for two atoms was developed that allows to distinguish between the states $|\uparrow\uparrow\rangle$, $|\downarrow\downarrow\rangle$ and the space spanned by $\{|\uparrow\downarrow\rangle, |\downarrow\uparrow\rangle\}$. In the following, the two methods and their combination are described in detail.

2.4.3.1. State Detection in Transmission

The first state detection method relies on probing the transmission of a laser beam through the cavity [102]. The right-circularly polarized probe beam is injected onto the cavity mirror with the higher reflectivity and its transmission is measured with single-photon detectors monitoring the output mode of the cavity (see upper graphics in figure 2.5). The probe beam is resonant with the empty cavity and impinges onto the high reflection mirror of the latter. If both atoms occupy the state $|\downarrow\rangle$, they cannot couple to the cavity mode and a high transmission signal is observed. For our cavity, a maximal transmission of 10.3% is expected on resonance due to the asymmetric design described in section 2.3. Within a typical state detection interval of $3\,\mu s$, the photon number distributions shown in figure 2.5 are recorded. In the case of one or two atoms occupying the state $|\uparrow\rangle$, the transmission through the cavity is strongly reduced since the coupled atom-cavity system is not resonant with the probing laser anymore. The cavity transmission is not completely blocked via the atoms as the cooperativity $C = Ng^2/(2\kappa\gamma)$ is finite. Here, N is the number of atoms
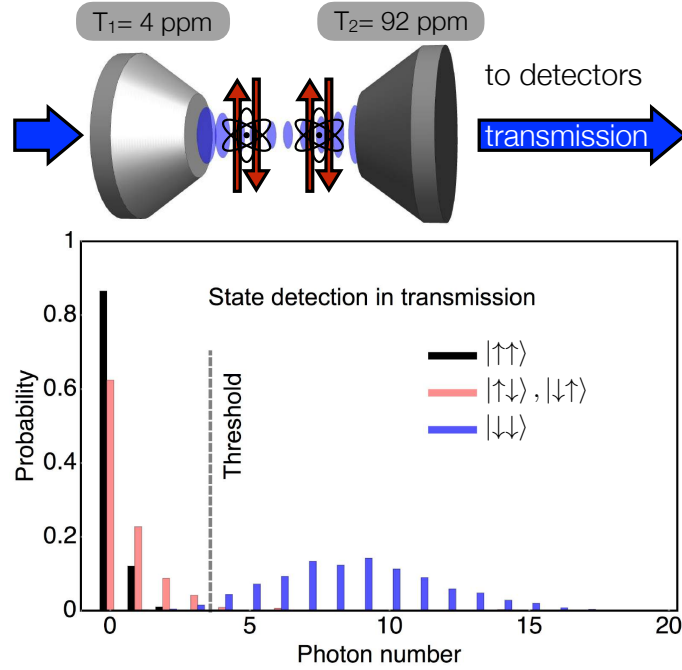
Figure 2.5.: State detection in transmission. Upper graphics: Resonant laser light (blue beam) is impinging on the $T_1 = 4$ ppm mirror of the cavity. The transmission is measured with single-photon detectors and strongly depends on the two-atom state in the cavity. Lower graphics: A laser resonant with the empty cavity is applied to the latter for a duration of $3\,\mu s$. The plot shows the probability to observe a certain photon number on a single-photon detector in this time interval. The suppression of the cavity transmission increases with the number of atoms occupying the coupling state $|\uparrow\rangle$.

occupying $|\uparrow\rangle$. In fact, the intracavity intensity and thus the transmission of the probing laser is suppressed by a factor of $(1 + 2C)^2$ where C is the cooperativity of the system [44]. For our cavity parameters, this leads to a suppression by a factor of 83 for $N = 1$ coupling atom and a respective factor of 297 for $N = 2$ coupling atoms. With increasing N, the Poissonian distributions are therefore shifted to lower photon numbers as can be observed in figure 2.5. In the experiment, the suppression of the transmitted light through the cavity is not quite as strong as expected from the calculated suppression factors. One reason for this is non-perfect coupling of the atoms to the cavity due to their finite temperature.

A threshold of $n = 3$ photons can be employed to distinguish between the distribution associated with $|\downarrow\downarrow\rangle$ and the distributions associated with $|\uparrow\uparrow\rangle$ and ($|\uparrow\downarrow\rangle$,$|\downarrow\uparrow\rangle$). Since there is a substantial overlap between the distributions corresponding to $|\uparrow\uparrow\rangle$ and ($|\uparrow\downarrow\rangle$,$|\downarrow\uparrow\rangle$), a single state detection interval is not sufficient to distinguish these distributions. To circumvent the problem, an additional state detection has to be applied to the atoms.

2.4.3.2. Fluorescence State Detection

The second method to read out the state of an atom or an atom pair is the measurement of photons scattered from the atoms into the cavity mode [103]. In principle, this state
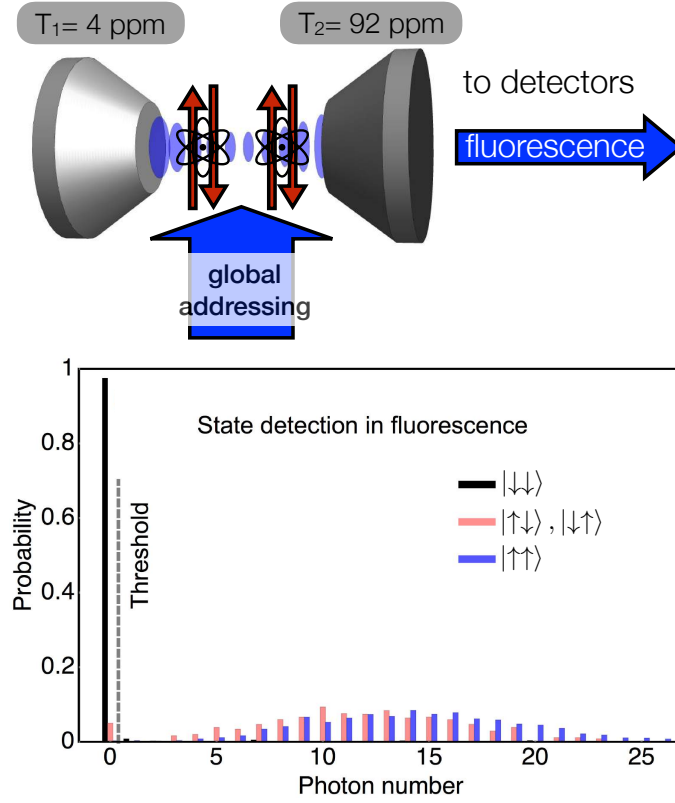
Figure 2.6.: Fluorescence state detection. Upper graphics: A global addressing beam (blue thick arrow) is impinging on the atom pair perpendicularly from the cavity axis. The fluorescence light is collected in the cavity mode and measured with single-photon detectors. Lower graphics: Photon number distributions for the cases where the two atoms are prepared in the states $|\uparrow\uparrow\rangle$, $(|\uparrow\downarrow\rangle, |\downarrow\uparrow\rangle)$ and $|\downarrow\downarrow\rangle$. The state detection laser is applied for 5 µs and impinges from the side onto the atom pair. The method allows to distinguish between the states $|\downarrow\downarrow\rangle$ and all other states where at least one of the atoms occupies the state $|\uparrow\rangle$. Note that the distributions for $|\uparrow\uparrow\rangle$ and $(|\uparrow\downarrow\rangle, |\downarrow\uparrow\rangle)$ strongly overlap and cannot be distinguished from each other. Their mean photon number is similar due to the interference effect studied in [86].

detection method can also be applied to atoms in free space. However, the fact that the Purcell effect [104] preferentially directs scattered photons into the cavity mode allows for an effective collection of those photons. The probability to scatter a photon into the cavity mode is given by $2C/(2C + 1) = 89\%$. The cavity therefore supports a fast state detection process. Typical durations of a state detection pulse are a few microseconds.

In our implementation, laser light resonant with the $|\uparrow\rangle \to |e\rangle$ transition is applied to the atoms. The laser beam has a waist of 30 µm and illuminates both atoms equally. It impinges onto the atoms from the side, perpendicular to the cavity axis (see upper graphics in figure 2.6). If the two atoms occupy the state $|\downarrow\downarrow\rangle$, ideally no fluorescence photons are detected. However, the presence of one atom in the state $|\uparrow\rangle$ leads to a Poissonian distribution of 11 detected photons on average in a typical state detection interval of 5 µs. If both of the atoms occupy the state $|\uparrow\rangle$, they will also scatter photons into the cavity mode. The photons emitted by the first atom can interfere with the ones from the second
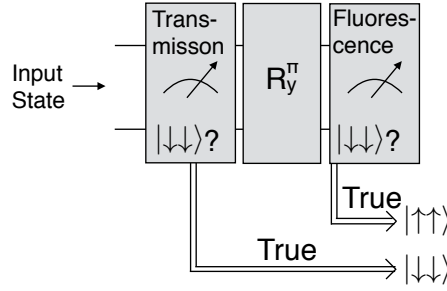
Figure 2.7.: Double state detection protocol. Two state detection pulses with an interleaved π rotation are applied to the atoms. The protocol allows to distinguish between the states $|\downarrow\downarrow\rangle$, $|\uparrow\uparrow\rangle$ and the states $(|\uparrow\downarrow\rangle, |\downarrow\uparrow\rangle)$.

atom. Depending on the relative positions of the two atoms, constructive or destructive interference can be observed. This phenomenon was extensively studied in [86]. Fig.2.6 shows the typical photon number statistics observed after each of the three states have been prepared. The figure shows a substantial overlap of the distributions associated with $(|\uparrow\downarrow\rangle, |\downarrow\uparrow\rangle)$ and $|\uparrow\uparrow\rangle$. The distribution for $|\downarrow\downarrow\rangle$, however, can be well distinguished from the other two. This is a property shared by the two different state detection methods.

2.4.3.3. Combination of Both State Detection Methods

A successive application of both state detection methods (transmission and fluorescence as outlined in the sections 2.4.3.1 and 2.4.3.2) with an interleaved π pulse allows to distinguish between the states $|\uparrow\uparrow\rangle$, $|\downarrow\downarrow\rangle$ and $(|\uparrow\downarrow\rangle, |\downarrow\uparrow\rangle)$. This means that the populations $P_{\uparrow\uparrow}$ and $P_{\downarrow\downarrow}$ can be measured separately. For the antiparallel configuration, only the sum $P_{\uparrow\downarrow} + P_{\downarrow\uparrow}$ can be measured as the two corresponding states cannot be distinguished from each other without individual addressing of the two atoms. The schematic circuit diagram for the two consecutive state detection methods is shown in Fig. 2.7. The first state detection relies on a measurement of the transmission of the cavity. As described in section 2.4.3.1 this method allows to distinguish $|\downarrow\downarrow\rangle$ from all other possible states. To distinguish $|\uparrow\uparrow\rangle$ from the remaining set of states, the populations are inverted with a π pulse such that $|\uparrow\uparrow\rangle$ is mapped to $|\downarrow\downarrow\rangle$ and $|\uparrow\downarrow\rangle$ and $|\downarrow\uparrow\rangle$ change their roles. With the second state detection in fluorescence, the state $|\downarrow\downarrow\rangle$ can be distinguished from the remaining states. In fact, the double state detection protocol can be performed with any combination of the two possible kinds of state detection protocols (fluorescence and transmission).

To characterize the quality of this newly developed *double state detection* method, the probability to correctly detect a well defined prepared state was determined. For the state $|\uparrow\uparrow\rangle$, the probability to detect less than three photons in the first state detection interval and no photon in the second state detection interval is 97.0%. Similarly, for the state $|\downarrow\downarrow\rangle$, the probability to detect more than three photons in the first interval and at least one photon in the second is 97.4%. For the states $|\uparrow\downarrow\rangle$ and $|\downarrow\uparrow\rangle$, the probability to first detect less than three photons and at least one in the second interval is given by 93.1%. These numbers are also affected by the state preparation process that generates desired

states with a fidelity of 99%. Also, there is a contribution of 0.2% in the experimental data, where the two state detections give imcompatible results due to detector dark counts. The combined state detection method will later serve as a tool to characterize the generated entanglement between the two atoms.

2.5. Phase Shift Mechanism

For the generation of entanglement between the atoms, a mechanism is employed where a phase is imprinted onto selected combined atom-atom-light states. This phase imprinting occurs upon the reflection of coherent light states from the cavity. The imprinted phase depends on the state of the atoms in the cavity, their detuning from the cavity resonance, the detuning of the light pulse from the cavity resonance, and the polarization state of the light.

The mechanism was observed in a series of experiments with different implementations of resonators [69, 101, 105–108]. In 2004, Duan and Kimble suggested to employ this mechanism to perform a quantum gate between two photons where the atom inside the cavity is used as a mediator of interaction between the photons that are successively reflected from the cavity [109]. This proposal was implemented experimentally in our group 2016 [35]. Building on this work, Duan, Wang and Kimble later suggested to build a quantum gate between two atoms in one cavity [75]. The suggested coupling mechanism between the atoms relies on a state-dependent phase shift in the atom-atom-photon state when the photon is reflected from the cavity. The implementation of this proposal is the main result of this thesis and will be described in detail in section 4. Another theoretical proposal [110] from the same time makes use of the phase shift mechanism to deterministically generate entangled states between an atomic qubit and an optical cat state. The generation of these entangled atom-light Schrödinger-cat states was recently achieved in our group [111]. The variety of these examples demonstrates the strength of the employed mechanism and its versatility in quantum information processing applications.

The magnitude of the imprinted phase shift can be derived from cavity input-output theory [93, 112, 113]. The reflection amplitude of a coupled atom-cavity system can be expressed as

$$r(\omega) = 1 - \frac{2\kappa_{\mathrm{r}}(i\Delta_a + \gamma)}{(i\Delta_c + \kappa)(i\Delta_a + \gamma) + Ng^2} \ , \tag{2.12}$$

where $\Delta_{c(a)} = \omega - \omega_{c(a)}$ is the detuning of the driving laser operating at a frequency ω compared to the cavity resonance ω_c or the atomic resonance ω_a. In general, $r(\omega)$ is a complex number. The intensity of the reflected light is given by the square modulus of the reflection amplitude $R(\omega) = |r(\omega)|^2$. The phase of the reflected light is expressed as $\arg(r(\omega))$, the angle of r to the positive real axis. The cavity is tuned actively to a chosen atomic transition such that $\Delta_a = \Delta_c = 0$ can be established by tuning the laser frequency ω to that transition frequency as well. The transition of choice is the one from $|\uparrow\rangle$ to $|e\rangle$. The experimentally relevant relative phase shift is defined as the difference of the phase of

the reflected light for a coupled compared to an uncoupled cavity. Therefore, this phase shift can be expressed as

$$\Delta_{\text{phase}}(\omega) = \arg\left(r(g > 0, \omega)\right) - \arg\left(r(g = 0, \omega)\right). \tag{2.13}$$

It should be noted that on resonance where $\Delta_c = \Delta_a = 0$ holds, the relative phase shift Δ_{phase} assumes a value of π for our cavity QED parameters.

There is an intuitive explanation for this phenomenon. Light impinging onto the cavity outcoupling mirror enters an uncoupled (empty) cavity, bounces back and forth between the two mirrors and eventually leaves through the outcoupling mirror. However, if one or two coupling atoms are present, the light cannot enter the cavity and is directly reflected from the outcoupling mirror. The phase shift of π between these two situations can be explained as follows. When the light impinges onto an empty cavity, the directly reflected part interferes destructively with the incoming part such that the light can enter the resonator. In the case of a coupled cavity, there is constructive interference for the direct reflection. This means that a phase difference $\Delta_{\text{phase}} = \pi$ occurs between the two situations.

There are different methods to measure this phase difference. In general, the experimental methods can be divided into two categories. The first category contains measurements on the photonic output state after the reflection from the cavity. The second category contains measurements on the atomic qubit after reflection of the light.

A method that belongs to the first category relies on reflecting photons in a linear polarization state of the form $\frac{1}{\sqrt{2}}(|R\rangle + |L\rangle)$ from the cavity containing a single atom [93]. Here, $|R\rangle$ and $|L\rangle$ denote right- and left-circular polarization states, respectively. The photons are tuned into resonance with the uncoupled cavity. The situation is shown in detail in figure 2.8. The result after the reflection is a polarization rotation of the photons as a relative phase shift between the left- and the right-circular component is imprinted. To understand the effect, it is convenient to consider the case where photons in the state $|R\rangle$ or $|L\rangle$ are reflected from the cavity. If the atom occupies the state $|\downarrow\rangle$, both polarization components can enter the cavity and leave the latter through the outcoupling mirror after being bounced back and forth in the cavity mode. As both polarization components enter, a phase shift of π is imprinted onto the combined atom-photon state in both cases. Therefore, the phase shift acts as a global phase and no polarization change is observed when comparing the incoming and the outgoing light. In the case where the atom is prepared in the state $|\uparrow\rangle$, only $|L\rangle$ polarized light can enter the cavity. In the case of $|R\rangle$ polarized light, the atom coupled to the cavity prevents light from entering. Mathematically, the situation resembles a controlled phase gate between the atomic qubit and the photonic qubit. The respective truth table can be expressed as

$$\begin{aligned}
|\uparrow\rangle\,|R\rangle &\longrightarrow +\,|\uparrow\rangle\,|R\rangle \\
|\uparrow\rangle\,|L\rangle &\longrightarrow -\,|\uparrow\rangle\,|L\rangle \\
|\downarrow\rangle\,|R\rangle &\longrightarrow -\,|\downarrow\rangle\,|R\rangle \\
|\downarrow\rangle\,|L\rangle &\longrightarrow -\,|\downarrow\rangle\,|L\rangle
\end{aligned} \tag{2.14}$$

where the minus signs are due to the π phase shift that occur whenever the light can enter the cavity. This particular gate was demonstrated experimentally in 2014 in our group [69].
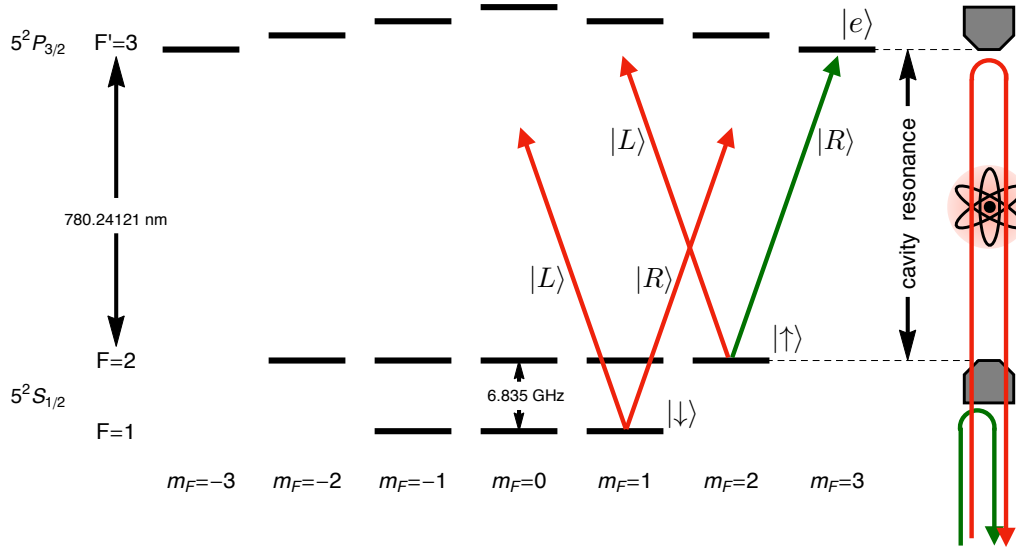
Figure 2.8.: Level scheme of the D_2 line of ^{87}Rb and phase shift mechanism. The cavity is actively stabilized to the optical transition $|\uparrow\rangle \to |e\rangle$. Due to the ac-Stark effect induced by the 1064 nm trapping laser, the Zeeman states with $-2 \leq m_F \leq 2$ in the excited state manifold $F' = 3$ are tuned out of cavity resonance. Light with different circular polarization states is reflected from the cavity. Right-circular polarized light ($|R\rangle$) drives transitions with $\Delta m_F = +1$ while left-circular polarized light ($|L\rangle$) drives transitions with $\Delta m_F = -1$. A photon with right-circular polarization resonant with the cavity will bounce off the first cavity mirror if the atom inside the cavity occupies the state $|\uparrow\rangle$ (green arrow). A left-circular polarized photon however can enter the cavity even if the atom occupies $|\uparrow\rangle$ (upper red arrow). If the atom occupies the state $|\downarrow\rangle$, both left- and right-circular polarized photons can enter the cavity (lower red arrows). A relative phase shift between the cases described by the red arrows and the case described by the green arrow allows for the implementation of a quantum gate between the atomic and the photonic qubit. The graphics is adapted from [93]. For a more detailed level scheme of the ^{87}Rb D_2 line, see appendix A.

To characterize Δ_{phase}, linearly polarized light states can be reflected from the atom-cavity system. A differential phase shift between the $|R\rangle$ and $|L\rangle$ component leads to a change of the resulting polarization state. A measurement of this state in different detection bases allows to extract the imprinted phase shift [93].

Another method from the first category to quantify the phase shift mechanism relies on the tomographic state reconstruction of the reflected light with a homodyne setup. The homodyne measurement allows to reconstruct the Wigner function of the outgoing photonic state. Coherent states of right-circular polarization are reflected from the cavity that contains an atom in a superposition state. The atomic superposition state consists of equal components of $|\uparrow\rangle$ and $|\downarrow\rangle$. Accordingly, the Wigner function of the outgoing state will contain two coherent components with different phase angles. The angle between these two distributions in phase space is the desired phase difference Δ_{phase}. The homodyne-based characterization of Δ_{phase} is described in detail in the PhD thesis of Bastian Hacker [94].

The methods for the phase characterization in the second category rely on a measurement of the atomic qubit. In a nondestructive measurement of optical photons [101], it was

demonstrated that a state detection of the atomic qubit can herald the presence of a photon in a coherent pulse. Here, the π phase shift was detected via the atom in the cavity. Another and related method belonging to the second category relies on the measurement of an atomic Raman spectrum that is affected by the reflected light. This method will be discussed in section 3.4.5.

As already mentioned, on resonance the relative phase Δ_{phase} shift assumes a value of

$$\begin{aligned}
\Delta_{\text{phase}}\Big(\Delta_c = \Delta_a = 0\Big) &= \arg\Big(r(g{=}2\pi \times 7.8\,\text{MHz}, \Delta_c{=}\Delta_a{=}0)\Big) \\
&\quad - \arg\Big(r(g{=}0.0\,\text{MHz}, \Delta_c{=}\Delta_a{=}0)\Big) \\
&= \pi.
\end{aligned} \tag{2.15}$$

The reason for this is a sign change of the reflection amplitude between the cases where $g = 0.0\,\text{MHz}$ and $g = 2\pi \times 7.8\,\text{MHz}$. If Δ_c or Δ_a deviate from zero, the phase difference will deviate from the desired value of π. Thus, it is important to precisely lock the employed laser onto the cavity resonance. Any fluctuation in the detunings Δ_a and Δ_c will influence the phase difference and thus decrease the fidelity of the quantum gates that rely on this mechanism. But not only the relative stability of the employed lasers with respect to the cavity has to be ensured. The bandwidth of the employed photon also plays a crucial role. If these photons are short in the time domain, they have a broad frequency spectrum. As a result, the phase difference between the coupling and the non-coupling component will smear out due to the sampling over different values of Δ_c. For the experiment, this means that the temporal width of the employed photons must not be too small.

This effect was studied in an earlier experimental work on the same setup [46]. In this work, it was found that the full width at half maximum (FWHM) of the employed Gaussian shaped light pulses has to exceed $\approx 0.6\,\mu\text{s}$ such that the phase shift mechanism works reliably. In the quantum gate experiment described in chapter 4, it is ensured that the light pulses reflected from the cavity have a FWHM of $0.9\,\mu\text{s}$ such that the phase shift mechanism works properly.

3. Quantum State Carving

Entanglement is a central phenomenon of modern quantum theory and describes the situation where the combined state of an ensemble of quantum particles cannot be separated into the individual parts. Instead, only a combined state of the entire entangled system can be written down. Entanglement between two or more quantum objects has been generated in a number of different experimental platforms like photons [33, 35, 114–116], ions [77, 117–120], atoms in Rydberg states [39, 121–123], atoms in optical tweezers [124], artificial atoms [125–129], hybrid systems [69, 130–132] and ensembles [133]. In this chapter, the implementation of a novel scheme to generate entanglement between two ^{87}Rb atoms in the same cavity [42] is introduced. The scheme is based on the reflection of weak coherent optical pulses from the atom-atom-cavity system. To generate the entanglement, projective measurements on the atom-atom state are performed as proposed theoretically in 2003 [80]. Coherent pulses with an initial antidiagonal linear polarization state ($|A\rangle$) change their polarization to diagonal ($|D\rangle$) if at least one atom occupies the state $|\uparrow\rangle$. In the case where both atoms are in the non-coupling state $|\downarrow\rangle$, the polarization state of the optical pulse is not changed after the reflection. A postselection of the measured data on the case of a polarization flip allows to remove the $|\downarrow\downarrow\rangle$ component from the two-atom state, a technique referred to as *carving* [134]. The method is intrinsically probabilistic but heralded via the polarization-resolved measurement of the light after the reflection process. For the experimental implementation of the carving technique, a global addressing beam for both atomic qubits is sufficient to generate all four maximally entangled Bell states [135]. The protocol can be extended to entangle more than two atoms in the same cavity.

3.1. The Protocol Described Theoretically

The reflection of antidiagonally polarized optical pulses from the cavity can be characterized in the form of a truth table. For an evaluation of this truth table, equation 2.14 is employed

and extended to the case of two atoms in the cavity. The extended version in the photonic R/L basis reads

$$\begin{aligned}
\left|\uparrow\uparrow\right\rangle\left|R\right\rangle &\to \left|\uparrow\uparrow\right\rangle\left|R\right\rangle & \left|\uparrow\uparrow\right\rangle\left|L\right\rangle &\to -\left|\uparrow\uparrow\right\rangle\left|L\right\rangle \\
\left|\uparrow\downarrow\right\rangle\left|R\right\rangle &\to \left|\uparrow\downarrow\right\rangle\left|R\right\rangle & \left|\uparrow\downarrow\right\rangle\left|L\right\rangle &\to -\left|\uparrow\downarrow\right\rangle\left|L\right\rangle \\
\left|\downarrow\uparrow\right\rangle\left|R\right\rangle &\to \left|\downarrow\uparrow\right\rangle\left|R\right\rangle & \left|\downarrow\uparrow\right\rangle\left|L\right\rangle &\to -\left|\downarrow\uparrow\right\rangle\left|L\right\rangle \\
\left|\downarrow\downarrow\right\rangle\left|R\right\rangle &\to -\left|\downarrow\downarrow\right\rangle\left|R\right\rangle & \left|\downarrow\downarrow\right\rangle\left|L\right\rangle &\to -\left|\downarrow\downarrow\right\rangle\left|L\right\rangle .
\end{aligned} \tag{3.1}$$

Based on equation 3.1, the truth table for the case of linearly polarized input light ($\left|A\right\rangle$) can be evaluated and yields

$$\begin{aligned}
\left|\uparrow\uparrow\right\rangle\left|A\right\rangle &\to \left|\uparrow\uparrow\right\rangle\left|D\right\rangle \\
\left|\uparrow\downarrow\right\rangle\left|A\right\rangle &\to \left|\uparrow\downarrow\right\rangle\left|D\right\rangle \\
\left|\downarrow\uparrow\right\rangle\left|A\right\rangle &\to \left|\downarrow\uparrow\right\rangle\left|D\right\rangle \\
\left|\downarrow\downarrow\right\rangle\left|A\right\rangle &\to \left|\downarrow\downarrow\right\rangle\left|A\right\rangle .
\end{aligned} \tag{3.2}$$

Here, the convention $\left|A\right\rangle = \frac{1}{\sqrt{2}}(\left|L\right\rangle - i\left|R\right\rangle)$ and $\left|D\right\rangle = \frac{1}{\sqrt{2}}(\left|L\right\rangle + i\left|R\right\rangle)$ was chosen and global phases are neglected. Whenever at least one of the two atoms occupies the coupling state $\left|\uparrow\right\rangle$, the relative phase between the $\left|R\right\rangle$ and $\left|L\right\rangle$ component of the linearly polarized input light is changed by π radians and a polarization rotation results. Only in the case where none of the atoms couple to the cavity mode, the polarization of the input light is maintained. To generate entanglement with the carving technique, both atoms are initially pumped into the coupling state $\left|\uparrow\uparrow\right\rangle$. Subsequently, a Raman pulse is applied to perform a global $\pi/2$ rotation such that both of the atoms end up in an equal superposition state of $\left|\uparrow\right\rangle$ and $\left|\downarrow\right\rangle$. At this stage of the protocol, the combined atom-atom state is given by

$$\frac{1}{\sqrt{2}}(\left|\uparrow\right\rangle - \left|\downarrow\right\rangle) \otimes \frac{1}{\sqrt{2}}(\left|\uparrow\right\rangle - \left|\downarrow\right\rangle) = \frac{1}{2}(\left|\uparrow\uparrow\right\rangle - \left|\uparrow\downarrow\right\rangle - \left|\downarrow\uparrow\right\rangle + \left|\downarrow\downarrow\right\rangle). \tag{3.3}$$

This state is still separable. The first reflection of an antidiagonally polarized photon results in the state

$$\frac{1}{2}(\left|\uparrow\uparrow\right\rangle\left|D\right\rangle - \left|\uparrow\downarrow\right\rangle\left|D\right\rangle - \left|\downarrow\uparrow\right\rangle\left|D\right\rangle + \left|\downarrow\downarrow\right\rangle\left|A\right\rangle). \tag{3.4}$$

A subsequent postselection on a $\left|D\right\rangle$ polarized optical output state probabilistically carves this state to generate

$$\frac{1}{\sqrt{3}}(\left|\uparrow\uparrow\right\rangle - \left|\uparrow\downarrow\right\rangle - \left|\downarrow\uparrow\right\rangle). \tag{3.5}$$

For this initial step, the probability of a successful carving operation is 3/4. To characterize the amount of entanglement in the generated states, an entanglement witness can be employed. Here, the *concurrence* is used [136]. The concurrence assumes values between zero and one depending on the amount of entanglement in the atom-atom state. Maximally entangled states have a concurrence of one while separable states have a concurrence of zero. The concurrence of state 3.5 is 2/3 and therefore it already contains entanglement. For the generation of a maximally entangled Bell state however, the $\left|\uparrow\uparrow\right\rangle$ component needs to be removed as well. To accomplish this, a π pulse is applied to both atoms which inverts
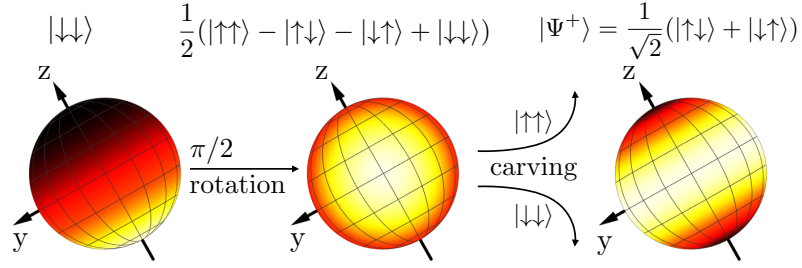
Figure 3.1.: Quantum state carving. The figure shows the Husimi Q distribution of the two-atom states generated at different steps of the carving protocol. An initial symmetric distribution around the south pole of the generalized Bloch sphere can be rotated onto the equator via a global $\pi/2$ rotation acting on both qubits. After the carving operation, a ring-shaped distribution along the equator of the Bloch sphere emerges. The color code is normalized in all shown Husimi distributions and increases from black (zero) to white.

the roles of $|\uparrow\rangle$ and $|\downarrow\rangle$. After application of this pulse, the state $\frac{1}{\sqrt{3}}(|\downarrow\downarrow\rangle + |\uparrow\downarrow\rangle + |\downarrow\uparrow\rangle)$ is generated. After the reflection of another $|A\rangle$ polarized pulse, the state

$$\frac{1}{\sqrt{3}}(|\downarrow\downarrow\rangle |A\rangle + |\uparrow\downarrow\rangle |D\rangle + |\downarrow\uparrow\rangle |D\rangle) \tag{3.6}$$

results. Postselection on the $|D\rangle$ polarization state completes the second carving step and removes $|\downarrow\downarrow\rangle$. This results in a maximally entangled Bell state [135]

$$\left|\Psi^+\right\rangle := \frac{1}{\sqrt{2}}(|\uparrow\downarrow\rangle + |\downarrow\uparrow\rangle). \tag{3.7}$$

The state $|\Psi^+\rangle$ has a concurrence of unity. The success probability for the second carving step is $2/3$. In combination with the success probability of the first carving step, the probability to obtain a maximally entangled state after the entire protocol is $P_{\text{success}} = 3/4 \times 2/3 = 1/2$. This success probability can only be achieved by employing an ideal single-photon source with an efficiency of unity. The actual experiment is performed with weak coherent pulses which leads to a reduction of P_{success}. Nevertheless, the use of coherent pulses to execute the carving procedure does not influence the fidelity of the produced entangled states unless photons from this pulse are scattered from the atom pair. This feature is certainly beneficial since coherent laser pulses can be generated easily in the laboratory.

3.2. The Husimi Q Distribution

The carving process is visualized in Fig. 3.1 where the Husimi Q distributions of the two-atom states 3.3 and 3.7 are illustrated. The Husimi Q distribution [137, 138] of an N particle state described by a density matrix ρ is a quasiprobability distribution [139] defined as [90, 140]

$$Q(\rho; \theta, \phi) = \frac{N+1}{4\pi} \langle \theta, \phi | \rho | \theta, \phi \rangle . \tag{3.8}$$

Here, $|\theta,\phi\rangle = \bigotimes_{j=1}^{N}[\cos(\theta/2)\,|\uparrow\rangle_j - e^{i\phi}\sin(\theta/2)\,|\downarrow\rangle_j]$ are *coherent spin states* [141, 142] and θ and ϕ are spherical coordinates on the generalized Bloch sphere of radius $J = N/2$. The coherent spin states are not mutually orthogonal and form an overcomplete basis spanning the symmetric part of Hilbert space. The Husimi Q distribution is non-negative and bounded from above by $Q \leq (N+1)/(4\pi)$. Furthermore, Q is normalized since $\int_{d\Omega} Q(\theta,\phi) = 1$ where $d\Omega = \sin\theta\,d\theta\,d\phi$. It is important to note that the Husimi Q distribution only contains information about the symmetric part of the density matrix ρ. All coherent spin states are symmetric states. Entirely non-symmetric states have a vanishing Husimi Q distrubution over the entire generalized Bloch sphere. An example of such a state is the singlet state $|\Psi^-\rangle := \frac{1}{\sqrt{2}}(|\uparrow\downarrow\rangle - |\downarrow\uparrow\rangle)$. The Husimi Q distribution for the states shown in Fig. 3.1 and other examplary states are listed in table 3.1.

Table 3.1.: Husimi Q distributions. List of Husimi Q distributions for different two-atom states according to eqn. 3.8. A plot of some distributions on a generalized Bloch sphere is shown in Fig. 3.1. Note that the Husimi Q distribution corresponding to the singlet state $|\Psi^-\rangle$ vanishes over the entire Bloch sphere as this state is non-symmetric.

State	Husimi distribution $Q(\rho;\theta,\phi)$
$|\downarrow\downarrow\rangle$	$3/(4\pi)\sin^4(\theta/2)$
$1/2(|\uparrow\uparrow\rangle - |\uparrow\downarrow\rangle - |\downarrow\uparrow\rangle + |\downarrow\downarrow\rangle)$	$3/(16\pi)(\cos(\phi)\sin(\theta)-1)^2$
$|\Psi^+\rangle = 1/\sqrt{2}(|\uparrow\downarrow\rangle + |\downarrow\uparrow\rangle)$	$3/(8\pi)\sin(\theta)^2$
$|\Psi^-\rangle = 1/\sqrt{2}(|\uparrow\downarrow\rangle - |\downarrow\uparrow\rangle)$	0
$|\Phi^+\rangle = 1/\sqrt{2}(|\uparrow\uparrow\rangle + |\downarrow\downarrow\rangle)$	$3/(32\pi)(3 + \cos(2\theta) + 2\cos(2\phi)\sin^2(\theta))$
$|\Phi^-\rangle = 1/\sqrt{2}(|\uparrow\uparrow\rangle - |\downarrow\downarrow\rangle)$	$3/(32\pi)(3 + \cos(2\theta) - 2\cos(2\phi)\sin^2(\theta))$

The Husimi Q distribution is a quantity that can be accessed experimentally as will be discussed in section 3.7. For a coherent spin state, $Q(\rho;\theta,\phi)$ is a round distribution and its center of mass can be moved to any point of the generalized Bloch sphere with global qubit rotations. Special cases are the states where $\theta = 0$ (north pole) or $\theta = \pi$ (south pole) where all qubits occupy the state $|\uparrow\rangle$ or $|\downarrow\rangle$, respectively.

For the entangled Bell states in the triplet manifold $|\Psi^+\rangle$, $|\Phi^-\rangle$, $|\Phi^+\rangle$, the Husimi Q distribution has the shape of a ring. The orientation of this ring depends on the respective Bell state and can also be controlled via global qubit rotations. Thus, once one of the triplet states has been generated experimentally, the other two can be generated via the application of a global Raman pulse. For the singlet state $|\Psi^-\rangle$, the situation is different. It has a vanishing overlap with the coherent spin states and thus a Husimi Q distribution of zero for all angle pairs (θ, ϕ). To generate this state, a modified carving scheme is necessary. This scheme will be discussed in section 3.4.8.

3.3. The Method of Parity Oscillations

To verify the creation of entanglement, the method of *parity oscillations* is employed [117, 118]. This technique allows to determine the fidelity of the experimentally generated state with a maximally entangled ideal state without measuring all entries of the density matrix. The method relies on the application of an analysis pulse of variable phase ϕ to the

two atoms after a desired entangled state is generated. This pulse transfers the off-diagonal coherence elements in the density matrix onto the diagonal which can be accessed via a subsequent state detection. For the state detection, the protocol outlined in section 2.4.3.3 is employed. The fidelity of the experimentally generated ρ with the ideal state $|\psi\rangle$ is given by $F = \langle\psi|\rho|\psi\rangle$. Inserting the four Bell states

$$\left|\Psi^+\right\rangle = \frac{1}{\sqrt{2}}(|\uparrow\downarrow\rangle + |\downarrow\uparrow\rangle) \tag{3.9}$$

$$\left|\Psi^-\right\rangle = \frac{1}{\sqrt{2}}(|\uparrow\downarrow\rangle - |\downarrow\uparrow\rangle) \tag{3.10}$$

$$\left|\Phi^+\right\rangle = \frac{1}{\sqrt{2}}(|\uparrow\uparrow\rangle + |\downarrow\downarrow\rangle) \tag{3.11}$$

$$\left|\Phi^-\right\rangle = \frac{1}{\sqrt{2}}(|\uparrow\uparrow\rangle - |\downarrow\downarrow\rangle) \tag{3.12}$$

into the definition of F, one finds that the fidelities with the four Bell states are given by

$$F(\left|\Psi^\pm\right\rangle) = \frac{1}{2}(P_{\uparrow\downarrow} + P_{\downarrow\uparrow}) \pm \mathrm{Re}(\rho_{\uparrow\downarrow,\downarrow\uparrow}) \tag{3.13}$$

$$F(\left|\Phi^\pm\right\rangle) = \frac{1}{2}(P_{\uparrow\uparrow} + P_{\downarrow\downarrow}) \pm \mathrm{Re}(\rho_{\uparrow\uparrow,\downarrow\downarrow}).$$

Here $P_{ij} = \rho_{ij,ij}$ are the probabilities to find the first atom in the state $|i\rangle$ and the second in the state $|j\rangle$ with $i,j \in \{\uparrow, \downarrow\}$. The terms $\rho_{\uparrow\downarrow,\downarrow\uparrow}$ and $\rho_{\uparrow\uparrow,\downarrow\downarrow}$ are the coherence terms in the density matrix of the form

$$\rho = \begin{pmatrix} \rho_{\uparrow\uparrow,\uparrow\uparrow} = P_{\uparrow\uparrow} & \rho_{\uparrow\uparrow,\uparrow\downarrow} & \rho_{\uparrow\uparrow,\downarrow\uparrow} & \rho_{\uparrow\uparrow,\downarrow\downarrow} \\ \rho_{\uparrow\downarrow,\uparrow\uparrow} & \rho_{\uparrow\downarrow,\uparrow\downarrow} = P_{\uparrow\downarrow} & \rho_{\uparrow\downarrow,\downarrow\uparrow} & \rho_{\uparrow\downarrow,\downarrow\downarrow} \\ \rho_{\downarrow\uparrow,\uparrow\uparrow} & \rho_{\downarrow\uparrow,\uparrow\downarrow} & \rho_{\downarrow\uparrow,\downarrow\uparrow} = P_{\downarrow\uparrow} & \rho_{\downarrow\uparrow,\downarrow\downarrow} \\ \rho_{\downarrow\downarrow,\uparrow\uparrow} & \rho_{\downarrow\downarrow,\uparrow\downarrow} & \rho_{\downarrow\downarrow,\downarrow\uparrow} & \rho_{\downarrow\downarrow,\downarrow\downarrow} = P_{\downarrow\downarrow} \end{pmatrix}. \tag{3.14}$$

It is clear from equations 3.13 that not all of the entries of the density matrix are needed to calculate the fidelity. Experimentally, two measurements are necessary, one to extract the populations (diagonal elements of the density matrix) and a second one to extract the relevant coherence terms.

To measure the coherence terms, the additional analysis pulse with an area of $\pi/2$ and phase ϕ is applied to the atoms. This pulse generates a modified density matrix $\tilde{\rho}$ with populations $\tilde{P}_{i,j}$ as diagonal elements. The populations $\tilde{P}_{i,j}$ depend on ϕ that is scanned from 0 to 2π. The analysis pulse can be mathematically expressed as a rotation matrix $R(\vec{v},\alpha)$ where $\vec{v}$ is the rotation axis vector and α is the rotation angle. Such a rotation matrix can be expressed in the form

$$R(\vec{v},\alpha) = \exp\left(-i\frac{\alpha}{2}\sum_{i=1}^{3}\sigma_i v_i\right), \tag{3.15}$$

where σ_i are the Pauli matrices with $i \in \{1,2,3\}$. The global rotation matrix R_2 is operating in the same way on both atoms in the combined Hilbert space and can be expressed as

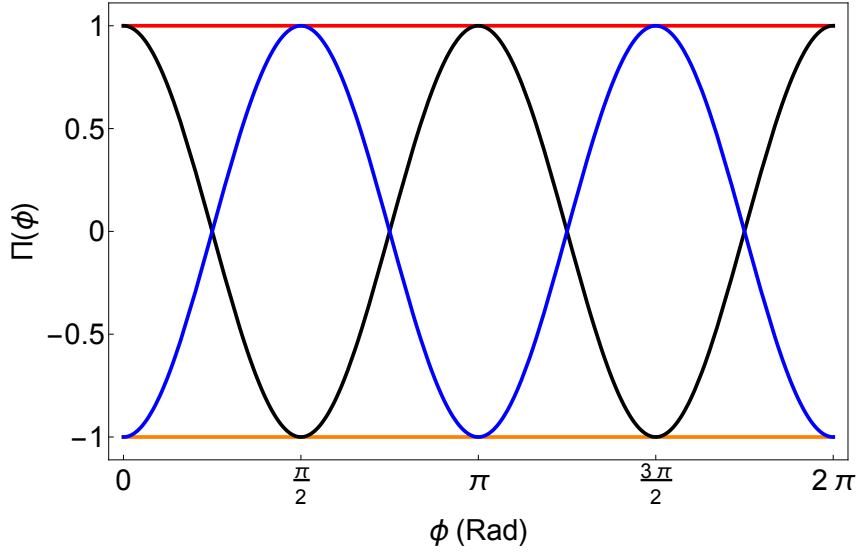$$R_2(\vec{v},\alpha) = R(\vec{v},\alpha) \otimes R(\vec{v},\alpha). \tag{3.16}$$

Figure 3.2.: Expected parity signal for the four Bell states. The figure shows the parity signal Π as a function of the phase ϕ. The red and orange curves correspond to the states $|\Psi^+\rangle$ and $|\Psi^-\rangle$, respectively. The two states $|\Psi^\pm\rangle$ show a constant parity signal. On the other hand, the black and blue curves correspond to $|\Phi^+\rangle$ and $|\Phi^-\rangle$, respectively. These parity signals oscillate as ϕ is changed from 0 to 2π.

The employed analysis pulse has an area of $\alpha = \pi/2$ and a rotation axis $\vec{v} = (\cos(\phi), \sin(\phi), 0)$ such that the modified density matrix can be written as

$$\widetilde{\rho} = R_2\Big((\cos(\phi), \sin(\phi), 0), \pi/2\Big)\rho R_2^\dagger\Big((\cos(\phi), \sin(\phi), 0), \pi/2\Big). \tag{3.17}$$

Therefore, this pulse rotates around an axis that lies in the equatorial plane with a variable phase ϕ defining the rotation axis. The *parity* $\Pi(\phi)$ is defined according to the expression

$$\Pi(\phi) := \widetilde{P}_{\uparrow\uparrow} + \widetilde{P}_{\downarrow\downarrow} - \widetilde{P}_{\uparrow\downarrow} - \widetilde{P}_{\downarrow\uparrow}. \tag{3.18}$$

The parity $\Pi(\phi)$ only contains experimentally accessible quantities as the different populations can be measured with the double state detection protocol outlined in section 2.4.3.3. The evaluation of expression 3.18 yields the compact expression

$$\Pi(\phi) = 2\mathrm{Re}(\rho_{\uparrow\downarrow,\downarrow\uparrow}) + 2\mathrm{Im}(\rho_{\uparrow\uparrow,\downarrow\downarrow})\sin(2\phi) + 2\mathrm{Re}(\rho_{\uparrow\uparrow,\downarrow\downarrow})\cos(2\phi). \tag{3.19}$$

Figure 3.2 shows the theoretically expected behavior of $\Pi(\phi)$ for all four maximally entangled Bell states. Equation 3.19 shows that the parity oscillates as ϕ is changed if the coherence term $\rho_{\uparrow\uparrow,\downarrow\downarrow}$ is populated. Therefore, this feature will become important for the maximally entangled states $|\Phi^\pm\rangle$. On the other hand, the states $|\Psi^\pm\rangle$ show a constant parity $\Pi(\phi) = \pm 1$. From a measurement of $\Pi(\phi)$ the coherence terms in the density matrix can be inferred. Together with a direct measurement of the populations $P_{i,j}$, the fidelities defined in equation 3.13 can be calculated. The technique of parity oscillations to characterize quantum states of two or more particles has been pioneered in the field of trapped ions in the group of David Wineland [118, 143].

3.4. Experimental Entanglement via Quantum State Carving

3.4.1. Normal Mode Spectra with One and Two Atoms

Before the carving technique for the generation of entanglement between the two neutral atoms can be applied, the atoms need to be initialized in a well defined spin configuration. As outlined in section 2.4.1, a right-circular pump laser on the $|\uparrow\rangle \leftrightarrow |e\rangle$ transition optically pumps the atoms into the state $|\uparrow\rangle$. When attempting to pump two atoms with this pumping scheme while the atoms and the pumping laser are on resonance with the cavity, a problem occurs. As soon as the first atom is pumped to $|\uparrow\rangle$, the corresponding normal mode splitting reduces the intracavity intensity of the pumping light by a factor of $(1 + 2C)^2$ (see section 2.4.3.1) and hampers the pumping of the second atom into the state $|\uparrow\rangle$ [86]. A way to prevent this is to detune the atoms from the cavity resonance by changing the optical power of the 1064 nm dipole trap laser. This induces an ac-Stark shift and thus detunes the atoms. The first atom that has been pumped does not completely block the cavity and some pump light can enter to pump the second atom as was outlined in section 2.4.1. After a pump interval of 170 µs, the overlap of the generated state with $|\uparrow\uparrow\rangle$ is 93%. Employing a global π rotation (see section 2.4.2) after the pumping allows for the preparation of the state $|\downarrow\downarrow\rangle$. To improve the fidelity with $|\downarrow\downarrow\rangle$, a state detection protocol is employed subsequently. The atoms are irradiated with resonant laser light impinging transversally on the cavity axis to perform the fluorescence state detection which was introduced in section 2.4.3.2. If one of the atoms still occupies the state $|\uparrow\rangle$, the scattered photons will be collected in the cavity mode and detected with single photon counting modules monitoring the output mode of the cavity. The absence of scattered photons in this state detection interval is employed as a herald such that a state with an overlap of 99% with $|\downarrow\downarrow\rangle$ can be prepared. Subsequently, a global π rotation can be employed to generate $|\uparrow\uparrow\rangle$ with a similar fidelity.

The pumping of one or of two atoms into the coupling state $|\uparrow\rangle$ can be verified with a spectroscopic measurement [144]. This measurement can be performed in two different ways. For the first technique, the transmission of a laser beam through the cavity is measured with single-photon detectors. The frequency of the laser light is scanned symmetrically around the cavity resonance over a range of 40 MHz . The respective data for zero, one and two atoms occupying the state $|\uparrow\rangle$ are shown in figure 3.3. For the empty cavity, a Lorentzian profile can be observed that shows a maximal transmission on cavity resonance. This maximum is defined by the different mirror reflectivities of the employed cavity. The value for the coupling strength g depends on the number of the coupling atoms N inside the cavity. The separation of the two peaks in the normal mode spectra is $2 \times g(N)$. The Tavis-Cummings model predicts a $\sqrt{N}$ behavior for $g(N)$ as was outlined in section 2.1. From the fit to the experimental data, the ratio of the respective coupling strengths $g(N)$ for one and two coupling atoms can be extracted. The ratio assumes a value of $g(2)/g(1) = 1.45 \pm 0.05$ which is consistent with $\sqrt{2} \approx 1.41$ within the error bar.

The second technique to quantify the presence of properly pumped coupling atoms inside the cavity is a normal mode spectroscopy in reflection. The reflection signals for zero, one
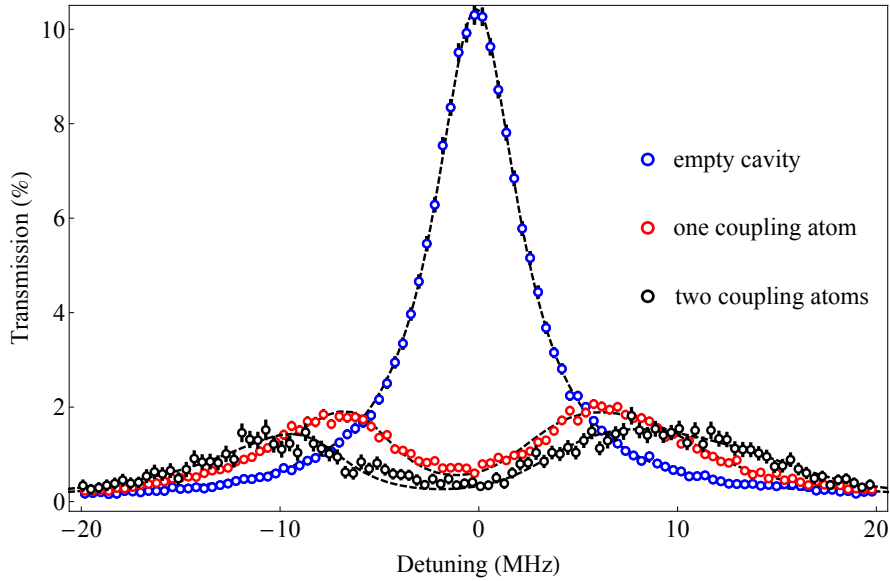
Figure 3.3.: Normal mode spectrum in transmission for zero, one and two coupling atoms. The plot shows the Lorentzian transmission profile for the empty cavity (blue data points). The red data points correspond to the case where one atom occupies the state $|\uparrow\rangle$. After two atoms are pumped to $|\uparrow\uparrow\rangle$, the black data points are observed. The black dashed lines represent a fit to the data that takes into account the thermal movement of the atoms in the trapping potential and the associated ac-Stark shift [44]. The detuning on the horizontal axis is measured with respect to the empty cavity resonance.

and two coupling atoms are shown in figure 3.4. For the parameters of the employed cavity, the reflectivity of the atom-cavity system on resonance is almost the same for the case of an empty cavity and the case in which a single or two coupling atoms are present. The fit in figure 3.4 reveals a value of $g(2)/g(1) = 1.28 \pm 0.05$. If the interatomic distance is too big, the maximal increase of the coupling strength by a factor of $\sqrt{2}$ is not reached due to the beating pattern between the blue-detuned intracavity trapping laser and the cavity mode at 780 nm. This beating pattern leads to an effective reduction of g because the atoms are not trapped at the positions of the highest coupling strength (see section 2). To minimize this effect, only atom pairs satisfying $2\,\mu m \leq d \leq 12\,\mu m$ are accepted where d is the interatomic distance. The center of mass of the atom pair is actively positioned to the center of the cavity by tilting a glass plate in the path of the 1064 nm trapping laser. The tilting of the glass plate is performed with a galvanometric scanner.

The data points shown in figure 3.3 and 3.4 are typically averaged over 10^4 measurements. In an actual experiment where a gate protocol is performed, a single state detection measurement is needed to check the proper pumping of the atoms in the cavity. This can be achieved in a few microseconds via a measurement of the transmission through the cavity on resonance or via a fluorescence measurement. The differences between these two state detection methods were outlined in section 2.4.3.
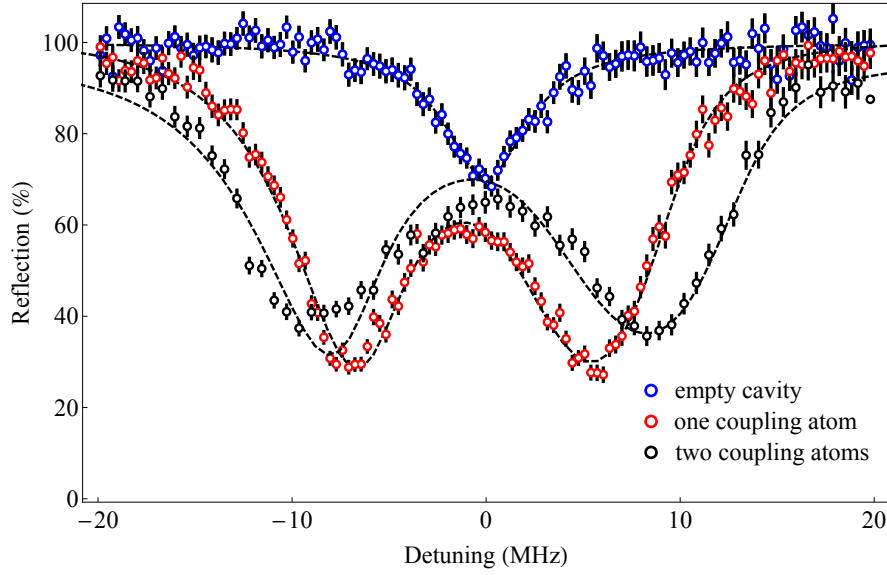
Figure 3.4.: Normal mode spectrum in reflection for one and two coupling atoms. The plot shows cavity reflection spectroscopy data for zero, one and two coupling atoms. In absence of coupling atoms in the cavity (blue data points), the cavity reflectivity on resonance amounts to 67%. This value is only slightly affected when a single or two coupling atoms are present in the cavity (red and black data points, respectively). When pumping two atoms into the state $|\uparrow\uparrow\rangle$, the splitting between the two normal modes ideally increases by a factor of $\sqrt{2}$. The black dashed lines represent a fit taking into account the thermal movement of the atoms inside the trapping potential [44].

3.4.2. Calibration of Raman Pulses for Qubit Rotations with one Atom

As outlined in section 3.1, a necessary prerequisite for the generation of entanglement between the two intracavity atoms is global control over the atomic qubits. The necessary qubit rotations require a precise gauging of the Raman lasers. The atoms are addressed with a pair of Raman lasers impinging from the side of the cavity in the same spatial mode. The corresponding beam has a waist of 30 μm and a wavelength of 795 nm. Both Raman beams are derived from the same laser oscillator such that two phase-stable beams are available. The 6.835 GHz gap between the two beams is established with a fiber-based electro-optical modulator and the fine adjustment to tune the two beams to two-photon resonance is performed with an additional acousto-optical modulator [100]. For all experiments with two intracavity atoms in this thesis, a Rabi frequency of $\widetilde{\Omega}_{\mathrm{Rabi}} = 62.5\,\mathrm{kHz}$ was chosen such that a π pulse can be executed in 8 μs. The two-photon Rabi frequency $\widetilde{\Omega}_{\mathrm{Rabi}}$ depends on the two single-photon Rabi frequencies of the two respective transitions Ω_C and Ω_P, the single-photon detuning Δ and the two-photon detuning δ. The subscripts P and C stand for the control and probe beam, respectively. The general expression for the two-photon Rabi frequency is given by [145]

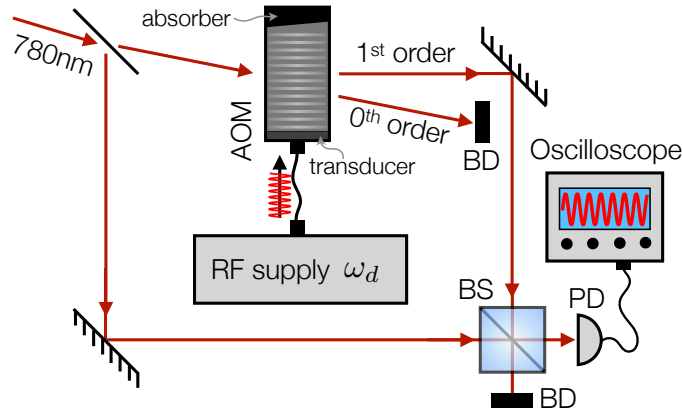$$\widetilde{\Omega}_{\mathrm{Rabi}} = \sqrt{\Omega_R^2 + \tilde{\delta}^2} \tag{3.20}$$

Figure 3.5.: Test setup to study frequency pulling of acousto-optical modulators. A 780 nm laser beam is sent through an acousto-optical modulator (AOM) that is supplied with a radio frequency signal (RF). The radio frequency source operates at the drive frequency ω_d. The first diffraction order is interfered with the unshifted beam on a beam splitter (BS). The other BS output port is sent into a beam dump (BD). The resulting beat signal is monitored on a photodiode (PD) attached to an oscilloscope.

where $\tilde{\delta} = \delta + \Omega_C^2/(4\Delta) - \Omega_P^2/(4\Delta)$ and $\Omega_R = \frac{\Omega_P \Omega_C}{2\Delta}$. Equation 3.20 only holds in the limit where $\gamma \ll \Delta$. This limit is established in the experiment, where $\Delta = 131\,\mathrm{GHz}$.

3.4.3. Frequency Shifting of Acousto-Optical Modulators

During the course of this thesis, it became clear that the employed acousto-optical modulators (AOMs) that define the frequencies of the Raman control and the Raman probe laser show an unexpected behavior of frequency shifting. This means that the frequency of the beam corresponding to the first diffraction order after the AOM deviates from the expected value of $\omega_{\mathrm{optical}} + \omega_d$. Here, $\omega_{\mathrm{optical}}$ and ω_d are the frequencies corresponding to the optical input signal and the radio frequency signal used as an input for the AOM, respectively. The effect occurs whenever the AOM is operated in a pulsed mode. With decreasing pulse length, the frequency of the first order beam deviates increasingly from the expected frequency. Initially, the effect was not known, but experiments with Raman pulses of different duration interacting with an atom in the cavity indicated a frequency dependence of the pulses depending on the pulse length.

To demonstrate this behavior, a test setup was built. A schematic diagram of this setup is shown in figure 3.5. In the test setup, a beam of 780 nm light is initially split into two parts. The first part passes an AOM that is supplied with a 106 MHz signal from a radiofrequency source. The 0th order is sent into a beam dump while the first diffraction order is interfered with the original beam on a beam splitter (BS). The resulting interference signal is monitored with a photodiode and read out with an oscilloscope. The RF supply can be operated in pulsed mode with a variable temporal length of the RF pulses entering the AOM. Typical experimental pulse lengths are on the order of microseconds.
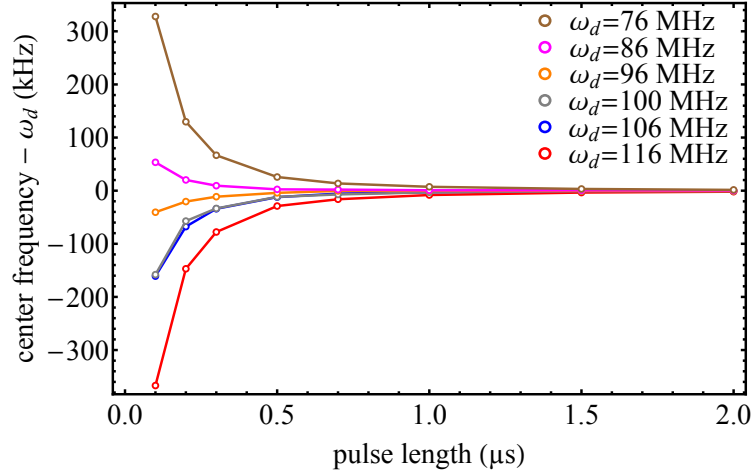
Figure 3.6.: Frequency shifting of an acousto-optical modulator. An acousto optical modulator is driven with an external frequency ω_d. The pulse duration of the applied radio frequency pulse is varied between $0.1\,\mu s$ and $2.0\,\mu s$. The AOM is specified for a frequency of $106\,\text{MHz}$ according to the datasheet. The graphics shows the deviation from the drive frequency as a function of the pulse duration.

The effect was investigated for different pulse lengths between $100\,\text{ns}$ and $2.0\,\mu s$. To this end, the interference signal of the unshifted and the shifted beam was observed with the photodiode. The observed data are Fourier transformed to extract the frequency spectrum. Subsequently, the center of the frequency spectrum was extracted. Figure 3.6 shows the deviation of the center frequencies from the AOM design frequency. For a drive frequency of $91\,\text{MHz}$, the effect vanishes, but increases if the drive frequency deviates from this value. Employing a network analyzer the eigenfrequency of the internal LC circuit of the AOM is determined. It assumes a value of $109.7\,\text{MHz}$. The AOM was specified for a center frequency of $106\,\text{MHz}$. A possible explanation for the frequency shifting effect is the following. The AOM can be described as a harmonic oscillator with a damping term. If such a harmonic oscillator is driven at a frequency that deviates from its eigenfrequency ω_0, it needs time to adjust to the driving frequency ω_d. Initially, it will start with a mixture of the external driving frequency and its eigenfrequency. Mathematically, this can be expressed as

$$x(t) = A(\omega_d)\Big(\sin(\omega_d t) - \frac{\omega_d}{\omega_{\text{damp}}} e^{-\zeta t} \sin(\omega_{\text{damp}} t)\Big). \tag{3.21}$$

Here, $x(t)$ denotes the deviation from the position of rest. In the presence of a damping term ζ, this frequency is changed to $\omega_{\text{damp}} = \sqrt{\omega_0^2 - \zeta^2}$, where ω_0 is the undamped eigenfrequency. If $\omega_d \neq \omega_{\text{damp}}$, the system will have two different frequency components initially. While the component ω_{damp} is dampened out exponentially, the system will asymptotically approach the drive frequency.

3.4.4. AOM Frequency Shifts Observed via an Atom

The AOM frequency shifts described in section 3.4.3 can also be observed in calibration measurements with a single atom. To demonstrate this, a sequence of three Raman pair pulses is employed. The time between the pulses is fixed to $t_{\text{off}} = 1.3\,\mu s$. As in the measurements for the AOM characterization, the pulse duration t_{on} is scanned between $0.1\,\mu s$ and $2.5\,\mu s$. The phase of the second pulse is changed by π radians compared to the first and the last pulse such that the rotation direction on the Bloch sphere is reversed compared to these pulses. After the three-pulse sequence, the state of the atom is read out via a fluorescence state detection. To obtain a spectrum that can later be evaluated, the two-photon detuning δ is scanned via a scan of the Raman control laser frequency. The Raman probe laser frequency is kept at a constant value. The rotation of the single atomic qubit can mathematically be described as a rotation matrix of the form $R(\vec{v},\alpha) = R(\alpha\vec{v})$ as defined in equation 3.15. Here, the vector $\vec{v}$ is a normalized vector that determines the rotation axis while α defines the rotation angle. The product $\alpha\vec{v}$ thus contains information about both the rotation angle and the rotation axis. The amount of atomic population in the state $|\uparrow\rangle$ as a function of the two-photon detuning δ can be modelled by the application of rotation matrices to the qubit that is initially prepared in the state $|\uparrow\rangle$. The two-photon detuning defines the z component of the rotation axis. As soon as two-photon resonance is established, this z component vanishes and the rotation axis lies in the x-y plane.

For the theoretical model, an offset of the two-photon detuning δ_{on} during the rotation pulses and δ_{off} between the rotation pulses are introduced. The Rabi frequency is denoted $\widetilde{\Omega}_{\text{Rabi}}$ and it was chosen as $\widetilde{\Omega}_{\text{Rabi}} = 250\,\text{kHz}$. With this notation, the atomic state $|\psi_{\text{out}}\rangle$ after the application of the described three pulse calibration sequence can be written as

$$|\psi_{\text{out}}\rangle = R\Big(2\pi t_{\text{on}}(0,\widetilde{\Omega}_{\text{Rabi}},\delta + \delta_{\text{on}})\Big) \cdot R\Big(2\pi t_{\text{off}}(0,0,\delta + \delta_{\text{off}})\Big) \qquad (3.22)$$
$$\cdot R\Big(2\pi t_{\text{on}}(0, -\widetilde{\Omega}_{\text{Rabi}},\delta + \delta_{\text{on}})\Big) \cdot R\Big(2\pi t_{\text{off}}(0,0,\delta + \delta_{\text{off}})\Big)$$
$$\cdot R\Big(2\pi t_{\text{on}}(0,\widetilde{\Omega}_{\text{Rabi}},\delta + \delta_{\text{on}})\Big) |\uparrow\rangle .$$

The experimental data showing the population in $|\uparrow\rangle$ after this particular protocol are plotted in figure 3.7. The model outlined in equation 3.22 serves as a fit model for this dataset. The fit (solid black line in figure 3.7) yields all parameters occuring in equation 3.22. For the chosen parameters in this particular example, on two-photon resonance, three $\pi/2$ pulses are applied to the atom. The middle pulse rotates the atomic qubit in the opposite direction compared to the first and the third pulse. The net result is a $\pi/2$ pulse applied to an atom initially prepared in $|\uparrow\rangle$. Thus, a 50% chance to observe the atom in the state $|\uparrow\rangle$ is expected when the two-photon detuning vanishes ($\delta = 0$). This can indeed be observed in the data in figure 3.7.

To observe the effect of AOM frequency shifts, the time between the pulses was kept constant at $t_{\text{off}} = 1.3\,\mu s$ while the pulse duration t_{on} was scanned. Similar spectra as the one shown in figure 3.7 were measured for $0.1\,\mu s \leq t_{\text{on}} \leq 2.5\,\mu s$ and the offset in the two-photon detuning δ_{on} was extracted from the fit. The observed AOM frequency shifts for short pulse durations (section 3.4.3) lead to a dependence of the offset parameter δ_{on} on the pulse duration, similar to the results observed in figure 3.6. Figure 3.8 shows the
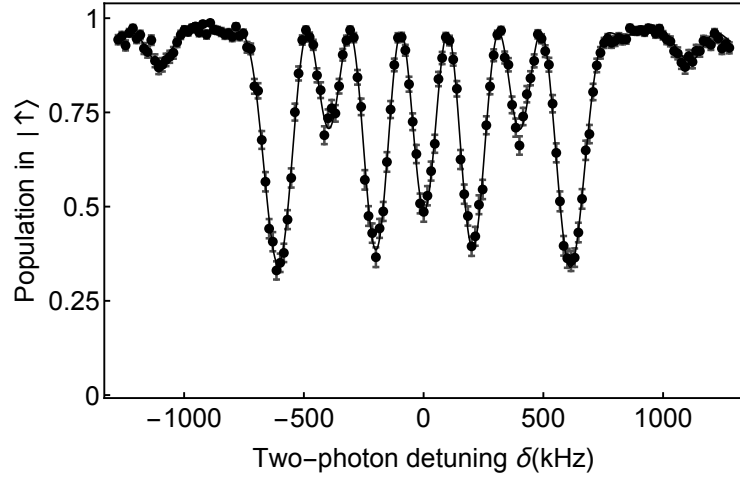
Figure 3.7.: Three-pulse calibration protocol. The plot shows experimental results of a state detection measurement as a function of the two-photon detuning after a three pulse sequence. The error bars are standard deviations from the mean. The solid line represents a fit to the data based on the model described in equation 3.22. The fit yields the parameters $t_{on} = 1.02\,\mu s$, $t_{off} = 1.28\,\mu s$, $\delta_{on} = -4\,kHz$, $\delta_{off} = -2\,kHz$, $\widetilde{\Omega}_{Rabi} = 253\,kHz$.
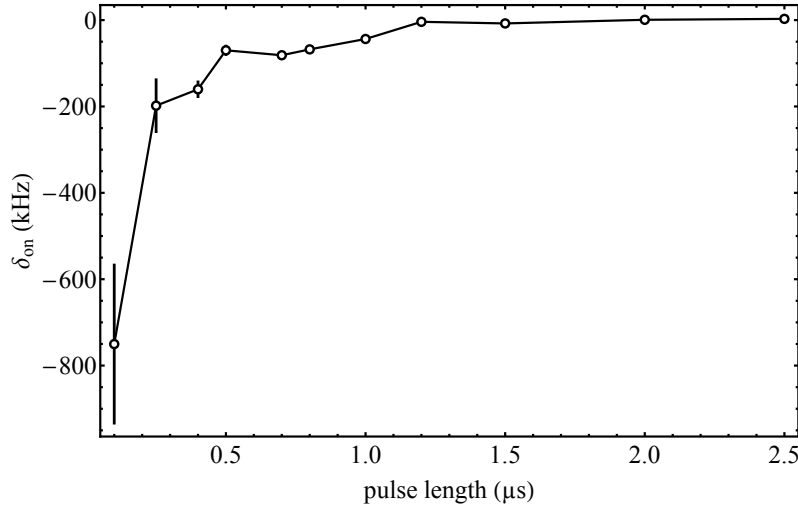
Figure 3.8.: AOM frequency shifts from a measurement on the atom. The plot shows the offset in the two-photon detuning δ_{on} when Raman pulses are applied to the atoms. The pulse duration t_{on} is scanned while the time between the pulses is kept at a constant value of $t_{off} = 1.3\,\mu s$. For decreasing pulse durations, δ_{on} deviates increasingly from zero.

experimentally observed results. A similar behavior as the one observed in section 3.4.3 is apparent. The employed AOMs in the two different measurements were not the same, but the qualitative behavior is very similar. The effect of AOM frequency pulling needs to be taken into account when calibrating the Raman pulses for any QIP protocol like the quantum state carving or the quantum gate protocol.
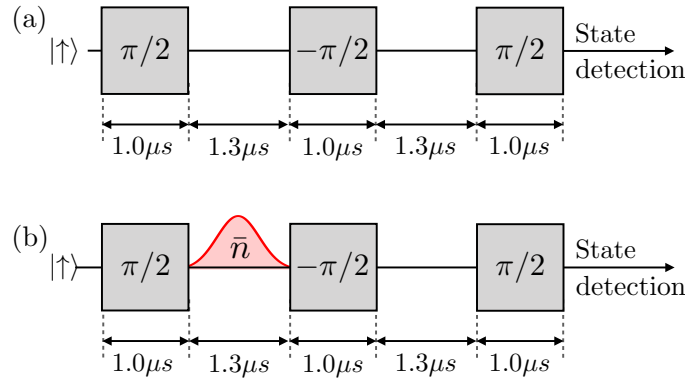
Figure 3.9.: Timing of calibration protocol without and with interleaved light reflection.
(a) Three $\pi/2$ pulses are applied to the atom. The second pulse rotates the atomic qubit into
the opposite direction. In between the pulses, a temporal gap of $1.3\,\mu s$ is inserted. The pulses
have a length of $1.0\,\mu s$ each. (b) A coherent pulse is reflected from the cavity in between the first
and second qubit rotation pulse. Photons in this pulse impart a π phase shift on the combined
atom-photon state.

Additionally, the ac-Stark effect imparted onto the atoms via the Raman lasers needs to
be considered. In the measurements shown in figure 3.8, the ac-Stark effect was equal for
all pulse durations as the laser power was held at a constant value. If the laser power is
increased to achieve a higher Rabi frequency and thus a bigger rotation angle in a given
time interval, the atom and the Raman lasers can run out of phase in the time interval
when the lasers are switched off with the AOMs. A solution to this problem is to slightly
change the RF frequency supplying the AOMs in between the Raman pulses. With this
method the Raman lasers and the atom in the cavity can be synchronized such that the
same phase evolution is guaranteed over the entire time of the experimental protocol. The
described effects are especially dominant for pulse durations below $\sim 1\,\mu s$. Therefore,
whenever it is not necessary to make the desired protocol as short as possible, longer pulse
times are easier to handle.

3.4.5. Calibration Sequence with an Inverleaved Photon

The method described in section 3.4.4 allows to calibrate a desired pulse sequence such
that δ_{on} and δ_{off} vanish while a desired Rabi frequency can be adjusted. The reflection of a
resonant weak coherent pulse from the cavity between these pulses will have an influence
on the observed spectra as the phase of the atomic qubit can be changed by π radians
via the phase shift mechanism outlined in chapter 2.5. An experiment was performed
to observe this effect. Initially, the Raman pulses were calibrated with the same three
pulse protocol outlined in section 3.4.4. After this calibration, a weak coherent pulse was
interleaved between the first and the second pulse. Employing waveplates, the polarization
state of the reflected pulse was set to $|R\rangle$ (right-circular polarization). A diagram showing
the calibration protocol and the protocol containing the photon pulse is shown in figure
3.9. In the case of a true single photon reflected from the cavity, the state generated after

this protocol can be written as

$$|\psi_{\text{out}}\rangle = R\Big(2\pi t_{\text{on}}(0,\widetilde{\Omega}_{\text{Rabi}},\delta + \delta_{\text{on}})\Big) \cdot R\Big(2\pi t_{\text{off}}(0,0,\delta + \delta_{\text{off}})\Big) \tag{3.23}$$
$$\cdot R\Big(2\pi t_{\text{on}}(0,-\widetilde{\Omega}_{\text{Rabi}},\delta + \delta_{\text{on}})\Big) \cdot R\Big(2\pi t_{\text{off}}(0,0,\delta + \delta_{\text{off}})\Big)$$
$$\cdot R\Big(\pi(0,0,1)\Big) \cdot R\Big(2\pi t_{\text{on}}(0,\widetilde{\Omega}_{\text{Rabi}},\delta + \delta_{\text{on}})\Big) |\uparrow\rangle .$$

The photon imprints a π phase shift onto the atomic state. This phase shift can be interpreted as a rotation pulse with the z axis as its rotation axis. In general, an $|n\rangle$ photon Fock state impinging onto the cavity imprints a phase shift of $n \cdot \pi$. Setting $t_{\text{on}} = 1.0\,\mu\text{s}$, $t_{\text{off}} = 1.3\,\mu\text{s}$ and $\delta_{\text{on}} = \delta_{\text{off}} = 0$, the theoretical prediction for the $|\uparrow\rangle$ component of $|\psi_{\text{out}}\rangle$ in equation 3.23 can be plotted as a function of δ and $\widetilde{\Omega}_{\text{Rabi}}$. Likewise, the same can be done for the state $|\psi_{\text{out}}\rangle$ in equation 3.22. The corresponding plots are shown in figure 3.10 (a,b). The respective expected spectra for a Rabi frequency of $250\,\text{kHz}$ are shown in figure 3.10 (c).

In the experiment, a weak coherent pulse is reflected from the cavity. Such a pulse contains a Poissonian distribution of photon numbers. In practice, the coherent pulse is strongly attenuated and contains a mean photon number of $\bar{n} \approx 0.2$. Thus, only the zero-, one- and two-photon contrubutions are relevant for the experimental results. For such low mean photon numbers, the probability to observe three photons is on the order of 0.1% and the higher photon numbers are even stronger suppressed. To fit the experimental data (figure 3.10 (d)) for the three pulse sequence with the coherent pulse interleaved between the first and second pulse, a weighted fit model can be employed. The model contains two contributions of the form $|\langle\uparrow|\psi_{\text{out}}\rangle|^2$ where $|\psi_{\text{out}}\rangle$ is given by equation 3.22 in the case of zero or two photons. In the case of one photon, $|\psi_{\text{out}}\rangle$ is given by equation 3.23. Figure 3.10 (d) shows the experimental data together with the described fit. Clearly, the effect of the pulse reflection is visible when comparing this spectrum to the one in figure 3.7. From the fit, a mean photon number of $(18.0 \pm 0.2)\%$ can be extracted. The method represents a way to extract the mean number of photons that have interacted with the atom in the cavity. Of course, it is also possible to directly measure $\bar{n}$ via single-photon detectors. The error associated with this method arises because the quantum efficiency of the detectors needs to be measured precisely for a good estimate of $\bar{n}$. The described method is more direct in the sense that it actually allows to extract the number of photons that matched the cavity mode and interacted with the atom. The non-modematched photons do not contribute and are thus excluded in the measurements.

3.4.6. Calibration of Raman Pulses with Two Atoms

All entangling protocols described in this thesis rely on the ability to perform precise rotations of two atomic qubits residing inside the cavity. The distance between the two atoms is not actively controlled. In case it is too large, a new atom pair needs to be loaded until a suitable pair is available. The selection of atom pairs is based on fluorescence images employing an EMCCD camera with an exposure time of $300\,\text{ms}$. To calibrate the global qubit rotation pulses for later applications, a technique was developed where the exact sequence of Raman pulses of a desired protocol is applied to the atom pair in a
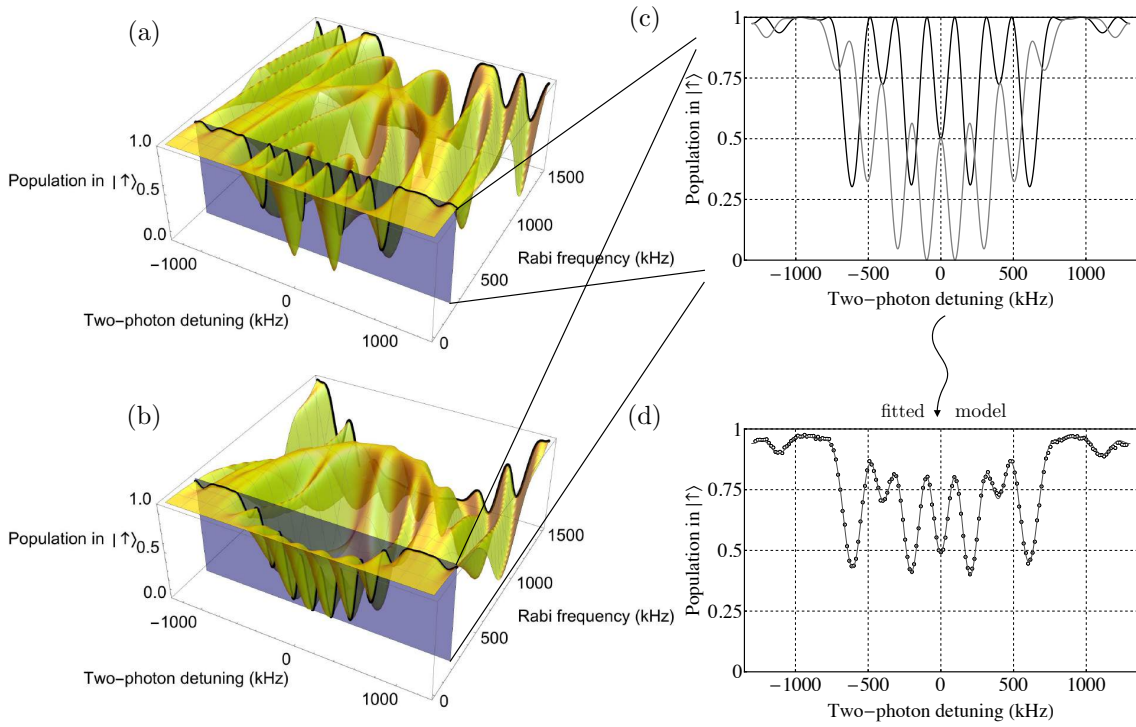
Figure 3.10.: Three pulse sequence without and with interleaved photon. (a) The theoretical model describing the three pulse sequence in section 3.4.4 allows to predict the atomic population in the state $|\uparrow\rangle$ as a function of the Rabi frequency and the two-photon detuning. The purple plane is a cut through the graph at a Rabi frequency of 250 kHz, the Rabi frequency chosen in this calibration experiment. For this particular Rabi frequency, a $\pi/2$ pulse can be executed in 1.0 µs. (b) If a true single photon impinges onto the cavity between the first and second qubit rotation pulse, the associated π phase shift changes the observed spectrum. (c) The plot shows a cut through the 3D plots in (a) and (b) at a Rabi frequency of 250 kHz. The black curve corresponds to the protocol without a photon reflection (same as in figure 3.7) while the gray curve corresponds to the case where exactly one photon is reflected. (d) In an actual measurement, a coherent pulse is reflected from the cavity. Due to the Poissonian photon statistics in such a pulse, the black curve and the gray curve in (c) contribute to the result with the weights corresponding to the respective photon number probability in the pulse. The datapoints can be fitted with this model and the mean number of photons $\bar{n}$ in the pulse can be extracted. Error bars are statistical standard errors and smaller than the size of the data points.

Ramsey-type experiment [35].

Here, an example of such a pulse sequence is presented. A protocol to entangle the two atoms based on the quantum gate mechanism described in section 4.4 requires three Raman pulses in succession, namely a $\pi/2$ pulse followed by $\pi/4$ and another $\pi/2$ pulse. These pulses can be applied to the atoms and their state can be read out afterwards with the double state detection protocol (see section 2.4.3.3) to obtain the populations $P_{\downarrow\downarrow}$, $P_{\uparrow\uparrow}$ and the sum $P_{\uparrow\downarrow} + P_{\downarrow\uparrow}$. The exact timing as chosen in the actual experiments is shown in figure 3.11.

As in section 3.4.4, the two-photon detuning δ is scanned. This scan allows for the measurement of three spectra corresponding to the populations $P_{\downarrow\downarrow}$, $P_{\uparrow\uparrow}$ and $P_{\downarrow\uparrow} + P_{\uparrow\downarrow}$.
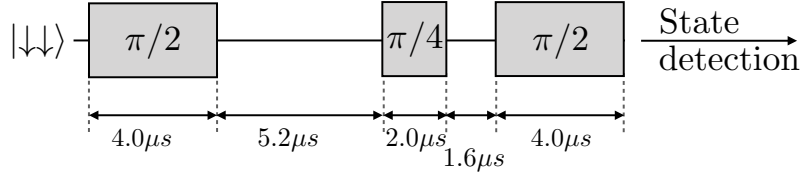
Figure 3.11.: Timing of a three pulse sequence. After initialization of both atoms in the state $|\downarrow\downarrow\rangle$, three pulses are applied. In the real experiment, a weak coherent pulse will be reflected off the cavity in the 5.2 μs interval between the first $\pi/2$ pulse and the $\pi/4$ pulse. For the calibration of the Raman pulses, as described here, this pulse is switched off. The last $\pi/2$ pulse will later be used as an analysis pulse to measure a parity signal.
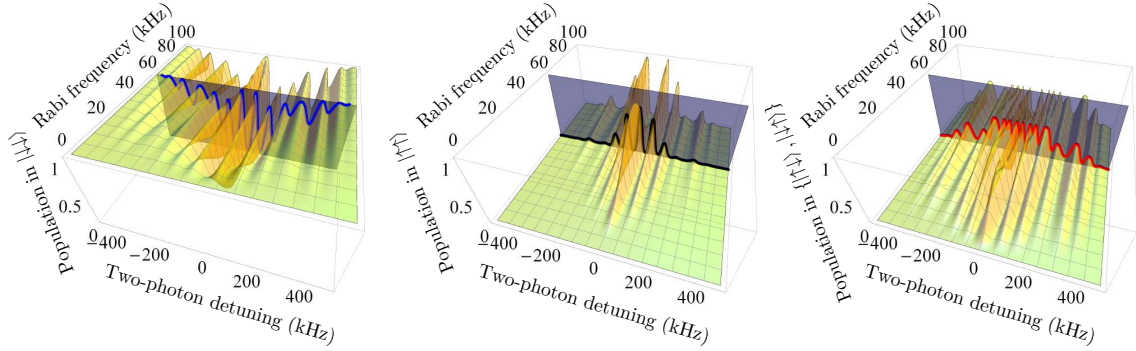

Figure 3.12.: Three spectra to calibrate a sequence of Raman pulses. Initially, both atoms are prepared in the state $|\downarrow\downarrow\rangle$. Afterwards, three pulses are applied: $\pi/2$, $\pi/4$ and another $\pi/2$ pulse. The two-photon detuning is scanned during the application of these pulses and the resulting populations $P_{\downarrow\downarrow}$ (left plot), $P_{\uparrow\uparrow}$ (middle plot) and the sum $P_{\uparrow\downarrow} + P_{\downarrow\uparrow}$ (right plot) are plotted. The cutting plane is located at the desired Rabi frequency of $\widetilde{\Omega}_{\mathrm{Rabi}} = 62.5\,\mathrm{kHz}$. The offset for the two-photon detuning during the time when the lasers are on or off was set to zero in all three graphics. Thus the ideal scenario where the Raman lasers are always on two-photon resonance is shown. If one or both of these two parameters is non-vanishing, the respective spectra are not symmetric around the point of vanishing two-photon detuning anymore, a feature also observable in the experimental data. This asymmetry can be extracted from a fit and compensated later.

Figure 3.12 shows the theoretically expected spectra after this particular protocol. In this plot, the respective spectra are plotted as a function of the two-photon detuning and the Rabi frequency. The purple plane is a cut through the 3D plots at $\widetilde{\Omega}_{\mathrm{Rabi}} = 62.5\,\mathrm{kHz}$, the Rabi frequency chosen in the later atom-atom gate experiments. In this setting, a $\pi/2$ pulse has a duration of $4\,\mu\mathrm{s}$. The theoretical prediction for these spectra can be derived by employing the formalism of rotation matrices $R_2(\vec{v},\alpha)$ developed in section 3.3. After the initialization of the system in the state $|\downarrow\downarrow\rangle$, appropriate rotation matrices of the form $R_2(\vec{v},\alpha)$ are multiplied with this state. The z component of the rotation axis $\vec{v}$ is determined by the two-photon detuning and may have an offset if the two Raman beams are not tuned to two-photon resonance.

The angle α is determined by the temporal length of the respective pulse and the Rabi frequency of the qubit rotations. By convention, the qubit rotations are performed around an axis oriented along the y direction. In the time gaps between the pulses, the y component is vanishing and only a z component exists which can have an offset due to a different
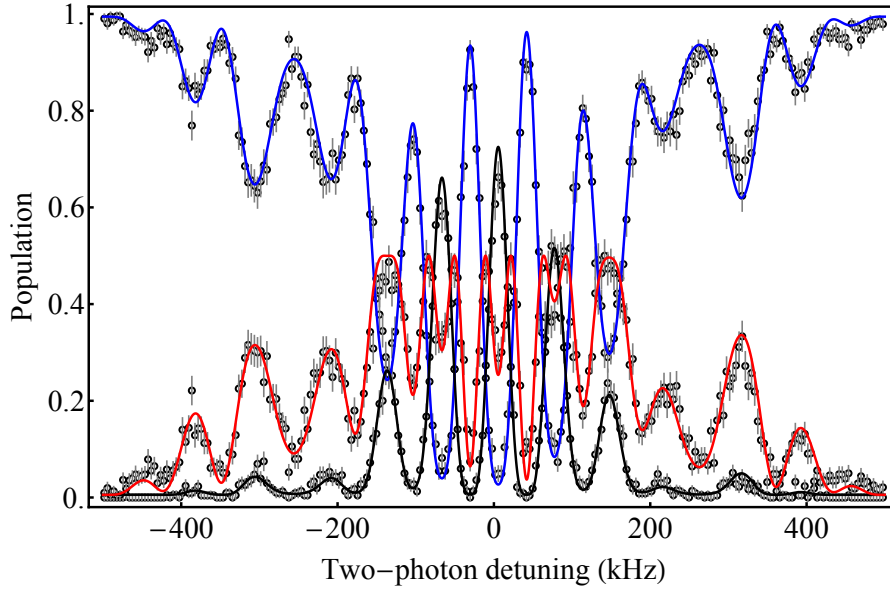
Figure 3.13.: Experimental data for the three Raman spectra. The populations $P_{\downarrow\downarrow}$ (Blue), $P_{\uparrow\uparrow}$ (black) and $P_{\uparrow\downarrow} + P_{\downarrow\uparrow}$ (red) are shown as a function of the two-photon detuning. The solid lines show a fit to the respective data set. The theoretical model delivers three fit models that depend on the same parameters, namely the two offsets of the two-photon detuning during the time intervals when the laser beams are on or off, an amplitude of the signal and the Rabi frequency $\widetilde{\Omega}_{\mathrm{Rabi}}$. All three models were fitted simultaneously with these fit parameters. The fit yields $\widetilde{\Omega}_{\mathrm{Rabi}} = 62.6\,\mathrm{kHz}$, $\delta_{\mathrm{off}} = -8.9\,\mathrm{kHz}$ and $\delta_{\mathrm{on}} = 3.3\,\mathrm{kHz}$.

ac-Stark shift in these intervals. This offset originates from the fact that the atomic qubit and the Raman laser pair can evolve with different frequencies during this time interval.

In total, five rotation matrices have to be multiplied to theoretically describe the sequence depicted in figure 3.11. In the experiment, the two-photon detuning can be scanned via an acousto-optical modulator in the path of the Raman control laser while the Raman probe laser is kept at a constant frequency. The experimentally observed Raman spectra obtained after this particular pulse sequence are shown in figure 3.13.

From a simultaneous fit of all three spectra, the Rabi frequency of the desired qubit transition can be inferred as $\widetilde{\Omega}_{\mathrm{Rabi}} = (62.6 \pm 0.2)\,\mathrm{kHz}$. Furthermore, the fit yields a value for the offset of the two-photon detuning as well as a value for the ac-Stark shift due to the Raman lasers. Especially for temporally short rotation pulses where high optical powers are needed, the effect of the ac-Stark shift is non-negligible and has to be compensated via a change of the respective AOM frequency depending on whether the Raman laser beams are applied to the atoms or not. This can be achieved via a change of the respective RF channel of a direct digital synthesizer supplying the acousto-optical modulator with a radio frequency signal. From the fit shown in figure 3.13, one obtains an offset of the two-photon detuning of $3.3\,\mathrm{kHz}$ during the time intervals when the lasers are applied to the atoms and $-8.9\,\mathrm{kHz}$ when the lasers are switched off between the pulses. If the compensation for the ac-Stark effect is not done properly, the atomic qubit and the Raman laser beams will run out of phase in the intervals when the atoms are not illumunated. The two detunings can be corrected with a precision of a few kHz.
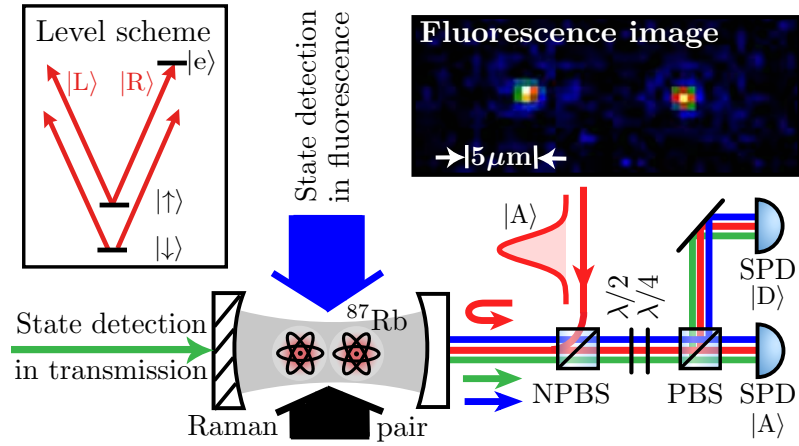
Figure 3.14.: Experimental setup. The experimental setup comprises the high-finesse cavity that contains two trapped ^{87}Rb atoms. Coherent pulses with an antidiagonal polarization $|A\rangle$ are reflected from the cavity and directed into a polarization-resolving setup of single-photon detectors (SPDs). A state detection on the atom pair can be performed via a fluorescence measurement (blue laser beam) or a measurement of the cavity transmission (green laser beam). The left inset shows the simplified level scheme of the two atoms consisting of the states $|\downarrow\rangle$, $|\uparrow\rangle$ and $|e\rangle$. The right inset shows an EMCCD fluorescence image of the atom pair.

3.4.7. Carving with Weak Coherent Pulses

Having carefully calibrated the Raman pulses, we will now focus on the experimental implementation of the carving protocol outlined in 3.1. In the theoretical discussion, it was assumed that single photons are reflected from the atom-cavity system. In the laboratory, a single-photon source was not available and thus the experiments were conducted with weak coherent laser pulses. These pulses can easily be generated with an acousto-optical modulator generating a Gaussian shaped pulse in the time domain. Subsequently, the pulses can be attenuated with a series of neutral density filters. The photon number distribution in such a coherent pulse is a Poissonian distribution

$$P(n) = \frac{\bar{n}^n}{n!}e^{-\bar{n}}, \tag{3.24}$$

where n is the number of photons, $\bar{n} = \sum_{n=0}^{\infty} n \cdot P(n)$ the expectation value of the distribution and $P(n)$ the probability to obtain n photons. As the number of photons is not well defined in a Poissonian distribution, there is a finite probability to obtain multiphoton events. As mentioned in the introduction of chapter 3, the polarization of the incoming photons impinging onto the cavity is antidiagonal ($|A\rangle$). This polarization state of the photons can be expressed as a superposition of right ($|R\rangle$) and left-circularly ($|L\rangle$) polarized components employing the convention that $|A\rangle = (|L\rangle - i|R\rangle)/\sqrt{2}$. Experimentally, the atomic levels are tuned in such a way that only the right-circular component can couple to the cavity if the atom is prepared in the $|\uparrow\rangle$ state as shown in the level scheme in Fig. 3.14.

A relative phase shift of π radians in the atom-photon state [69, 101, 146] between the $|R\rangle$ and $|L\rangle$ component leads to a polarization rotation of 90 degrees if at least one of the atoms occupies the state $|\uparrow\rangle$ and results in a diagonal polarization state $|D\rangle$ at the output. The

output pulses are subsequently sent into a polarization-resolving setup of single-photon detectors (SPDs) (Fig. 3.14). The measurement of $|D\rangle$ polarized light in this setup heralds the presence of at least one coupling atom in the cavity. Thus, this measurement allows to distinguish between the subspace spanned by $\{|\uparrow\uparrow\rangle, |\uparrow\downarrow\rangle, |\downarrow\uparrow\rangle\}$ and the state $|\downarrow\downarrow\rangle$. This is not only true for one reflected photon, but remains true for any photon number, a feature that makes this entanglement scheme robust to the statistics of the incoming optical pulse. Therefore, also coherent pulses containing larger mean photon numbers can be employed to execute the carving scheme. In practice however, the scattering of photons from the reflected laser pulse by the intracavity atoms puts a limit on the mean number of photons in each coherent pulse. It will be shown in section 3.5 that the fidelity of the generated entangled states decreases exponentially with $\bar{n}$. Thus, it is favorable to work with low mean photon numbers.

3.4.8. Experimental Generation of All Four Bell States

The generation of all four maximally entangled Bell states relies on two variations of the carving protocol. These two variations are necessary as three of the maximally entangled Bell states, namely $|\Phi^{\pm}\rangle$ and $|\Psi^{+}\rangle$ are situated in the symmetric part of the two-atom Hilbert space while $|\Psi^{-}\rangle$ is situated in the non-symmetric part. Once one of the three symmetric Bell states is generated, the other two can be generated easily via a suitable global rotation. The singlet state however, cannot be generated out of a symmetric state via global qubit rotations. The reason for this is that the symmetric and non-symmetric parts of Hilbert space are closed under global qubit rotations.
To generate the Bell states $|\Phi^{\pm}\rangle$ and $|\Psi^{+}\rangle$, the carving protocol starts with an initially prepared parallel spin configuration $|\downarrow\downarrow\rangle$. After the two carving steps with coherent pulses containing a mean photon number $\bar{n} = 0.33$, the state $|\Psi^{+}\rangle$ is generated. The polarization of choice for the carving pulses is antidiagonal polarization $|A\rangle$. In principle, any linear polarization state can be employed. The cavity however is slightly birefringent [96, 147] due to strain in the mirror substrates. It was observed experimentally that the two polarization eigenaxes of the cavity are close to antidiagonal and diagonal polarization. This is the reason for the specific choice of the antidiagonal input polarization. The choice of a linear input polarization close to the eigenaxes of the cavity ensures that in the case where no atom couples to the cavity the same polarization state as the input state is reflected from the cavity. If an input state between the two eigenaxes is chosen, the reflected polarization is slightly rotated compared to the input state. This leads to a reduction of the eventual state fidelity as the necessary herald clicks for carving in the employed SPDs are admixed with false positive events. Earlier measurements showed that the maximal splitting of the resonance curves for different polarization states is $410\,\text{kHz}$ [96].

Once the state $|\Psi^{+}\rangle$ is successfully generated, it is straightforward to generate $|\Phi^{\pm}\rangle$ as these states can be obtained from $|\Psi^{+}\rangle$ via a global $\pi/2$ rotation around two different rotation axes (x and y). The respective rotation axis for the generation of $|\Phi^{+}\rangle$ or $|\Phi^{-}\rangle$ is experimentally controlled by the phase of the rotation pulse in the dashed box in figure 3.15. Either the phase of the Raman control or the Raman probe laser can be switched to change the rotation axis. A switch to a different phase profile in the employed direct digital
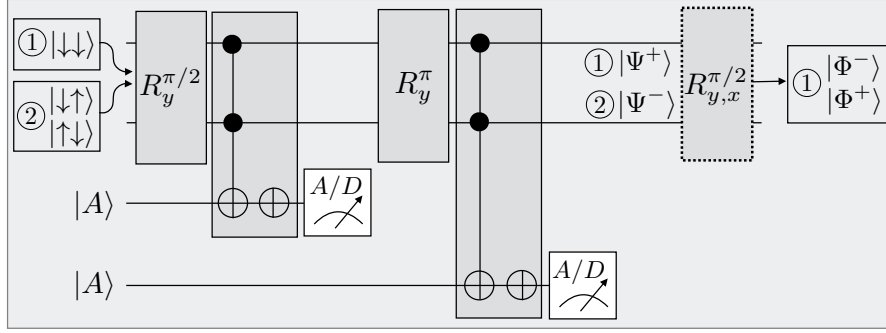
Figure 3.15.: Quantum circuit diagram of the carving protocol. After initializing the atoms in the parallel spin configuration $|\downarrow\downarrow\rangle$ (①), a $\pi/2$ rotation generates the state $1/2(|\uparrow\uparrow\rangle - |\uparrow\downarrow\rangle - |\downarrow\uparrow\rangle + |\downarrow\downarrow\rangle)$. In two carving steps, interleaved with a π rotation to invert the populations, the $|\uparrow\uparrow\rangle$ and $|\downarrow\downarrow\rangle$ components are removed to generate a maximally entangled state $|\Psi^+\rangle$. The dashed box for the final $\pi/2$ rotation is optional and can be applied depending on whether $|\Phi^\pm\rangle$ should be created from $|\Psi^+\rangle$ or not. For the generation of the singlet state $|\Psi^-\rangle$, the atoms are initially prepared in an incoherent superposition of $|\uparrow\downarrow\rangle$ and $|\downarrow\uparrow\rangle$ (②) before the double carving protocol is applied. In this case, the dashed pulse at the end of the protocol can be omitted. The symbol • denotes the atomic control qubits while the symbol ⊕ denotes a NOT operation. The circuit diagram notation for the two carving steps (boxes before the two state detection measurements) is a compact way to express the truth table outlined in equation 3.2.

synthesizer supplying one of the two AOMs setting the frequencies of the two Raman lasers is sufficient to change the rotation axis.

For the generation of $|\Psi^-\rangle$, a different input state is necessary. The choice of an antiparallel configuration like $|\uparrow\downarrow\rangle$ or $|\downarrow\uparrow\rangle$ as an input state for the double carving protocol allows for the generation of $|\Psi^-\rangle$. Experimentally, the states $|\uparrow\downarrow\rangle$ or $|\downarrow\uparrow\rangle$ cannot be generated independently since the atoms are not individually addressed. However, it is possible to generate an incoherent mixture $\frac{1}{2}(|\uparrow\downarrow\rangle\langle\uparrow\downarrow| + |\downarrow\uparrow\rangle\langle\downarrow\uparrow|)$ as outlined in section 2.4.1. A calculation shows that starting from both $|\uparrow\downarrow\rangle$ and $|\downarrow\uparrow\rangle$ the resulting state after the double carving protocol is $|\Psi^-\rangle$. The only difference between starting from $|\uparrow\downarrow\rangle$ and $|\downarrow\uparrow\rangle$ is a global phase of the eventually generated output state. This phase does not play a role. The schematic quantum circuit diagram for the double carving scheme is shown in Fig. 3.15.

To verify the generation of entanglement, the method of parity oscillations is employed. The theoretical foundations of this method were outlined in section 3.1. Fig. 3.16 shows the outcome of the parity signals after the experimental generation of all four Bell states.

As expected from equation 3.18, the parity signal oscillates for the two states $|\Phi^\pm\rangle$ and it is constant for the two states $|\Psi^\pm\rangle$ as the phase ϕ of the analysis pulse is changed. The corresponding measured populations P and the resulting state fidelities are listed in table 3.2. Fidelities of up to 90% with the respective desired Bell states can be achieved with the double carving method. The table also contains a measurement of the state lifetime τ. This measurement will be discussed in detail in section 3.10.

An advantage of the carving scheme is its insensitivity to the mode matching of the incoming pulses to the cavity mode. This mode matching is 92% in the case of optimal adjustment of the respective coupling mirrors and lenses. The remaining 8% of the light is directly reflected from the first cavity mirror without coupling to the cavity mode.
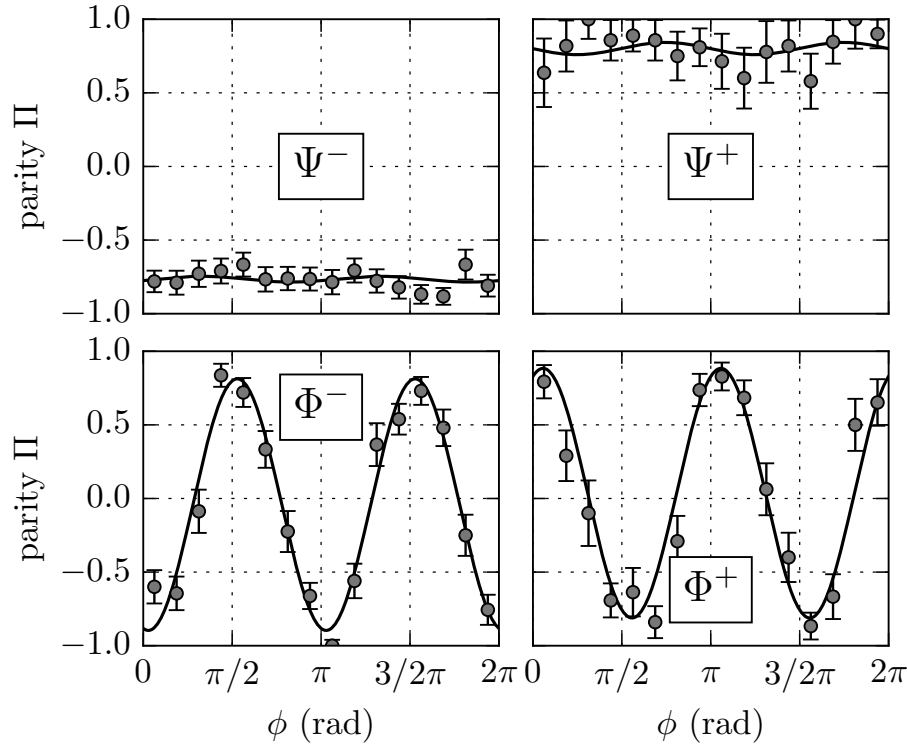
Figure 3.16.: Parity oscillation data The four plots show the parity signals corresponding to the experimentally generated states $|\Phi^{\pm}\rangle$ and $|\Psi^{\pm}\rangle$ as a function of the phase angle ϕ of the analysis pulse. The solid line is a fit to the data with $\text{Re}(\rho_{\uparrow\downarrow,\downarrow\uparrow})$, $\text{Im}(\rho_{\uparrow\uparrow,\downarrow\downarrow})$ and $\text{Re}(\rho_{\uparrow\uparrow,\downarrow\downarrow})$ as free parameters (see equation 3.18). While the states $|\Psi^{\pm}\rangle$ exhibit the characteristic constant behavior of $\Pi(\phi)$, the parity signals for states $|\Phi^{\pm}\rangle$ oscillate as ϕ is changed.

The scheme however, is heralded via the polarization change of the reflected pulse from antidiagonal polarization $|A\rangle$ to diagonal polarization $|D\rangle$. This polarization change can only occur if the photons actually couple to the cavity mode, which is not the case for the non mode-matched component. This component therefore does not contribute to the measured signal. It cannot change its polarization state when it is reflected from the first cavity mirror. Therefore, the property of being heralded makes the carving scheme robust to spatial fluctuations of the incoming mode. On the other hand, the inherently

Table 3.2.: Measured populations P, fidelities F and lifetimes τ of the states created via quantum state carving. The experimental protocol to perform the lifetime measurement will be discussed in section 3.10. The error bars are statistical standard errors.

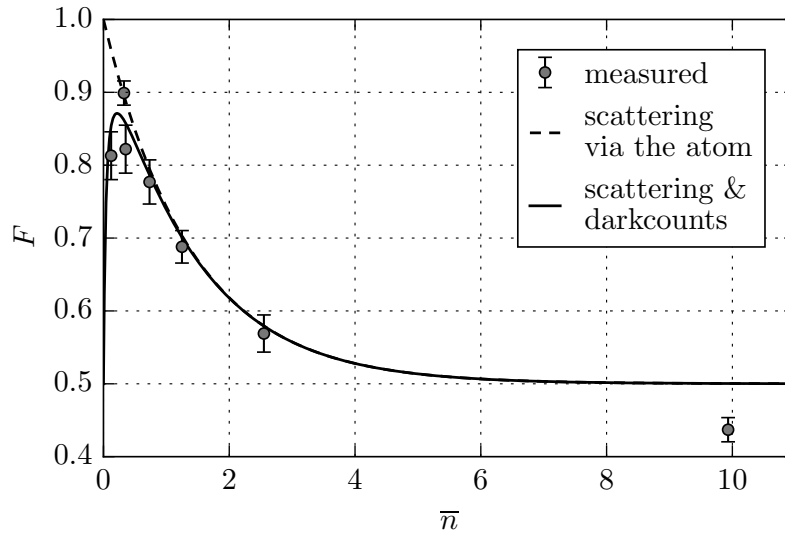| $|\psi\rangle$	$P_{\uparrow\uparrow}$	$P_{\downarrow\downarrow}$	$P_{\uparrow\downarrow} + P_{\downarrow\uparrow}$	F	τ (µs)
$|\Psi^-\rangle$	6(2)%	9(2)%	84(2)%	83.4(1.4)%	204(26)
$|\Psi^+\rangle$	2(2)%	15(5)%	83(5)%	81.9(2.8)%	134(17)
$|\Phi^-\rangle$	40(3)%	54(3)%	6(1)%	89.9(1.7)%	90(19)
$|\Phi^+\rangle$	44(5)%	43(5)%	13(4)%	82.4(3.1)%	—

Figure 3.17.: Entangled state fidelity as a function of the mean photon number $\bar{n}$ in the reflected coherent pulses. The plot shows the fidelity of the states procuced via the double carving protocol with the maximally entangled state $|\Phi^-\rangle$. The dashed line is a theoretical model taking into account the decoherence due to photons scattered by the atom pair. The decay of this exponential curve depends on the cavity parameters and is applied without any fit parameters. The solid line is a theoretical model that additionally takes detector dark counts into account. These dark counts influence the postselection process and become dominant as $\bar{n}$ approaches zero. From the fit, a dark count rate of 0.011 per pulse can be extracted. The highest fidelity of 89.9% is achieved for $\bar{n} = 0.33$ where the solid line reaches a maximum.

probabilistic nature of the scheme means that its efficiency is fundamentally limited. As will be discussed in chapter 4, this is not the case for the atom-atom gate mechanism.

3.5. Fidelity Dependence on the Mean Photon Number

In principle, the carving scheme does not depend on the mean photon number of the coherent optical pulses injected onto the cavity. Thus, also higher numbers of photons could be used to execute the carving method. In practice however, it turns out that the scattering of photons from the carving pulses by the atoms sets an upper bound on the experimentally achievable fidelities. Fig. 3.17 shows the fidelity with an ideally expected $|\Phi^-\rangle$ state as a function of the mean photon number in each of the two reflected pulses employed for carving.

An exponential decay of the measured fidelity is observable as $\bar{n}$ is increased. The reason for this decay is the scattering of photons from the incoming pulse by the intracavity atoms. Such a scattering event scrambles the phase relation between the two atoms and thus leads to a decrease of fidelity. The fidelity approaches a value of $F = 0.5$ because only coherences are scrambled by the scattering processes while the atomic populations are unaffected. This behavior was already predicted in the original proposal for quantum state carving [80]. In
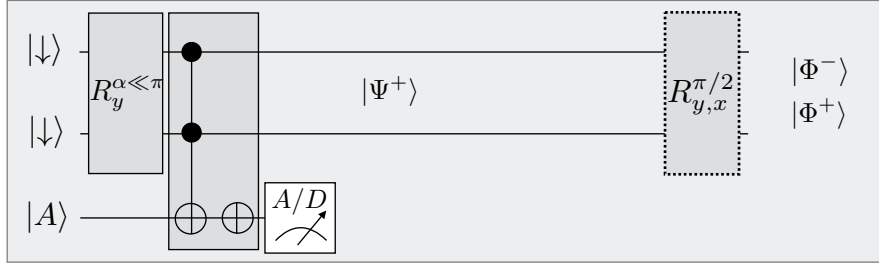
Figure 3.18.: Quantum circuit diagram for the single carving protocol. After initializing both atoms in the state $|\downarrow\rangle$, a global qubit rotation pulse R_y^α is applied. The successive reflection of an initially $|A\rangle$ polarized pulse and the postselection on a polarization rotation to $|D\rangle$ approximately generates $|\Psi^+\rangle$. This state can later be transformed into $|\Phi^+\rangle$ or $|\Phi^-\rangle$ with global $\pi/2$ rotation pulses.

the proposal by Sørensen and Mølmer, an analytical expression for the scattering fraction s was derived. This expression reads

$$s = \frac{4\kappa_r \gamma N g^2}{(\kappa\gamma + Ng^2)^2} \ . \tag{3.25}$$

Inserting the experimental cavity parameters yields $s = 0.36$. As the protocol involved two reflected pulses, the number of scattered photons and thus the decoherence doubles. The dashed line in figure 3.17 shows the exponential decay with this decay constant. If $\bar{n}$ is not too small, the dashed line describes well the experimentally observed data. However, for very low values of $\bar{n}$, the fidelity deviates from the simple exponential model. The reason for this behavior are dark counts of the single-photon detectors used to measure the heralding event. The intrinsic dark count rates of these detectors are typically between 20 and 80 counts per second (cps). Additionally to the intrinsic dark counts, stray light falling on the detectors and light leaking out of the cavity cause false herald clicks. The latter two contributions dominate the intrinsic dark counts of the single-photon detectors. The model thus identifies the dark count contributions as well as the scattering processes from the atoms as the main sources of fidelity reduction. The scattering fraction s can be reduced by increasing the coupling strength g between the atom and the cavity, i.e. by employing a cavity with a smaller mode volume.

3.6. Single Carving Scheme for Entanglement Creation

In the scheme for entanglement creation discussed in section 3.1, two optical pulses were needed to generate a maximally entangled state. There is a slightly modified scheme compared to the double carving protocol that can be employed to approximately generate maximally entangled states with only one reflection of an optical pulse. To achieve high fidelities with this scheme, the value of α should be as small as possible. The idea was proposed theoretically in [80] and removes the second carving pulse at the expense of success probability. The protocol is outlined in figure 3.18.

Starting from a two-atom state $|\downarrow\downarrow\rangle$, a rotation pulse $R_y^\alpha = R_2((0,1,0),\alpha)$ generates a slight
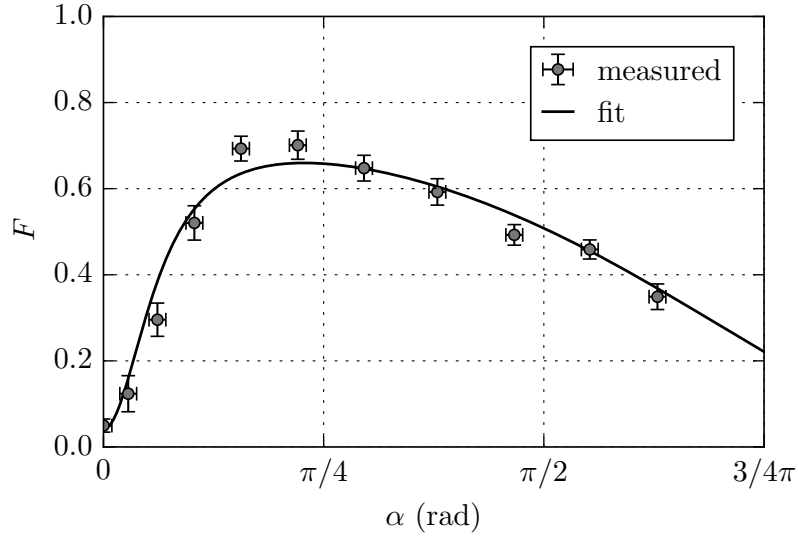
Figure 3.19.: Entanglement creation with single carving protocol. Fidelity of the prepared states with an ideal $|\Phi^-\rangle$ state. The fidelity was measured for different initial rotation angles α. Entanglement was created via a single reflection of an optical pulse with $\bar{n} = 1.2$. The error bars are the standard deviations of the mean. The solid line is a fitted theoretical model taking into account the dark counts of the single-photon detectors employed for heralding. In the case of vanishing dark counts, F would converge to unity as $\alpha \to 0$.

deviation of the coherent spin state initially located at the south pole of the generalized Bloch sphere. The choice of α is a tradeoff between the fidelity of the generated state with a desired Bell state and the efficiency of the entanglement generation process. Generally, the state after the rotation can be written as

$$\sin^2(\alpha/2)\,|\uparrow\uparrow\rangle - 1/2\sin(\alpha)(|\uparrow\downarrow\rangle + |\downarrow\uparrow\rangle) + \cos^2(\alpha/2)\,|\downarrow\downarrow\rangle. \tag{3.26}$$

In the next step, the $|\downarrow\downarrow\rangle$ component is carved out with the single optical pulse and a postselection on the polarization flip from $|A\rangle$ to $|D\rangle$ just as in the double-carving protocol. The resulting state can be written in the form

$$\frac{1}{\sqrt{1/2(3 + \cos(\alpha))\sin^2(\alpha/2)}}\Big(\sin^2(\alpha/2)\,|\uparrow\uparrow\rangle - 1/2\sin(\alpha)(|\uparrow\downarrow\rangle + |\downarrow\uparrow\rangle)\Big). \tag{3.27}$$

This state approaches $|\Psi^+\rangle$ in the limit where $\alpha \to 0$. Once the state 3.27 has been created, it can be transformed into $|\Phi^\pm\rangle$ with a global $\pi/2$ rotation around an appropriate axis. The protocol generates entangled states with a fidelity of $F = 4\cos^2(\alpha/2)/(3 + \cos(\alpha))$. In the limit where $\alpha \to 0$, the fidelity converges to 1. In this limit however, the efficiency of the single carving operation vanishes.

The efficiency of the scheme depends on the residual amount of population in the $|\downarrow\downarrow\rangle$ state which is controlled by α. If all the population is accumulated in this particular state, a polarization flip of the reflected pulse cannot occur. A nonzero efficiency can thus only be achieved if $\alpha \neq 0$. The analytic expression for the efficiency η reads $\eta = 1 - \cos^4(\alpha/2)$. An application of the single carving protocol thus requires a tradeoff between the achieved efficiency and the fidelity. The dark counts of the single-photon detectors used to observe

the herald click dominate as $\alpha \to 0$. The experiment was performed with a mean photon number $\bar{n} = 1.2$ and a $|\Phi^-\rangle$ state was created with α ranging between 0 and 0.63π. The experimentally observed data are shown in figure 3.19. From the fit, a dark count rate of 0.01 per pulse can be extracted. This number is compatible with the value found in the experiments where the double carving protocol was employed. To achieve the highest fidelity, α must not be too small for the dark counts to dominate but also not too high such that the $|\uparrow\uparrow\rangle$ component is still suppressed. For the employed parameters, the highest experimentally observed fidelity $F(\Phi^-) = (70.2 \pm 3.2)\%$ is attained for $\alpha = 0.23\pi$. The achieved efficiency is $\eta = (5.9 \pm 0.1)\%$.

The scheme is a versatile tool and can easily be extended to more than just two atoms. Multi-atom entanglement has been demonstrated in the group of Jakob Reichel in Paris where 40 atoms were entangled within an optical fiber cavity of high finesse [140]. A similar scheme based on quantum Zeno dynamics has also been demonstrated [148]. In the experiments of the Reichel group, the suppression of laser light transmitted through the cavity served as a herald for coupling atoms in the cavity. A modified scheme has been used by the Vuletić group to generate entanglement between 3000 atoms within a cavity [149].

3.7. Measurement of the Husimi Q Distribution

As discussed in chapter 3.1, the Husimi Q distribution offers a way to illustrate the carving process. Any two-qubit state can be assigned a Q distribution that is accessible experimentally. The Q distribution of a coherent spin state is a symmetrical distribution on the generalized Bloch sphere. One can rewrite the definition given in equation 3.8 and obtains for the case of two atomic spins

$$Q(\theta,\phi) = \frac{3}{4\pi} \langle\theta,\phi|\, \rho \,|\theta\phi\rangle \tag{3.28}$$

$$= \frac{3}{4\pi} \langle\downarrow\downarrow|\, \mathbf{R}(\theta,\phi)\rho\mathbf{R}^\dagger(\theta,\phi) \,|\downarrow\downarrow\rangle . \tag{3.29}$$

Equation 3.29 shows that the Husimi Q distribution of ρ can be measured via a global rotation $\mathbf{R}(\theta,\phi)$ defined by the spherical coordinates θ and ϕ and a subsequent state detection of the population in the state $|\downarrow\downarrow\rangle$. Experimentally, ϕ was scanned from 0 to 2π in 30 equidistant steps and θ was scanned from 0 to π in 15 equidistant steps. This results in 450 points on the generalized Bloch sphere. As a first example, a coherent spin state $\frac{1}{2}(|\uparrow\uparrow\rangle - |\uparrow\downarrow\rangle - |\downarrow\uparrow\rangle + |\downarrow\downarrow\rangle)$ was prepared via a global $\pi/2$ rotation from $|\downarrow\downarrow\rangle$. The theoretically expected and experimentally observed Husimi distributions are shown in figure 3.20. Theory and experiment are in good agreement and both show a round distribution on the equator of the generalized Bloch sphere. A slight reduction in the visibility of the observed Q distribution is due to the state detection process which detects the state $|\downarrow\downarrow\rangle$ with 97.4% as was discussed in section 2.4.3.3.

If the double carving scheme is applied to the prepared coherent spin state, an entangled state $|\Phi^-\rangle$ can be generated. The theoretically expected and experimentally observed Husimi distributions are shown in figure 3.21. More specifically, the Mollweide projection of the respective Bloch sphere is depicted.
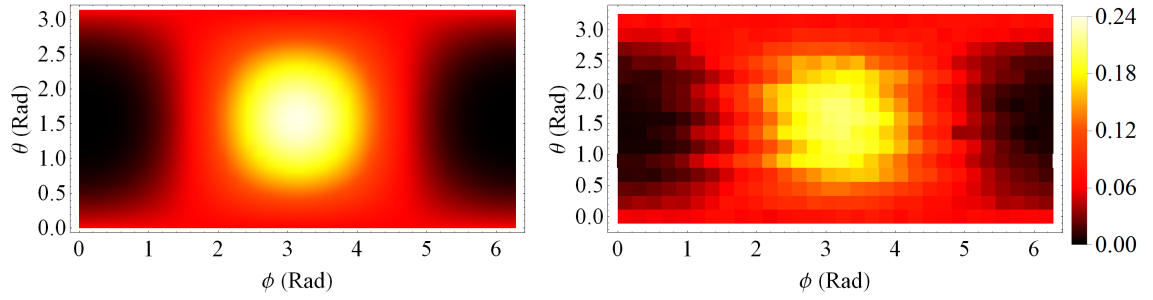
Figure 3.20.: Experimental data of the Husimi Q distribution of a coherent spin state.
Theoretical (left) and experimental (right) Husimi Q distribution for a coherent spin state of the form $\frac{1}{2}(|\uparrow\uparrow\rangle - |\uparrow\downarrow\rangle - |\downarrow\uparrow\rangle + |\downarrow\downarrow\rangle)$). In the experiment, 450 data points were recorded on the generalized Bloch sphere.
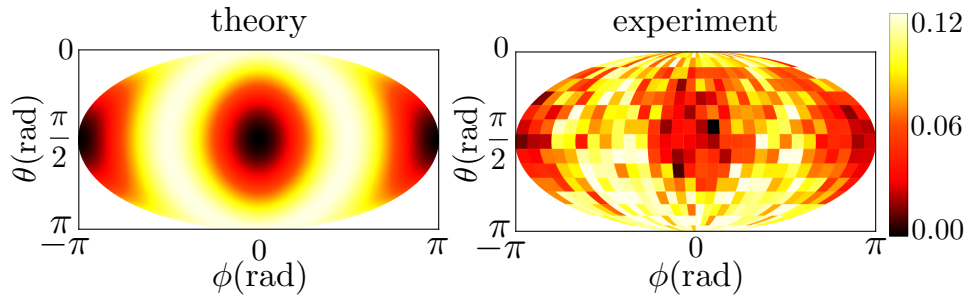

Figure 3.21.: Experimental data of the Husimi Q distribution of $|\Phi^-\rangle$. The left graph shows the theoretically expected Husimi Q distribution for a $|\Phi^-\rangle$ state. A characteristic ring-shaped distribution is expected. The right graph shows the experimentally observed data. The noise in the experimental data is statistical. Both plots show the Mollweide projection of the respective Bloch sphere.

The observed ring shape is characteristic for the maximally entangled Bell states $|\Phi^\pm\rangle$ and $|\Psi^+\rangle$. By an appropriate choice of the rotation axis, a global $\pi/2$ rotation can transform any of these three states into any state out of the same set. In the Husimi representation, such a rotation corresponds to a rotation of the observed ring on the generalized Bloch sphere. In the case of the $|\Phi^\pm\rangle$ states, the observed ring is oriented such that Q is non-vanishing on the north- and the south pole of the generalized Bloch sphere. This is due to the fact that these states have contributions of both $|\uparrow\uparrow\rangle$ and $|\downarrow\downarrow\rangle$.

3.8. Maximum Likelihood Reconstruction of the Density Matrix

In this section a method is described that allows to reconstruct the density matrix of the produced state from the measured Husimi Q distribution [138]. The method is based on a maximum likelihood technique. Based on the available data, the technique determines the most likely underlying density matrix. The method was described in the context of quantum optics for the reconstruction of entangled states in [150] and was later applied to homodyne tomography [151]. It was also employed to reconstruct the contributions of

different Dicke states in an ensemble of atoms in an optical cavity [90, 140, 148, 152]. Here, the method is used for reconstructing the density matrix of a two-particle entangled state. In the following, an iterative algorithm is explained that asymptotically approximates the density matrix based on the data available from the measurement of the Husimi Q distribution [150].

Consider a quantum state ρ that is subject to projective measurements with M_N different outcomes. The measurements can be described by the projection operators $|y_i\rangle \langle y_j|$ where $i = 1,...,M_N$ and

$$\sum_{i=1}^{M_N} |y_i\rangle \langle y_i| = \mathbb{1}. \tag{3.30}$$

A measurement on ρ in a certain measurement basis results in a probability p_i given by $p_i = \langle y_i| \rho |y_i\rangle$. The corresponding experimental quantity is the Husimi Q distribution of the form $Q(\theta,\phi) \propto \langle \theta,\phi| \rho |\theta,\phi\rangle$. This distribution characterizes the overlap of the experimentally generated state with coherent spin states for different pairs of spherical coordinates θ and ϕ. Therefore, there is a set of measurement bases described by projection operators $|(\theta,\phi)_i\rangle \langle (\theta,\phi)_i|$. In the limit of an infinite number of measurements, the observed probabilities $f_i \propto Q(\theta,\phi)$ will approach p_i. In the case of the measurement of a Husimi Q distribution, there are only two possible measurement outcomes. Either zero photon clicks in the fluorescence state detection interval are observed, or a non-vanishing number of clicks is observed. This binary signal corresponds to the operators $|(\theta,\phi)_i\rangle \langle (\theta,\phi)_i|$ and $\mathbb{1} - |(\theta,\phi)_i\rangle \langle (\theta,\phi)_i|$ and the respective probabilities are f_i^1 and $f_i^0 = 1 - f_i^1$. It is convenient to define the likelihood function as $\mathcal{L}(\rho)$, an expression that depends on the measured probabilities f_i. The definition reads

$$\mathcal{L}(\rho) := \prod_{i=1}^{M_N} \langle y_i| \rho |y_i\rangle^{f_i}. \tag{3.31}$$

For the specific case of the Husimi Q distribution, the likelihood function can be expressed as [90]

$$\mathcal{L}(\rho) = \prod_{i=1}^{M_N} (p_i^1)^{f_i^1} \cdot (p_i^0)^{f_i^0} \tag{3.32}$$

where $p_i^1 = \langle (\theta,\phi)_i| \rho |(\theta,\phi)_i\rangle$ and $p_i^0 = 1 - p_i^1$. The goal of the maximum likelihood technique is to determine a density matrix $\rho_{\max}$ which maximizes $\mathcal{L}(\rho)$. For this matrix, the measured probabilities will approach the values of p_i^k such that $f_i^k \approx p_i^k$ holds. To find the desired matrix $\rho_{\max}$, an operator $\mathbf{T}$ is introduced [151] as

$$\mathbf{T}(\rho) = \sum_i \frac{f_i^1}{p_i^1} |(\theta,\phi)_i\rangle \langle (\theta,\phi)_i| + \frac{f_i^0}{p_i^0}(\mathbb{1} - |(\theta,\phi)_i\rangle \langle (\theta,\phi)_i|). \tag{3.33}$$

For the density matrix $\rho_{\max}$, the relation $\mathbf{T}(\rho_{\max}) \propto \mathbb{1}$ holds. Starting with the initial density matrix $\rho^{(0)} \propto \mathbb{1}$ an iterative algorithm can be applied to obtain the density matrix for the next iteration step according to

$$\rho^{(k+1)} = \mathcal{N}\Big(\mathbf{T}(\rho^{(k)})\rho^{(k)}\mathbf{T}(\rho^{(k)})\Big). \tag{3.34}$$

In the last expression, $\mathcal{N}$ denotes the normalization to a unitary trace. It can be shown that in each step, the likelihood function increases monotonically [151].

The iterative algorithm asympotically approaches the desired density matrix ρ_{max}. It should be pointed out that a measurement of the Husimi distribution always measures the symmetric part of the density matrix since the overlap of a non-symmetric state with a coherent spin state is always zero. This is the reason why the Husimi distribution of the $|\Psi^-\rangle$ state is vanishing over the entire Bloch sphere. In our example from section 3.7 the Husimi distribution of the symmetric state $|\Phi^-\rangle$ was measured. This dataset will be used for the reconstruction of ρ_{max} in the following section.

3.9. Maximum Likelihood Reconstruction of a Density Matrix from a Measured Husimi Q Distribution

Figure 3.21 (right part) shows the experimental data of a Husimi Q distribution after the production of a $|\Phi^-\rangle$ state via the double carving protocol. In total, Q was measured at 450 points on the Bloch sphere which corresponds to 450 different measurement bases $|(\theta,\phi)_i\rangle \langle(\theta,\phi)_i|$. Starting with a normalized unit matrix, 200 iterations of the algorithm outlined in section 3.8 yield the density matrix

$$\rho_{\mathrm{max}} = \begin{pmatrix} 0.498 & -0.023 + 0.008i & -0.023 + 0.008i & -0.328 + 0.046i \\ -0.023 - 0.008i & 0.065 & 0.002 & 0.020 + 0.017i \\ -0.023 - 0.008i & 0.002 & 0.065 & 0.020 + 0.017i \\ -0.328 - 0.046i & 0.020 - 0.017i & 0.020 - 0.017i & 0.373 \end{pmatrix}. \tag{3.35}$$

The real and the imaginary part of this density matrix are shown graphically in figure 3.22.

A measurement of the Husimi Q distribution and the successive reconstruction of the density matrix does not allow to distinguish between the states $|\uparrow\downarrow\rangle$ and $|\downarrow\uparrow\rangle$. Thus, in the density matrix shown in figure 3.22, the bars corresponding to the components $|\uparrow\downarrow\rangle \langle\uparrow\downarrow|$ and $|\downarrow\uparrow\rangle \langle\downarrow\uparrow|$ have the same value, the average of the physical values which cannot be accessed independently. The imaginary components of the density matrix are close to zero, a sign that the characteristic ring structure on the Husimi sphere is not rotated around the vertical z axis away from $|\Phi^-\rangle$.

The iterative process to approach ρ_{max} can be visualized by plotting the logarithm of the likelihood function defined in equation 3.32 as a function of the corresponding iteration step. Furthermore, the fidelity with the ideal state $|\Phi^-\rangle$ can be plotted as a function of the respective iteration step. These plots are shown in figure 3.23. The fidelity is defined as

$$F(\rho, |\Phi^-\rangle) = \langle\Phi^-| \rho |\Phi^-\rangle \tag{3.36}$$

and asymptotically approaches a value of $F(\rho_{\mathrm{max}}, |\Phi^-\rangle) = 76.3\%$. It should be noted that in this measurement, the fidelity is not as high as the best achieved fidelities for the generation of the $|\Phi^-\rangle$ state (see table 3.2). The reason is the long duration of the experiment and thermal drifting of the system during the measurement of the full Husimi distribution.
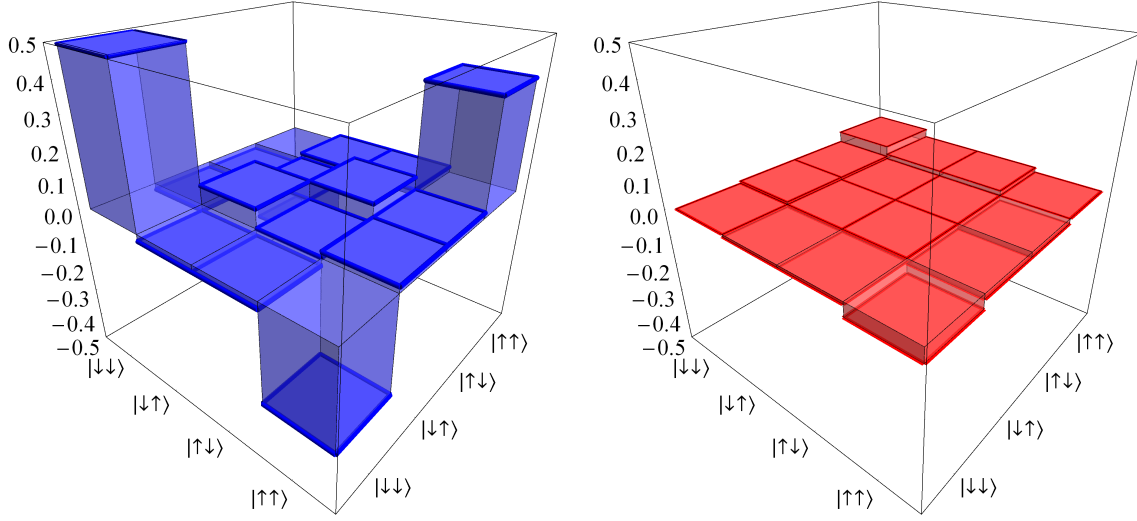
Figure 3.22.: Reconstructed density matrix. The figure shows the real (blue, left) and the imaginary (red, right) parts of the reconstructed density matrix ρ_{max}. The fidelity with the maximally entangled state $|\Phi^-\rangle$ is 76.3%.

Such a measurement typically takes 24 hours. A parity oscillation measurement is much faster (1-2 hours) and thermal spatial drifts i.e. of the Raman beam employed for qubit rotations do not play such a big role on shorter timescales.

It is worthwile to calculate an entanglement measure for the reconstructed density matrix. A good example of such a measure is the concurrence $\mathcal{C}$ [136]. The concurrence of a density matrix ρ describing a two-qubit state is defined as

$$\mathcal{C} = \max(0, \lambda_1 - \lambda_2 - \lambda_3 - \lambda_4) \tag{3.37}$$

where $\lambda_1, \lambda_2, \lambda_3, \lambda_4$ are the eigenvalues (sorted in decreasing order) of

$$R = \sqrt{\sqrt{\rho}\widetilde{\rho}\sqrt{\rho}}. \tag{3.38}$$

Here, the matrix $\widetilde{\rho}$ is defined as $\widetilde{\rho} = (\sigma_2 \otimes \sigma_2)\rho^*(\sigma_2 \otimes \sigma_2)$, where σ_2 is a Pauli matrix[1] and the asterisk denotes complex conjugation. The concurrence assumes a value between zero and one, depending on the amount of entanglement between the qubits. For maximally entangled states, a concurrence of one is reached while separable states have a concurrence of zero. Inserting the reconstructed density matrix ρ_{max} into this definition yields a value of $\mathcal{C} = 0.54$ and thus shows that entanglement was generated.

As a crosscheck, one can also verify that the measured values for the expected probabilities p_i^1 approach the values of the measured Husimi distribution f_i^1. In total, 450 values of f_i^1 were measured on a grid evenly distributed over the entire generalized Bloch sphere.

---

[1]The Pauli matrix σ_2 is defined as $\sigma_2 = \begin{pmatrix} 0 & -i \\ i & 0 \end{pmatrix}$.
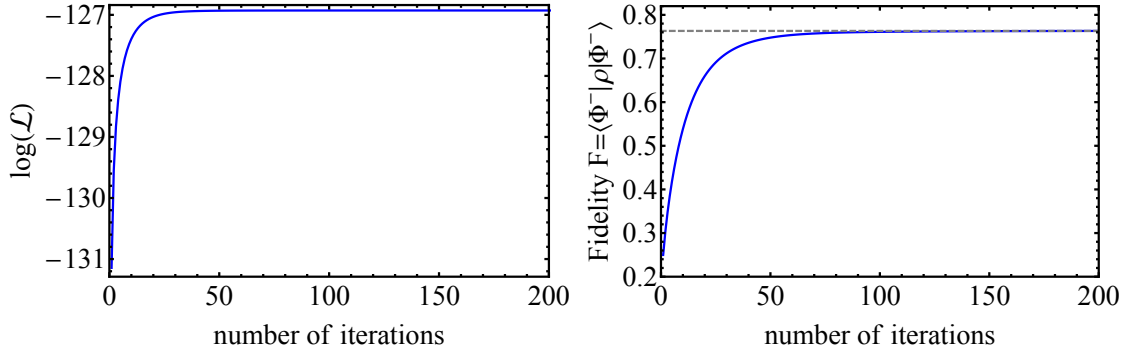
Figure 3.23.: Likelihood and fidelity. Left: Logarithm of the likelihood as a function of the iteration step. The likelihood increases monotonically. Right: Fidelity of the generated state with the ideally expected Bell state $|\Phi^-\rangle$ as a function of the iteration step. The fidelity asymptotically approaches $F = 76.3\%$ (gray dashed line). As a starting state for the iteration process, a normalized unit matrix was chosen.
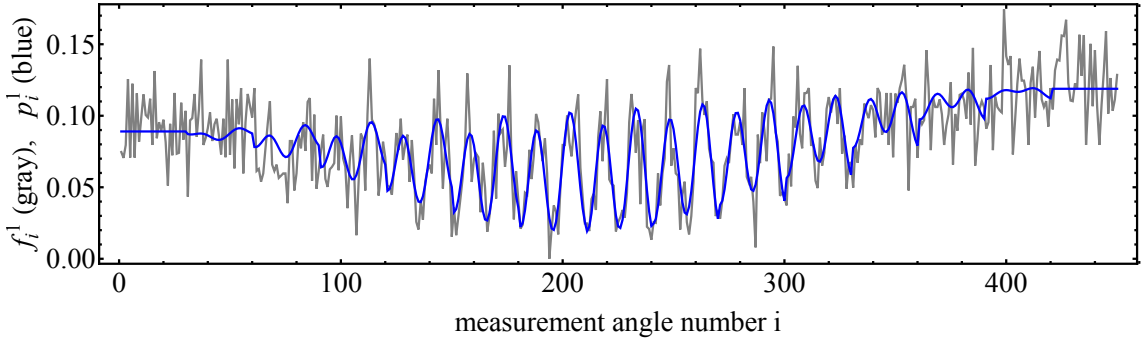

Figure 3.24.: Plot of f_i^1 and p_i^1 for $i \in \{1, \cdots, 450\}$. The gray curve shows the experimentally measured values of f_i^1, namely the value of the Husimi Q distribution at the measurement angle pair $(\theta, \phi)_i$ with the index i. The blue curve shows the values of p_i^1 resulting from the reconstructed density matrix $\rho_{\max}$.

Initially a value for θ was chosen and fixed. Then ϕ was scanned from 0 to 2π in 30 steps before θ was increased by $\pi/14$ and ϕ was scanned again. The measured values for f_i^1 can be plotted together with the values for p_i^1, as shown in figure 3.24.

In a final step, the Husimi Q distribution of $\rho_{\max}$ can be reconstructed. For this, the inferred density matrix is inserted into definition 3.29. The resulting Husimi Q distribution is shown in figure 3.25.

The characteristic ring structure of the state $|\Phi^-\rangle$ is visible in the reconstructed Husimi distribution. As can be seen in figure 3.22, the $|\downarrow\downarrow\rangle$ component of the reconstructed density matrix contains more population than the $|\uparrow\uparrow\rangle$ component. This asymmetry can also be observed in the Husimi Q distribution in figure 3.25. The Q distribution assumes higher values at the south pole of the sphere compared to the north pole. A similar asymmetry was also observed in the direct measurement of the atomic populations in table 3.2. To explain this, one has to take into account the dark counts of the employed photon detectors which herald the successful execution of a carving operation. Such a dark count in the detector measuring $|D\rangle$ polarized photons after the reflection process yields a false positive
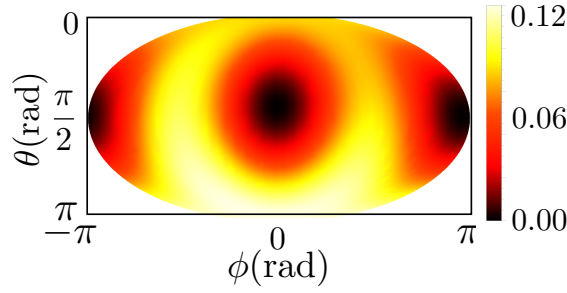
Figure 3.25.: Husimi distribution of the reconstructed density matrix $\rho_{\mathbf{max}}$. The Mollweide projection of the generalized Bloch sphere is shown with the Husimi Q function encoded color code. The distribution assumes higher values at the south pole of the generalized Bloch sphere compared to the north pole. The corresponding experimental data are shown in figure 3.21 (right plot).

event. If such an event occurs during the time interval of the first carving pulse, while the second carving pulse works properly, the resulting state is

$$\frac{\sqrt{3}}{2}\left|\downarrow\downarrow\right\rangle + \frac{1}{2\sqrt{3}}\left|\downarrow\uparrow\right\rangle + \frac{1}{2\sqrt{3}}\left|\uparrow\downarrow\right\rangle - \frac{1}{2\sqrt{3}}\left|\uparrow\uparrow\right\rangle. \tag{3.39}$$

In the reverse situation, where the first carving step works properly, but the second photon interval contains a dark count instead of a real click, the resulting state is

$$\frac{\sqrt{3}}{2}\left|\downarrow\downarrow\right\rangle - \frac{1}{2\sqrt{3}}\left|\downarrow\uparrow\right\rangle - \frac{1}{2\sqrt{3}}\left|\uparrow\downarrow\right\rangle - \frac{1}{2\sqrt{3}}\left|\uparrow\uparrow\right\rangle. \tag{3.40}$$

If both photon intervals contain a false positive click the resulting state is $\left|\downarrow\downarrow\right\rangle$ since in this case the initial state $\left|\downarrow\downarrow\right\rangle$ is effectively rotated by 2π. Thus, all experimental outcomes with any form of a false positive event lead to a state where the $\left|\downarrow\downarrow\right\rangle$ component contains the majority of the population compared to all other state contributions. This explains the asymmetry in the populations of the observed data. It is worthwhile to note that this is not the case for the generation process of the $\left|\Psi^+\right\rangle$ state. Here, the two outcomes where a false positive event occurs in the first or second photon interval lead to states where in one situation the $\left|\downarrow\downarrow\right\rangle$ component and in the other situation the $\left|\uparrow\uparrow\right\rangle$ component dominate and thus the net effect is cancelled.

3.10. Lifetime Measurement of the Produced Entangled States

Once an entangled state has been generated with the carving method, the corresponding lifetime can be characterized. In the context of quantum information processing, states situated in decoherence free subspaces are of particular interest because they are protected against environmental noise sources [153]. Due to the phase noise acting on an atomic qubit in the cavity a random phase shift $\langle\phi\rangle$ is imprinted on the two components $\left|\uparrow\right\rangle$ and $\left|\downarrow\right\rangle$. An example of a source for such phase noise could be a fluctuating magnetic field $\vec{B}(t)$ that affects the two qubits in the same way. Such a field imprints a dynamical phase onto

the two qubit states. Starting with a general quantum state $|\psi\rangle$, the dynamical phase after the vector $\vec{B}$ fluctuated for a time interval of length T can be expressed as

$$|\psi\rangle \longrightarrow e^{-\frac{i}{\hbar} \int_0^T E_{|\psi\rangle}(\vec{B}(t))dt} |\psi\rangle \tag{3.41}$$

with the dynamical phase $e^{-\frac{i}{\hbar} \int_0^T E_{|\psi\rangle}(\vec{B}(t))dt} := e^{i\langle\phi_\psi\rangle}$. After such a phase noise has been applied to an equal superposition state, it evolves as

$$\frac{1}{\sqrt{2}} \Big(|\uparrow\rangle + |\downarrow\rangle \Big) \rightarrow \frac{1}{\sqrt{2}} \Big(e^{i\langle\phi_\uparrow\rangle} |\uparrow\rangle + e^{i\langle\phi_\downarrow\rangle} |\downarrow\rangle \Big) \tag{3.42}$$

$$= e^{i\langle\phi_\uparrow\rangle} \Big(|\uparrow\rangle + e^{i(\langle\phi_\downarrow\rangle - \langle\phi_\uparrow\rangle)} |\downarrow\rangle \Big). \tag{3.43}$$

A global phase $e^{i\langle\phi_\uparrow\rangle}$ is not relevant, but uncorrelated phase noise between the $|\uparrow\rangle$ and $|\downarrow\rangle$ components leads to a reduction of the coherence terms in the corresponding density matrix. The situation is different if one considers an entangled state. Good examples are the states $|\Psi^\pm\rangle = \frac{1}{\sqrt{2}}(|\uparrow\downarrow\rangle \pm |\downarrow\uparrow\rangle)$. Under global phase noise fluctuations on both involved qubits, these states evolve into

$$|\Psi^\pm\rangle = \frac{1}{\sqrt{2}} \Big(|\uparrow\downarrow\rangle \pm |\downarrow\uparrow\rangle \Big) \tag{3.44}$$

$$\rightarrow \frac{1}{\sqrt{2}} \Big(e^{i\langle\phi_\uparrow\rangle} |\uparrow\rangle \, e^{i\langle\phi_\downarrow\rangle} |\downarrow\rangle \pm e^{i\langle\phi_\downarrow\rangle} |\downarrow\rangle \, e^{i\langle\phi_\uparrow\rangle} |\uparrow\rangle \Big) \tag{3.45}$$

$$= \frac{e^{i(\langle\phi_\uparrow\rangle + \langle\phi_\downarrow\rangle)}}{\sqrt{2}} \Big(|\uparrow\downarrow\rangle \pm |\downarrow\uparrow\rangle \Big) \tag{3.46}$$

$$= e^{i(\langle\phi_\uparrow\rangle + \langle\phi_\downarrow\rangle)} |\Psi^\pm\rangle. \tag{3.47}$$

Therefore, the states $|\Psi^\pm\rangle$ are preserved up to a global phase which makes them robust to global phase noise. It should be noted that the same reasoning does not hold for the states $|\Phi^\pm\rangle$. These states evolve according to

$$|\Phi^\pm\rangle = \frac{1}{\sqrt{2}} \Big(|\uparrow\uparrow\rangle \pm |\downarrow\downarrow\rangle \Big) \tag{3.48}$$

$$\rightarrow \frac{1}{\sqrt{2}} \Big(e^{i\langle\phi_\uparrow\rangle} |\uparrow\rangle \, e^{i\langle\phi_\uparrow\rangle} |\uparrow\rangle \pm e^{i\langle\phi_\downarrow\rangle} |\downarrow\rangle \, e^{i\langle\phi_\downarrow\rangle} |\downarrow\rangle \Big) \tag{3.49}$$

$$= \frac{e^{2i\langle\phi_\uparrow\rangle}}{\sqrt{2}} \Big(|\uparrow\uparrow\rangle \pm e^{2i(\langle\phi_\downarrow\rangle - \langle\phi_\uparrow\rangle)} |\downarrow\downarrow\rangle \Big). \tag{3.50}$$

Thus, both $|\Phi^+\rangle$ and $|\Phi^-\rangle$ are prone to global phase noise. Assuming global magnetic field fluctuations, a measurement of the state lifetime should show a longer lifetime of the $|\Psi^\pm\rangle$ states compared to the $|\Phi^\pm\rangle$ states. Such a lifetime measurement was performed experimentally. Initially a certain entangled state was generated with the double carving method. After a waiting time t, the usual parity oscillation measurement is performed to extract the fidelity as a function of t. A measure of the lifetime τ is the $1/e$ decay time of a fitted Gaussian to the measured fidelities as a function of the waiting time t. The results of this measurement are $\tau(|\Psi^-\rangle) = (204 \pm 26)\,\mu\text{s}$, $\tau(|\Psi^+\rangle) = (134 \pm 17)\,\mu\text{s}$ and $\tau(|\Phi^-\rangle) = (90 \pm 19)\,\mu\text{s}$. The $|\Psi^\pm\rangle$ indeed have a longer lifetime than the $\tau(|\Phi^-\rangle)$ state

as one would expect from the calculation above. The lifetime of $|\Phi^+\rangle$ was not measured experimentally.

The lifetimes of the produced states are limited by fluctuations of external magnetic fields and by atomic motion in the trapping potential with circular polarization components. These circular components of the trapping lasers introduce differential energy shifts between the qubit levels and thus lead to a reduction of the qubit coherence time. If the two atoms move in the trapping potential in an uncorrelated way, this effect leads to a reduction of the lifetime of the produced entangled states. The circular polarization components of the trapping lasers were carefully eliminated with appropriate polarizers and waveplates [94]. With additional ground state cooling of the atoms the effect of any residual circular trap component could be further reduced. An elimination of external fluctuating magnetic fields in combination with ground state cooling of the atoms would therefore increase the lifetime of produced entangled states.

3.11. Quantum State Carving as a Probabilistic Entanglement Swapping Procedure

In a quantum repeater architecture like the one envisioned in [74], a central ingredient is the ability to generate remote entanglement over large distances. However, the direct transmission of optical signals and therefore the direct distribution of entanglement is hampered by losses in the optical fibers connecting the network nodes. Here it is demonstrated theoretically that employing the quantum state carving method in a repeater station, the generation of remote entanglement can be achieved probabilistically.

To generate entanglement between two atoms in two remote cavities (atoms number 1 and 4), the repeater station is placed half way between the two remote cavities. The repeater station comprises two atoms (atoms number 2 and 3) like in the quantum state carving experiments. In an initial step, entanglement between the atoms 1 and 2 can be generated by performing an optical Bell state measurement between two photons extracted from those atoms [74]. Likewise, entanglement between atoms number 3 and 4 can be generated. For the specific example of a $|\Phi^+\rangle$ state generated between atoms 1 and 2 and atoms 3 and 4, the initial state of the four considered qubits can be written as

$$
\begin{aligned}
&\frac{1}{2}\Big(|{\uparrow_1}{\uparrow_2}\rangle + |{\downarrow_1}{\downarrow_2}\rangle\Big)\Big(|{\uparrow_3}{\uparrow_4}\rangle + |{\downarrow_3}{\downarrow_4}\rangle\Big) \qquad\qquad (3.51)\\
&= \frac{1}{2}\Big(|{\uparrow_1}{\uparrow_2}{\uparrow_3}{\uparrow_4}\rangle + |{\uparrow_1}{\uparrow_2}{\downarrow_3}{\downarrow_4}\rangle + |{\downarrow_1}{\downarrow_2}{\uparrow_3}{\uparrow_4}\rangle + |{\downarrow_1}{\downarrow_2}{\downarrow_3}{\downarrow_4}\rangle\Big).
\end{aligned}
$$

At this stage in the protocol the double carving scheme between atoms 2 and 3 in the repeater station can be executed by successively reflecting two linearly polarized coherent

optical states. The input and output states for a successful double carving protocol including the last $\pi/2$ rotation as in figure 3.15 can be written as

$$|\uparrow\uparrow\rangle \longrightarrow \frac{1}{\sqrt{2}}(|\uparrow\uparrow\rangle - |\downarrow\downarrow\rangle) \tag{3.52}$$

$$|\uparrow\downarrow\rangle \longrightarrow \frac{1}{\sqrt{2}}(|\uparrow\downarrow\rangle - |\downarrow\uparrow\rangle) \tag{3.53}$$

$$|\downarrow\uparrow\rangle \longrightarrow \frac{1}{\sqrt{2}}(-|\uparrow\downarrow\rangle + |\downarrow\uparrow\rangle) \tag{3.54}$$

$$|\downarrow\downarrow\rangle \longrightarrow \frac{1}{\sqrt{2}}(-|\uparrow\uparrow\rangle + |\downarrow\downarrow\rangle). \tag{3.55}$$

Applying the carving operation on atoms 2 and 3 to the initial state 3.51, the output state can be written as

$$\frac{1}{2\sqrt{2}}\Big[|\uparrow_1\rangle\Big(|\uparrow_2\uparrow_3\rangle - |\downarrow_2\downarrow_3\rangle\Big)|\uparrow_4\rangle + |\uparrow_1\rangle\Big(|\uparrow_2\downarrow_3\rangle - |\downarrow_2\uparrow_3\rangle\Big)|\downarrow_4\rangle + \tag{3.56}$$

$$|\downarrow_1\rangle\Big(-|\uparrow_2\downarrow_3\rangle + |\downarrow_2\uparrow_3\rangle\Big)|\uparrow_4\rangle + |\downarrow_1\rangle\Big(-|\uparrow_2\uparrow_3\rangle + |\downarrow_2\downarrow_3\rangle\Big)|\downarrow_4\rangle\Big]$$

$$= \frac{1}{2\sqrt{2}}\Big[|\uparrow_1\uparrow_2\uparrow_3\uparrow_4\rangle - |\uparrow_1\downarrow_2\downarrow_3\uparrow_4\rangle + |\uparrow_1\uparrow_2\downarrow_3\downarrow_4\rangle - |\uparrow_1\downarrow_2\uparrow_3\downarrow_4\rangle$$

$$- |\downarrow_1\uparrow_2\downarrow_3\uparrow_4\rangle + |\downarrow_1\downarrow_2\uparrow_3\uparrow_4\rangle - |\downarrow_1\uparrow_2\uparrow_3\downarrow_4\rangle + |\downarrow_1\downarrow_2\downarrow_3\downarrow_4\rangle\Big]$$

$$= \frac{1}{2\sqrt{2}}\Big[|\downarrow_2\downarrow_3\rangle\Big(-|\uparrow_1\uparrow_4\rangle + |\downarrow_1\downarrow_4\rangle\Big) + |\downarrow_2\uparrow_3\rangle\Big(|\downarrow_1\uparrow_4\rangle - |\uparrow_1\downarrow_4\rangle\Big) +$$

$$|\uparrow_2\downarrow_3\rangle\Big(|\uparrow_1\downarrow_4\rangle - |\downarrow_1\uparrow_4\rangle\Big) + |\uparrow_2\uparrow_3\rangle\Big(|\uparrow_1\uparrow_4\rangle - |\downarrow_1\downarrow_4\rangle\Big)\Big].$$

After this step, another linearly polarized coherent state is reflected from the cavity. In the case where the polarization of this photon does not change, the state of the atoms in the repeater station is projected onto $|\downarrow_2\downarrow_3\rangle$, while the atoms in the remote cavities will be projected onto $\frac{1}{\sqrt{2}}(-|\uparrow_1\uparrow_4\rangle + |\downarrow_1\downarrow_4\rangle)$, a maximally entangled state. Therefore, three coherent states are required to perform the entanglement swapping. The first two are needed for the carving procedure. A polarization change after the reflection of both of these pulses heralds the successful carving operation. The third reflection of a coherent state projects the outer atoms 1 and 4 on a maximally entangled state if its polarization is not changed after the reflection.

The described mechanism to perform entanglement swapping is probabilistic and heralded. The first carving step has an efficiency of 3/4 while the second has an efficiency of 2/3 which yields a combined success probability of 1/2. The third step has a success probability of 1/4. Therefore, the total combined success probability of the protocol is 1/8.

Experimental imperfections like the finite cooperativity of the atom-cavity system further reduce these numbers. For example, in the double carving experiment an efficiency of 61% was measured instead of the expected 75% for the first carving step. Also, employing weak coherent pulses strongly reduces the total efficiency since in the majority of experimental trials no photon is present in the carving pulses and no herald photon can be detected. Nevertheless, the scheme could be employed to generate remote entanglement in a probabilistic way.

In the case in which the polarization of the last reflected photon did change, a π pulse can be applied to atoms 2 and 3 before reflecting another linearly polarized photon. If the polarization of this additional photon does not change, the state $\frac{1}{\sqrt{2}}(|\uparrow_1\uparrow_4\rangle - |\downarrow_1\downarrow_4\rangle)$ results which is also a maximally entangled state between the remote atoms 1 and 4. In the other case, the state $\frac{1}{\sqrt{2}}(|\uparrow_1\downarrow_4\rangle - |\downarrow_1\uparrow_4\rangle)$ or $\frac{1}{\sqrt{2}}(-|\uparrow_1\downarrow_4\rangle + |\downarrow_1\uparrow_4\rangle)$ results.

To circumvent the probabilistic nature of this scheme and increase the efficiency, a deterministic gate operation between atoms 2 and 3 can be implemented. The experimental implementation of such a gate will be discussed in section 4.

3.12. Requirements for the Carving Scheme

It is important to ask the question for the required ranges of the atom-cavity parameters to successfully perform the carving operation for entanglement generation. As it turns out, these requirements allow for employing a cavity with a lower cooperativity than in our case. The scheme presented in this thesis differs in some aspects from the original proposal of Sørensen and Mølmer [80]. In this proposal, the reflection of a photon from a symmetric ring cavity was used as a herald for the presence of atoms interacting with the cavity mode. Thus, it is not a polarization rotation that heralds the presence of coupling atoms inside the cavity, but the fact that the photons are reflected at all. Since the cavity in the QGate laboratory is strongly asymmetric, the implementation of this scheme was not feasible. Thus, an extension of the original proposal to general cavity parameters was devised.

As outlined in section 3.1, the method of choice is to consider two different polarization modes $|R\rangle$ and $|L\rangle$. If a photon in a superposition of these two modes is impinging onto the cavity, the presence of coupling atoms can be heralded via a polarization rotation after the reflection. Experimentally, the $|L\rangle$ mode is far off-resonant from the atomic transition and can serve as a reference. The $|R\rangle$ mode can be prohibited from entering the cavity by an atom in the state $|\uparrow\rangle$. The cavity parameters are given by $(g,\kappa,\kappa_r,\gamma) = 2\pi(7.8, 2.5, 2.3, 3.0)$ MHz. Input-output theory allows to calculate the reflection amplitude r of the cavity which depends on the number of coupling atoms N. For sufficiently narrow photons in the frequency domain (compared to the cavity linewidth), the reflection amplitude on resonance can be expressed as [112, 113]

$$r(N) = 1 - \frac{\kappa_r/\kappa}{C(N) + 1/2} \tag{3.57}$$

where $C(N) = Ng^2/(2\kappa\gamma) = 4.1 \times N$ is the cooperativity of the system. Since $|L\rangle$ is far off resonant, a photon in this polarization mode experiences a reflection amplitude of $r(0)$ while a photon in the $|R\rangle$ mode experiences $r(N)$. Since the carving scheme relies on the polarization rotation of light after the reflection, the probability P_f to change the polarization from linear to its orthogonal state is an important quantity. We can calculate P_f by defining a reflection operator $\hat{R}$ according to

$$\hat{R} := |R\rangle\langle R|\, r(N) + |L\rangle\langle L|\, r(0). \tag{3.58}$$

With this definition P_f can be expressed as a matrix element of the reflection operator $\hat{R}$ according to

$$P_f(N) = \left| \langle D| \hat{R} |A\rangle \right|^2 \tag{3.59}$$

$$= \left| \frac{1}{2}r(N=0) - \frac{1}{2}r(N>0) \right|^2 = \tag{3.60}$$

$$= \left(\frac{\kappa_r}{\kappa} \frac{Ng^2}{Ng^2 + \gamma\kappa} \right)^2 = \left(\eta_{\text{esc}} \frac{C(N)}{C(N) + 1/2} \right)^2, \tag{3.61}$$

where $\eta_{\text{esc}} = \kappa_r/\kappa = 0.92$ is the probability of a photon in the cavity to escape through the outcoupling mirror. In absence of coupling atoms ($N = 0$), one obtains $P_f = 0$ as expected. For $N = 0,1,2$, one obtains $P_f(N = 0,1,2) = (0.00, 0.67, 0.75)$. The input pulse reflected from the cavity is a coherent pulse with an average photon number of $\bar{n}$ and thus the average number of heralding photons with a polarization state $|D\rangle$ is given by $\bar{n}P_f$. In principle, this means that one can perform these experiments with big values of $\bar{n}$, but there is always a finite fraction of scattered photons. This fraction s is given by [80]

$$s = \frac{4\kappa_r\gamma Ng^2}{(\kappa\gamma + Ng^2)^2}. \tag{3.62}$$

For the experimental parameters in this thesis the scattering fraction s amounts to $s(N = 0,1,2) = (0.00, 0.36, 0.20)$. Therefore, two effects are competing. On the one hand, there is the undesired scattering of photons from the atoms in the cavity which increases with $\bar{n}$. On the other hand, the heralding signal for the entanglement generation also increases with increasing $\bar{n}$. From these considerations it follows that the ratio P_f/s should be as large as possible to achieve a high heralding signal and a low scattering fraction. An evaluation of this expression yields

$$P_f/s = \frac{Ng^2\kappa_r}{4\kappa^2\gamma} = \frac{\eta_{\text{esc}}}{2}C. \tag{3.63}$$

Therefore, the coorporativity C is a crucial parameter quantifying the performance of the carving protocol. Additionally, the escape probability $\eta_{\text{esc}} = \kappa_r/\kappa$ determines the performance and assumes its highest possible value of unity for $\kappa_r = \kappa$.

A different way to approach the question of the performance of the carving scheme is to look at the phase shift mechanism accompanying the reflection process from the cavity. A prerequisite for the phase shift to work properly is a change of sign of the reflection amplitude r for right-circularly polarized light in the case of coupling atoms in the cavity compared to the empty cavity. The phase of the reflected light is given by $\arg(r)$, the angle of r with the real positive axis. The analytic expression for r on resonance was given in equation 3.57. Since $r(N>0) > r(N=0)$, the only possibility to achieve the desired phase shift is to change the sign of r when changing from $N=0$ to $N>0$. This means that the two conditions

$$r(N>0) = 1 - \frac{2\kappa_r\gamma}{Ng^2 + \kappa\gamma} = 1 - \frac{\kappa_r/\kappa}{C + 1/2} > 0 \tag{3.64}$$

$$r(N=0) = 1 - \frac{2\kappa_r}{\kappa} < 0 \tag{3.65}$$

must be fulfilled. These inequalities can be rearranged to

$$C = \frac{Ng^2}{2\kappa\gamma} > \eta_{\text{esc}} - 1/2 \qquad (3.66)$$

$$\kappa_r > \kappa/2. \qquad (3.67)$$

Therefore, a cooperativity C higher than $\eta_{\text{esc}} - 1/2 = 0.42$ and an asymmetric cavity are needed for a proper execution of the phase shift mechanism. In this regime a sign change of r between the coupling and the non-coupling cases occurs. When decreasing the cooperativity, the success probability of the scheme is reduced according to equation 3.61. However, the herald signal allows to postselect on the cases where the carving process was successful. For our case, the threshold for the cooperativity is a factor of ten lower than the actual experimental value $C = 4.1$. This means that g could in principle be much lower than it actually is in the experiment.

4. Photon-Mediated Atom-Atom Gate

The content of this chapter has been published in:

Photon-Mediated Quantum Gate between Two Neutral Atoms in an Optical Cavity.

S. Welte, B. Hacker, S. Daiss, S. Ritter and G. Rempe,

In chapter 3, a method was developed to generate entanglement between two atoms in a probabilistic and heralded protocol. The purpose of the experiment described in this chapter is to implement a universal quantum gate between the two atomic qubits [43]. The two theoretical proposals for this experiment date back to 2005 and 2006 [75, 76] and were implemented experimentally in this work. An intracavity quantum gate allows for the generation of entanglement in a deterministic way and has many applications in a future quantum network. On the one hand, it allows for local processing of quantum information in the network nodes. This sets the stage for a quantum network architecture where small scale quantum computers located in the network nodes perform elementary quantum computation tasks. The results of these computations could later be mapped onto flying photons via the scheme outlined in [46] and sent to a different network node [154]. Furthermore, the demonstrated gate can be used in an entanglement swapping protocol to distribute entanglement in a large scale quantum network. In such a scheme, the two atoms in the same cavity play the role of a repeater station. The theoretical proposal for such an atom-cavity based quantum repeater architecture was outlined in [74]. While the technique of quantum state carving does not necessarily require single photons for entanglement generation, the gate described in this chapter is based on a protocol that deterministically generates entanglement if a single-photon source is employed. The reflection of the single photon from the cavity executes the gate. As a single-photon source was not available for the described experiments, they were performed with strongly attenuated coherent laser pulses. A postselection on the presence of a single photon in these pulses with conventional photon detectors mimics a single-photon source.

The described gate mechanism is independent of the experimental platform. Therefore it can be realized in any physical implementation where two material qubits can be coupled to a resonator [155–162]. Possible platforms include superconducting qubits, trapped ions, nitrogen-vacancy centers and quantum dots.

4.1. Operating Principle of the Gate

Just as the carving technique, the atom-atom gate relies on the reflection of light from the atom-atom-cavity system. The situation is illustrated in figure 4.1. In contrast to the
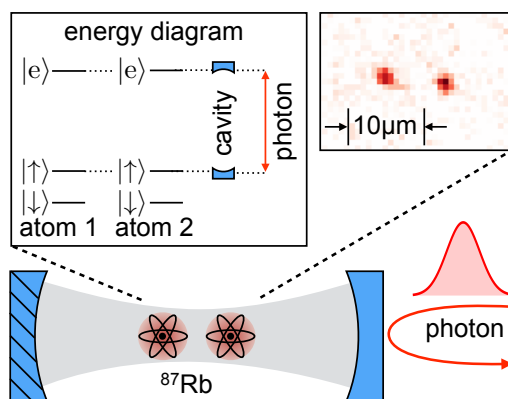
Figure 4.1.: Atom-atom gate executed via reflection of a photon from the cavity. A right-circularly polarized photon is reflected from the cavity containing the two atomic qubits to execute a quantum logic gate between them. The upper left inset shows a simplified level scheme of the two atoms which can be considered as three-level systems. The upper right inset shows an EMCCD camera flourescence image of an intracavity atom pair. The cavity is actively stabilized to the $|\uparrow\rangle \to |e\rangle$ transition. Reflected photons are resonant with the uncoupled cavity.

quantum state carving experiment (see chapter 3), where linearly polarized light ($|A\rangle$) was employed, the polarization of the light impinging onto the cavity is right-circular ($|R\rangle$) for the atom-atom gate experiment. Due to the phase shift mechanism outlined in section 2.5, the reflection of a sinlge photon with this polarization gives rise to a truth table of the form

$$
\begin{aligned}
|\uparrow\uparrow\rangle |R\rangle &\longrightarrow & |\uparrow\uparrow\rangle |R\rangle \\
|\uparrow\downarrow\rangle |R\rangle &\longrightarrow & |\uparrow\downarrow\rangle |R\rangle \\
|\downarrow\uparrow\rangle |R\rangle &\longrightarrow & |\downarrow\uparrow\rangle |R\rangle \\
|\downarrow\downarrow\rangle |R\rangle &\longrightarrow & - |\downarrow\downarrow\rangle |R\rangle \, .
\end{aligned}
\tag{4.1}
$$

This truth table represents a controlled phase gate and therefore a universal quantum gate between the two atomic qubits [135]. Figure 4.2 illustrates the phase shift mechanism for different configurations of atomic states in the cavity. The photon serves as an ancilla to mediate the atom-atom interaction and executes the gate upon reflection from the cavity. It is important to note that the minus sign in front of the $|\downarrow\downarrow\rangle$ component only occurs for an odd number of reflected photons. If a Fock state $|n\rangle$ is reflected, a phase shift of $n \cdot \pi$ results.

For a different set of input basis states, the gate can assume the form of a controlled NOT (CNOT) gate. An example is the basis $|\uparrow\rangle |\rightarrow\rangle$, $|\uparrow\rangle |\leftarrow\rangle$, $|\downarrow\rangle |\rightarrow\rangle$, $|\downarrow\rangle |\leftarrow\rangle$, with $|\rightarrow\rangle := 1/\sqrt{2}(|\uparrow\rangle + |\downarrow\rangle)$ and $|\leftarrow\rangle := 1/\sqrt{2}(|\uparrow\rangle - |\downarrow\rangle)$. In this particular basis, the gate transforms the four basis states according to the truth table

$$
\begin{aligned}
|\uparrow\rangle |\rightarrow\rangle &\longrightarrow |\uparrow\rangle |\rightarrow\rangle \\
|\uparrow\rangle |\leftarrow\rangle &\longrightarrow |\uparrow\rangle |\leftarrow\rangle \\
|\downarrow\rangle |\rightarrow\rangle &\longrightarrow |\downarrow\rangle |\leftarrow\rangle \\
|\downarrow\rangle |\leftarrow\rangle &\longrightarrow |\downarrow\rangle |\rightarrow\rangle \, .
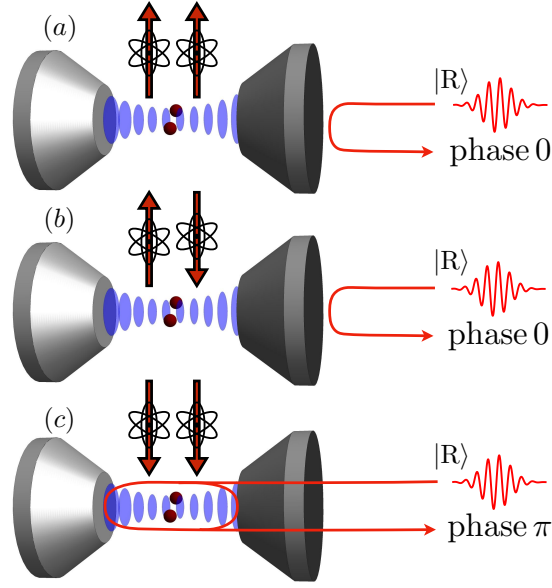\end{aligned}
\tag{4.2}
$$

Figure 4.2.: Illustration of the reflection process. The figure illustrates the reflection mechanism for $|R\rangle$-polarized input photons. If both atoms (a) or only one atom (b) occupies the state $|\uparrow\rangle$, the photon is directly reflected from the first cavity mirror. If both atoms occupy the non-coupling state $|\downarrow\rangle$, the photons enter the cavity, bounce back and forth and leave through the outcoupling mirror (c). In comparison to the cases (a) and (b), a phase shift of π is imprinted onto the combined atom-atom-photon state.

For characterization purposes, a quantum gate can be probed in any desired basis. As was discussed in chapter 3, all four maximally entangled Bell states can be generated with the method of quantum state carving. These Bell states also constitute a set of basis states for the two-qubit Hilbert space. This set of states is especially interesting because it can be generated experimentally without the necessity of individual atom addressing. Employing truth table 4.1, the action of the atom-atom gate onto the four Bell states is given by

$$
\begin{aligned}
|\Psi^-\rangle |R\rangle &= \tfrac{1}{\sqrt{2}}\big(|\uparrow\downarrow\rangle - |\downarrow\uparrow\rangle\big)|R\rangle &\longrightarrow&\quad \tfrac{1}{\sqrt{2}}\big(|\uparrow\downarrow\rangle - |\downarrow\uparrow\rangle\big)|R\rangle = |\Psi^-\rangle |R\rangle \\
|\Psi^+\rangle |R\rangle &= \tfrac{1}{\sqrt{2}}\big(|\uparrow\downarrow\rangle + |\downarrow\uparrow\rangle\big)|R\rangle &\longrightarrow&\quad \tfrac{1}{\sqrt{2}}\big(|\uparrow\downarrow\rangle + |\downarrow\uparrow\rangle\big)|R\rangle = |\Psi^+\rangle |R\rangle \\
|\Phi^-\rangle |R\rangle &= \tfrac{1}{\sqrt{2}}\big(|\uparrow\uparrow\rangle - |\downarrow\downarrow\rangle\big)|R\rangle &\longrightarrow&\quad \tfrac{1}{\sqrt{2}}\big(|\uparrow\uparrow\rangle + |\downarrow\downarrow\rangle\big)|R\rangle = |\Phi^+\rangle |R\rangle \\
|\Phi^+\rangle |R\rangle &= \tfrac{1}{\sqrt{2}}\big(|\uparrow\uparrow\rangle + |\downarrow\downarrow\rangle\big)|R\rangle &\longrightarrow&\quad \tfrac{1}{\sqrt{2}}\big(|\uparrow\uparrow\rangle - |\downarrow\downarrow\rangle\big)|R\rangle = |\Phi^-\rangle |R\rangle .
\end{aligned}
\tag{4.3}
$$

The two Bell states $|\Phi^\pm\rangle$ are interconverted via the gate operation while the other two Bell states $|\Psi^\pm\rangle$ are invariant because they do not contain a $|\downarrow\downarrow\rangle$ component. The experimental verification of truth table 4.3 will demonstrate the gate mechanism in section 4.2.

In addition to the expected truth table, the gate must comprise the ability to generate entanglement between the two input qubits. This can be achieved by initially preparing both atoms in an equal superposition of the two qubit states

$$
\frac{1}{\sqrt{2}}(|\uparrow\rangle - |\downarrow\rangle) \otimes \frac{1}{\sqrt{2}}(|\uparrow\rangle - |\downarrow\rangle) = \frac{1}{2}(|\uparrow\uparrow\rangle - |\uparrow\downarrow\rangle - |\downarrow\uparrow\rangle + |\downarrow\downarrow\rangle).
\tag{4.4}
$$

Afterwards, a right-circularly polarized photon is reflected from the atom-atom-cavity system to generate

$$\frac{1}{2}(|\uparrow\uparrow\rangle - |\uparrow\downarrow\rangle - |\downarrow\uparrow\rangle - |\downarrow\downarrow\rangle). \tag{4.5}$$

This state already is a maximally entangled state, but it can be transformed into a Bell state via a global rotation of both qubits. The amount of entanglement in the system is invariant under such a global rotation. Application of a $\pi/4$ pulse yields

$$\left|\Phi^-\right\rangle = \frac{1}{\sqrt{2}}(|\uparrow\uparrow\rangle - |\downarrow\downarrow\rangle). \tag{4.6}$$

The generation of entanglement together with the truth table with the four Bell states as input states will serve as a characterization of the gate in section 4.4.

4.2. Experimental Implementation of the Atom-Atom Gate: Truth Table

In this section, the experimental data obtained in the atom-atom gate experiment are discussed. As a first characterization, the truth table of the gate is determined. As outlined in section 4.1, the gate is probed in the basis spanned by the four maximally entangled Bell states generated initially with the method of quantum state carving. After the input state preparation, the gate is executed before the resulting output states are analyzed via a measurement of parity oscillations. The entire protocol thus comprises five essential steps, namely state preparation, quantum state carving, gate execution, analysis and state detection. All steps are shown schematically in the circuit diagram in figure 4.3. This experimental protocol is followed by a 700 µs long cooling interval. The repetition rate of the experiment is 1 kHz and the gate execution time is defined by the bandwidth of the reflected photons. Here, they have a full width at half maximum of 0.9 µs.

After preparing the basis states, a right-circularly polarized weak coherent pulse is reflected from the atom-atom-cavity system to execute the gate. Experimentally, a pulse with an average photon number of $\bar{n} = 0.13$ was chosen. The Poissonian nature of the photon number statistics with a high vacuum contribution in the pulse makes it necessary to herald the successful gate operation with single-photon detectors monitoring the reflection mode of the cavity. These detector clicks are employed to postselect on the presence of a single photon in the reflected coherent pulse. Figure 4.4(a) shows the fidelities of the respective prepared input states. The resulting fidelities after the gate operation are shown in figure 4.4(b).

The fidelities were derived from a measurement of the parity signal before or after execution of the gate, respectively. The fidelities for the $|\Psi^\pm\rangle$ states do not significantly differ before and after the gate operation. This is expected because these states comprise no $|\downarrow\downarrow\rangle$ component and are therefore not affected. The $|\Phi^\pm\rangle$ states however change their roles after the gate has been executed.

For the extraction of the respective fidelities in figure 4.4(a) and (b), the offset $\overline{\Pi} := 2\mathrm{Re}(\rho_{\uparrow\downarrow,\downarrow\uparrow})$, the oscillation amplitude $\Delta\Pi := 2\mathrm{Re}(\rho_{\uparrow\uparrow,\downarrow\downarrow})$ and the populations $P_{\uparrow\uparrow}$, $P_{\uparrow\downarrow} + P_{\downarrow\uparrow}$, $P_{\downarrow\downarrow}$ need to be measured. The experimentally obtained values are given in table 4.1. Figure
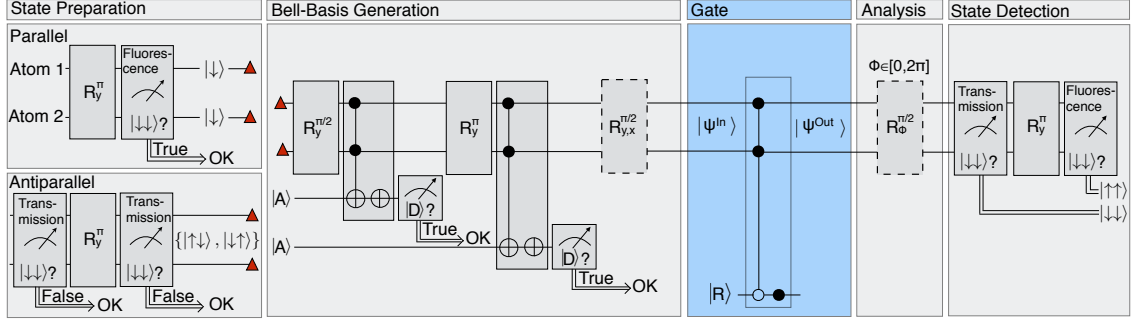
Figure 4.3.: Circuit diagram of the gate operation. The diagram shows all the steps necessary to prepare input states and to execute and characterize the atom-atom gate. Qubit rotations are labelled with R and have a subscript denoting the rotation axis x ($|\uparrow\rangle + |\downarrow\rangle$) or y ($|\uparrow\rangle + i|\downarrow\rangle$). The superscript denotes the rotation angle. A state detection of the two atomic qubits can be performed via a measurement of the transmission through the cavity or via a fluorescence measurement as discussed in section 2.4.3. State preparation is performed with the optical pumping schemes outlined in section 2.4.1 and heralded with a transmission or fluorescence measurement. Whenever the result of such a measurement does not yield the desired state (OK), the corresponding experimental run is discarded and the protocol is repeated. After the state preparation, the four Bell states are generated with the carving technique described in section 3.1 and used as input states for the atom-atom gate. In the Bell-basis generation, the symbol $\oplus$ denotes a NOT operation while the symbol $\bullet$ denotes the control qubits. The second NOT operation after the Toffoli gate (in the second and fifth box from the left in the Bell-basis generation panel) in each carving step is needed for a compact notation of the truth table in equation 3.2. The triplet states $|\Phi^{\pm}\rangle$ and $|\Psi^{+}\rangle$ can be transformed into any other triplet state via a global $\pi/2$ rotation indicated by the dashed box. This rotation is optional and can be applied depending on the desired Bell state. The singlet state $|\Psi^{-}\rangle$ is generated from an initially prepared incoherent mixture of the form $\frac{1}{2}(|\uparrow\downarrow\rangle\langle\uparrow\downarrow| + |\downarrow\uparrow\rangle\langle\downarrow\uparrow|)$. The respective created maximally entangled state is used as an input state $|\Psi^{\text{In}}\rangle$ for the atom-atom gate (blue panel). Here, the symbol $\circ$ is equivalent to a phase gate interleaved between two NOT gates. The additional phase gate $\bullet$ acting on the photon is necessary for a compact notation of the truth table in equation 4.1. After the gate was executed, the state $|\Psi^{\text{Out}}\rangle$ leaves the gate. In a final stage, the output state is rotated by $\pi/2$ via a Raman pulse of variable phase ϕ before the double state detection protocol from section 2.4.3.3 is applied. The analysis pulse is optional. If a direct measurement of the populations P_{ij} with $i,j \in \{\uparrow, \downarrow\}$ is needed, this pulse is omitted. For a measurement of $\widetilde{P}_{ij}$, the analysis pulse is applied to the atoms. From both P_{ij} and $\widetilde{P}_{ij}$, the fidelity of the output states with maximally entangled states can be inferred.

4.5 shows the parity signal of all four Bell states before (left column) and after (right column) execution of the gate. The parity signals in this figure represent the raw data necessary to calculate the fidelities shown in figure 4.4(a) and (b).
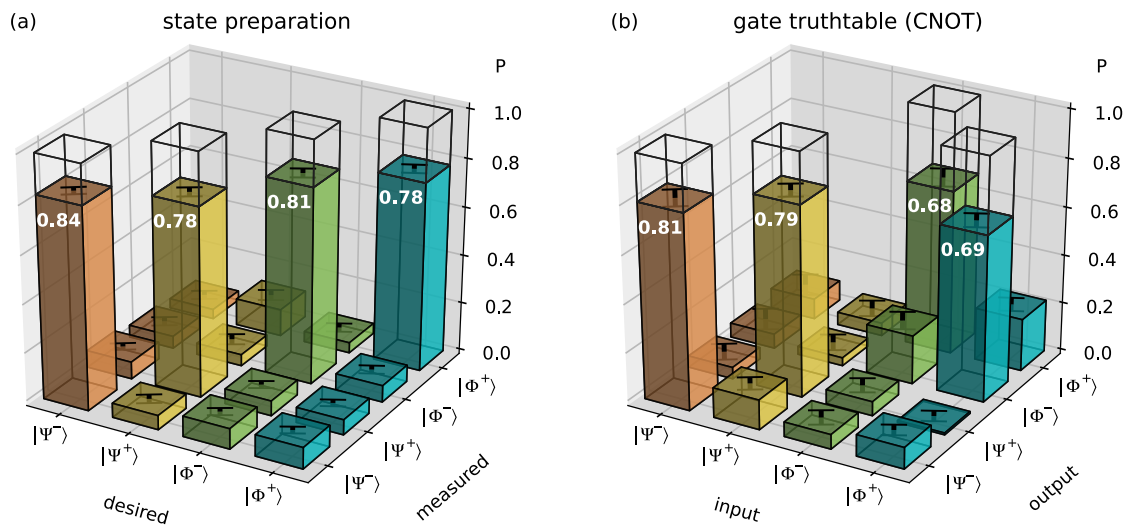
Figure 4.4.: Input and output states of the atom-atom gate.
(a) Input states generated via quantum state carving. All four Bell states are generated with an average fidelity of $(80.2 \pm 0.8)\%$. The open bars show a fidelity of unity for an ideal preparation of the four Bell states. The sum of the probabilities P in every row is unity.
(b) Output states after the gate was performed. An average overlap of $(74.1 \pm 1.6)\%$ with the ideal CNOT truth table (open bars) is achieved. The gate changes the roles of the $|\Phi^{\pm}\rangle$ states and leaves the $|\Psi^{\pm}\rangle$ states unaffected.
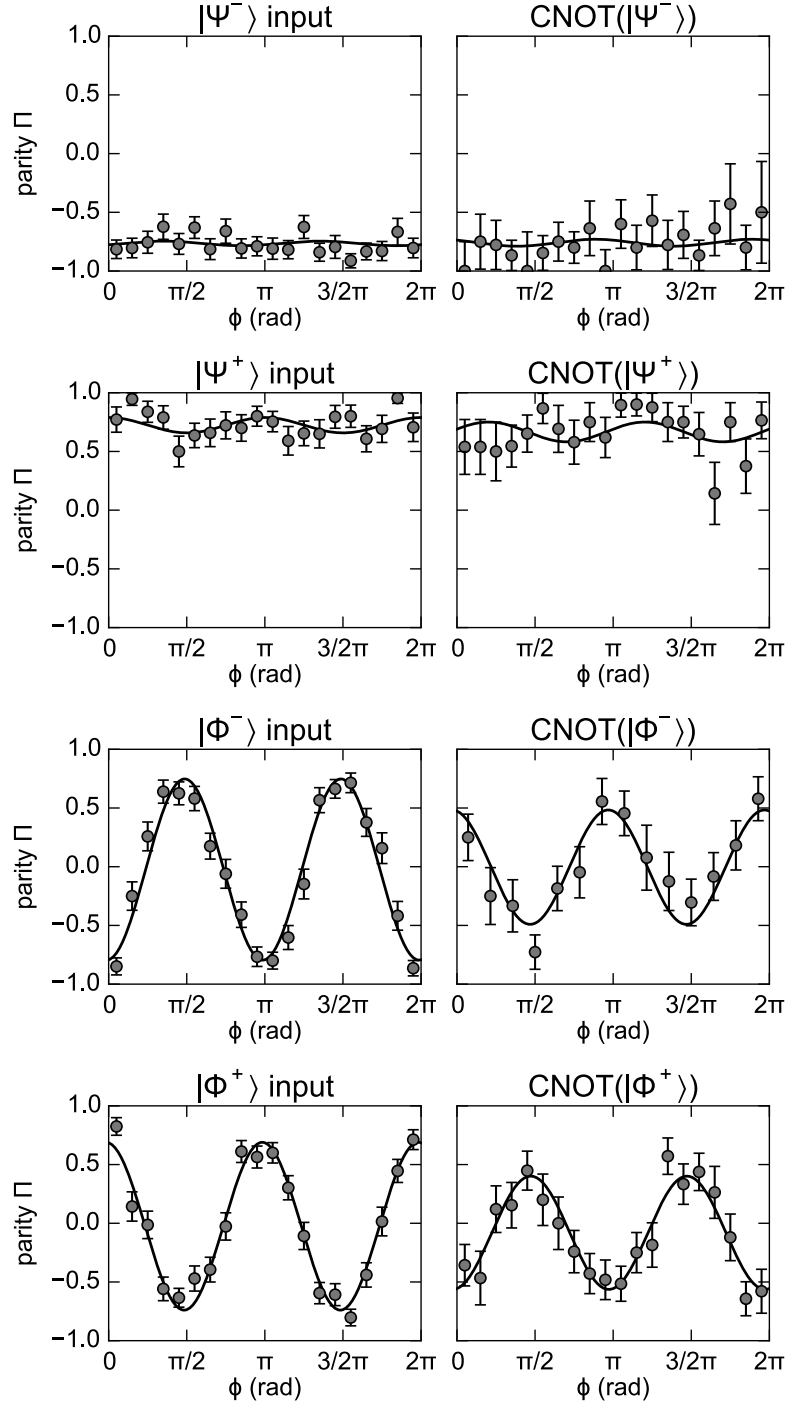
Figure 4.5.: Parity signals before and after the gate execution. The left column shows the parity signals of the four Bell states as they are generated with the quantum state carving technique. While $|\Psi^{\pm}\rangle$ show a constant parity, the parity of $|\Phi^{\pm}\rangle$ shows an oscillatory behavior when ϕ is changed between 0 and 2π. The right column shows the respective parity signals after execution of the atom-atom gate. While the signals of $|\Psi^{\pm}\rangle$ do not change, the signals corresponding to $|\Phi^{\pm}\rangle$ change their roles as described by equation 4.3. This change of roles is observable via a phase flip of the corresponding parity signal. The solid lines represent a fitted sinusoidal curve with the amplitude, phase and offset as free fit parameters. The extraction of these parameters is necessary for the calculation of the respective fidelities.

Table 4.1.: Population measurements and inferred fidelities. The population measurements before and after execution of the gate are listed. The obtained values for the amplitude of the oscillation $\Delta\Pi$ and the offset $\overline{\Pi}$ are inferred from a fit to the data shown in figure 4.5. From these numbers, the values for the fidelity F can be calculated according to equation 4.8.

state	$P_{\uparrow\uparrow}$	$P_{\uparrow\downarrow}+P_{\downarrow\uparrow}$	$P_{\downarrow\downarrow}$	$\overline{\Pi}$	$\Delta\Pi$	F
$|\Psi^-\rangle$	03%	91%	06%	-0.76	-0.01	84(1)%
CNOT($|\Psi^-\rangle$)	05%	86%	10%	-0.76	$+0.02$	81(3)%
$|\Psi^+\rangle$	07%	84%	09%	$+0.72$	$+0.06$	78(2)%
CNOT($|\Psi^+\rangle$)	03%	91%	06%	$+0.67$	$+0.02$	79(3)%
$|\Phi^-\rangle$	29%	15%	56%	-0.02	-0.77	81(2)%
CNOT($|\Phi^-\rangle$)	23%	12%	65%	$+0.00$	$+0.48$	68(4)%
$|\Phi^+\rangle$	45%	15%	40%	-0.03	$+0.71$	78(2)%
CNOT($|\Phi^+\rangle$)	44%	10%	46%	-0.08	-0.47	69(3)%

The measurements of the parity in figure 4.5 show the key features of the photon reflection mechanism. The direct comparison of these states before and after execution of the gate shows that the two $|\Psi^\pm\rangle$ states are unaffected. The $|\Phi^\pm\rangle$ states however change their roles after the photon reflection as can be observed via the phase change of the corresponding parity signal. For an evaluation of the fidelity with the ideal Bell states, the populations are needed as well. These can be inferred experimentally by omitting the analysis pulse in figure 4.3 and direct application of the double state detection protocol as outlined in section 2.4.3.3. The parity signal as a function of ϕ can be written as

$$\Pi(\phi) = 2\mathrm{Re}(\rho_{\uparrow\downarrow,\downarrow\uparrow}) + 2\mathrm{Re}(\rho_{\uparrow\uparrow,\downarrow\downarrow})\cos(2\phi) + 2\mathrm{Im}(\rho_{\uparrow\uparrow,\downarrow\downarrow})\sin(2\phi). \quad (4.7)$$

The amplitude $\Delta\Pi = 2\mathrm{Re}(\rho_{\uparrow\uparrow,\downarrow\downarrow})$ and the offset $\overline{\Pi} = 2\mathrm{Re}(\rho_{\uparrow\downarrow,\downarrow\uparrow})$ can be directly inferred from a least square fit to the data in figure 4.5. In a final step, the fidelity can be calculated according to

$$
\begin{aligned}
F(|\Psi^-\rangle) &= \tfrac{1}{2}(P_{\uparrow\downarrow} + P_{\downarrow\uparrow}) - \mathrm{Re}(\rho_{\uparrow\downarrow,\downarrow\uparrow}) \\
F(|\Psi^+\rangle) &= \tfrac{1}{2}(P_{\uparrow\downarrow} + P_{\downarrow\uparrow}) + \mathrm{Re}(\rho_{\uparrow\downarrow,\downarrow\uparrow}) \\
F(|\Phi^-\rangle) &= \tfrac{1}{2}(P_{\uparrow\uparrow} + P_{\downarrow\downarrow}) - \mathrm{Re}(\rho_{\uparrow\uparrow,\downarrow\downarrow}) \\
F(|\Phi^+\rangle) &= \tfrac{1}{2}(P_{\uparrow\uparrow} + P_{\downarrow\downarrow}) + \mathrm{Re}(\rho_{\uparrow\uparrow,\downarrow\downarrow}).
\end{aligned}
\quad (4.8)
$$

Using the measured values from the first five columns in table 4.1, the sixth column with the numbers for the respective fidelities is calculated. The measured fidelities are limited by the imperfect preparation of the Bell states with the carving technique. An improvement of this preparation fidelity could be achieved by utilizing a single-photon source for the carving process. Employing the clicks in the single-photon detector as a herald for the successful reflection of the single photon would further increase the fidelity of the generated input states. If the herald is measured successfully in such a detector, the cases where photons are scattered by the atom pair can be excluded. Furthermore, heralding detectors with a low dark count rate are beneficial for a high preparation fidelity with the carving technique as was outlined in section 3.5.

4.3. Atom-Atom Gate Efficiency

The efficiency of the gate is 4.2% and given by the fraction of experimental runs in which one photon click was detected in the time interval of the gate-executing optical pulse. The main limiting factors for the gate efficiency are the high probability to observe zero photons due to the Poissonian photon number statistics in the reflected pulse, the non-unity reflectivity of the cavity on resonance, and the quantum efficiency of the employed single-photon detectors. The reflectivity of the atom-atom-cavity system on resonance is 67% in the case where the atoms occupy the state $|\downarrow\downarrow\rangle$. This value is only slightly changed when transferring an atom into the state $|\uparrow\rangle$. The backreflected photons are detected with a quantum efficiency of 55%. There is a small probability to transfer an atom out of the qubit space with the photon that executes the gate. In this case, the atom can be excited to the $|F'=3, m_F = 1,2\rangle$ states and decay back into one of the Zeeman ground states that do not belong to the qubit space. The probability for such an event is strongly reduced as the respective states are shifted out of resonance by the red-detuned 1064 nm dipole trap. Furthermore, cavity birefringence generates small polarization imperfections (2%) such that the undesired transitions can be driven. However, the probability for such an event can be approximated as 2.4×10^{-4} which is negligible. The chance to lose an atom during the gate sequence (70 µs) is 2.0×10^{-5} and can be neglected as well. Employing a single-photon source, the gate efficiency could be boosted to unity. For such a scenario, there is no need to herald the photons after the reflection (see appendix section C).

4.4. Experimental Implementation of the Atom-Atom Gate: Entanglement Generation

A characteristic prerequisite of a quantum gate is its ability to generate entangled states from separable states. As shown theoretically in section 4.1, the gate mechanism can be used to generate a maximally entangled state between the two atoms. The employed protocol involves the creation of a coherent spin state on the equator of the generalized Bloch sphere initially. Afterwards, the sign of the $|\downarrow\downarrow\rangle$ component is changed via the reflection of a photon to generate entanglement. The polarization state of the reflected light is $|R\rangle$. A subsequent global $\pi/4$ rotation transforms the generated state into $|\Phi^-\rangle$. A detailed schematic of the employed circuit diagram is shown in figure 4.6.
The different states produced during the steps in the entanglement generation protocol can be visualized as a Husimi Q distribution on the generalized Bloch sphere. These states are shown in figure 4.7.

It should be noted that the gate operation step in figure 4.7 does not work in all trials. When optimized, the mode matching between the photons impinging onto the cavity and the cavity mode is 92%. Therefore, 8% of the reflected photons never interact with the cavity mode and cannot execute the gate. To quantify this effect, an experiment is performed. The atom pair is initially prepared in the state $|\downarrow\downarrow\rangle$. After the generation of $1/2(|\uparrow\uparrow\rangle - |\uparrow\downarrow\rangle - |\downarrow\uparrow\rangle + |\downarrow\downarrow\rangle)$, the gate operation is executed via the reflection of a weak coher-
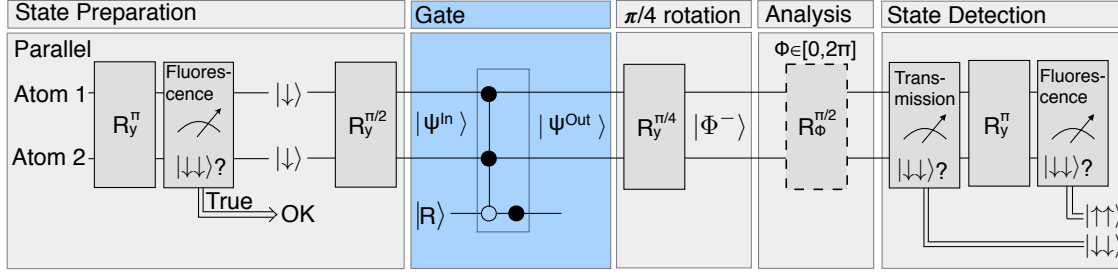
Figure 4.6.: Circuit diagram for entanglement generation via the gate. After generation of the state $|\uparrow\uparrow\rangle$ via optical pumping and a subsequent π rotation, a projection onto $|\downarrow\downarrow\rangle$ with a state detection pulse is employed. Afterwards, a $\pi/2$ rotation generates the state $\frac{1}{2}(|\uparrow\uparrow\rangle - |\uparrow\downarrow\rangle - |\downarrow\uparrow\rangle + |\downarrow\downarrow\rangle)$. The gate is then executed and followed by a global $\pi/4$ rotation to generate $|\Phi^-\rangle$. This state is characterized with an analysis pulse and the double state-detection protocol to extract the parity signal $\Pi(\phi)$.
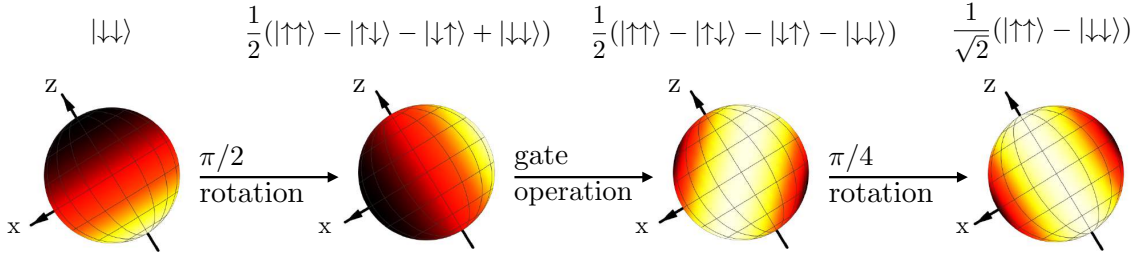
Figure 4.7.: Entanglement generation in via the gate mechanism. The figure shows the Husimi Q distributions of the states generated in the different steps of the entanglement generation protocol. In all cases, the color code is normalized and increases from dark (zero) to bright. The figure also gives an intuition for the necessity of a $\pi/4$ rotation to eventually generate the maximally entangled Bell state $|\Phi^-\rangle$ in the last step of the protocol.

ent pulse from the cavity ($\bar{n} = 0.13$). The last $\pi/4$ rotation of the entanglement generation protocol is omitted. If the gate works properly, ideally the state $1/2(|\uparrow\uparrow\rangle - |\uparrow\downarrow\rangle - |\downarrow\uparrow\rangle - |\downarrow\downarrow\rangle)$ should be generated. Besides the imperfect mode matching, another imperfection which can influence the experimental results is the accuracy of the phase shift associated with the photon reflection. On cavity resonance, the phase shift associated to the light reflection is exactly π, but may deviate from this value if the cavity mirrors vibrate mechanically such that the cavity resonance vibrates as well. Also, the laser has a finite frequency width and the laser frequency may slightly change. These effects deteriorate the phase shift mechanism [46]. In general, a phase Δ_{phase} is imprinted on the $|\downarrow\downarrow\rangle$ component of the two atom state. Thus, after the photon reflection, in general the state

$$|\psi_1\rangle = 1/2(|\uparrow\uparrow\rangle - |\uparrow\downarrow\rangle - |\downarrow\uparrow\rangle + e^{i\Delta_{\text{phase}}}|\downarrow\downarrow\rangle) \tag{4.9}$$

is generated. The Husimi Q distribution of this particular state can be written as

$$Q_1(\theta,\phi,\Delta_{\text{phase}}) = \frac{3}{32\pi}\Big(2\sin^2(\theta) + \cos^2(\theta) - \cos^2(\theta)(\cos(\Delta_{\text{phase}} - 2\phi)) \tag{4.10}$$
$$+ 2\sin(\theta)((\cos(\theta) - 1)\cos(\Delta_{\text{phase}} - \phi)$$
$$- (\cos(\theta) + 1)\cos(\phi)) + \cos(\Delta_{\text{phase}} - 2\phi) + 1\Big).$$

Additionally, the Husimi Q distribution of the state $|\psi_2\rangle = 1/2(|\uparrow\uparrow\rangle - |\uparrow\downarrow\rangle - |\downarrow\uparrow\rangle + |\downarrow\downarrow\rangle)$ can be expressed as

$$Q_2(\theta,\phi) = \frac{3}{16\pi}\Big(\cos(\phi)\sin(\theta) - 1 \Big)^2. \tag{4.11}$$

Due to the imperfect mode matching between the incoming photonic mode and the cavity mode, a mixture of the states $|\psi_1\rangle$ and $|\psi_2\rangle$ is generated. Accordingly, the measured distribution can be fitted with a model of the form

$$Q_{1,2}(\theta,\phi,a,\Delta_{\text{phase}}) = a \cdot Q_2(\theta,\phi) + (1-a)Q_1(\theta,\phi,\Delta_{\text{phase}}). \tag{4.12}$$

Figure 4.8 shows the Husimi distributions of $|\psi_1\rangle$ and $|\psi_2\rangle$ as well as the fit according to the model in equation 4.10 and the corresponding experimental data. The fit to the experimental data allows for inferring the values for the fit parametrers $a = 0.19 \pm 0.02$ and $\Delta_{\text{phase}} = (2.96 \pm 0.04)\,\text{rad}$. From the value of a, the proportion of mismatched light m can be extracted according to $a = m/(0.67(1-m) + m)$. This gives a value of $m = 0.14$ and thus a mode matching of 86%. The value of a is also influenced by dark counts of the SPDs employed to herald the presence of a photon in the reflected pulse. Thermal drifts of the coupling mirrors and an associated beam alignment are the reason of the slight deviation from the optimal mode matching of 92%.

After this characterization measurement, the phase shift is adjusted to π by an appropriate change of the frequency of the reflected photons. Additionally, the mode matching is optimized. Then, the full entanglement generation protocol including the last $\pi/4$ pulse is executed, to generate the Bell state $|\Phi^-\rangle$. Having performed the experimental protocol, the parity oscillation method is employed to extract the fidelity of the obtained state with the ideal Bell state. The experimental data showing the experimentally measured parity oscillation signal and the corresponding populations P_{ij} with $i,j \in \{\uparrow, \downarrow\}$ are shown in figure 4.9.

The experiment yields the populations of the produced state $P_{\uparrow\uparrow} = 48(3)\%$, $P_{\uparrow\downarrow} + P_{\downarrow\uparrow} = 9(2)\%$ and $P_{\downarrow\downarrow} = 42(3)\%$. To calculate the fidelity, the amplitude of the parity oscillation signal is inferred from a fit to the data. This amplitude is equal to $2\text{Re}(\rho_{\uparrow\uparrow,\downarrow\downarrow})$ and leads to an experimental value of $\text{Re}(\rho_{\uparrow\uparrow,\downarrow\downarrow}) = -31(2)\%$. These numbers allow to calculate a fidelity of

$$F(|\Phi^-\rangle) = \frac{1}{2}(P_{\uparrow\uparrow} + P_{\downarrow\downarrow}) - \text{Re}(\rho_{\uparrow\uparrow,\downarrow\downarrow}) = 76(2)\%. \tag{4.13}$$

To further characterize the gate, its entanglement capability is calculated. The entanglement capability $\mathcal{E}_\mathcal{C}$ is defined as the smallest eigenvalue of the partially transposed density matrix of the produced output state and was introduced in [163]. It can also be accessed via the smallest absolute negativity of all possible states with the entries of the density matrix measured experimentally. An ideal quantum gate that generates maximally
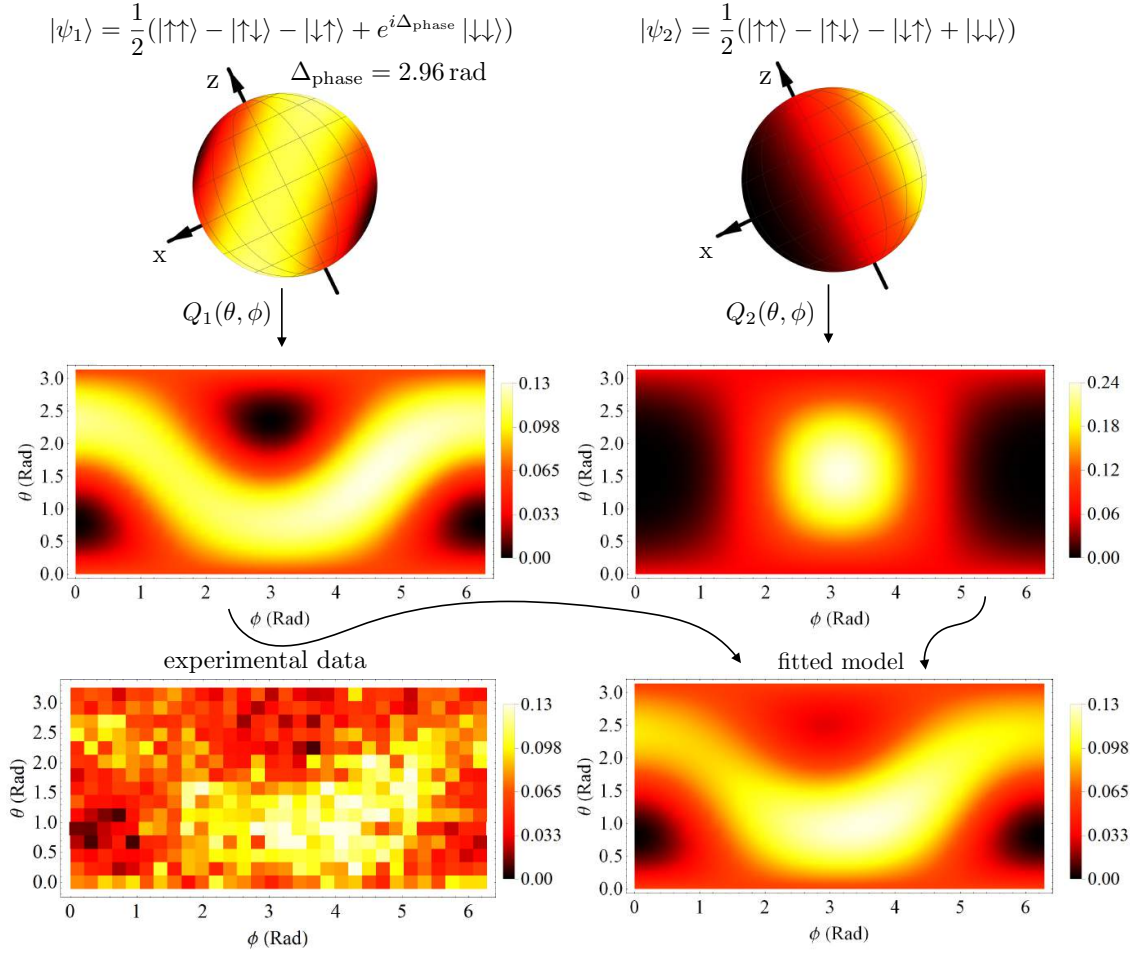
$$|\psi_1\rangle = \frac{1}{2}(|\uparrow\uparrow\rangle - |\uparrow\downarrow\rangle - |\downarrow\uparrow\rangle + e^{i\Delta_{\mathrm{phase}}}|\downarrow\downarrow\rangle)$$

$$|\psi_2\rangle = \frac{1}{2}(|\uparrow\uparrow\rangle - |\uparrow\downarrow\rangle - |\downarrow\uparrow\rangle + |\downarrow\downarrow\rangle)$$

$$\Delta_{\mathrm{phase}} = 2.96\,\mathrm{rad}$$

Figure 4.8.: The effect of imperfect mode matching on the Husimi Q distribution. The figure shows the Husimi distributions Q_1 and Q_2 of the states $|\psi_1\rangle$ (upper left graphics) and $|\psi_2\rangle$ (upper right graphics), respectively. A mixture of these states is produced due to imperfect mode matching. The lower right plot shows a fit to the experimental data which yields a fit value for the phase shift Δ_{phase} and for the mode matching. The lower left plot shows the corresponding experimental data.

entangled states with unity fidelity has an entanglement capability of $\mathcal{E}_{\mathcal{C}} = -0.5$ while a nonentangling gate has an entanglement capability of $\mathcal{E}_{\mathcal{C}} = 0$. It can be shown that the negativity of $\mathcal{E}_{\mathcal{C}}$ is a necessary and sufficient condition for the nonseparability of two qubits [164]. For the quantum gate presented here, the entanglement capability assumes the value $\mathcal{E}_{\mathcal{C}} = -0.26 \pm 0.02$.

The fidelity of the experimentally generated state with the ideal one is limited by several sources of error. The biggest error contribution is the finite mode matching of the gate-triggering photons to the cavity mode. After careful alignment of the respective coupling mirrors, a mode matching of 92% can be achieved. The non mode-matched parts of the photonic mode do not imprint a phase shift on the combined two-atom state in the cavity and thus leave the atoms in the unentangled state $\frac{1}{2}(|\uparrow\uparrow\rangle - |\uparrow\downarrow\rangle - |\downarrow\uparrow\rangle + |\downarrow\downarrow\rangle)$. Additional
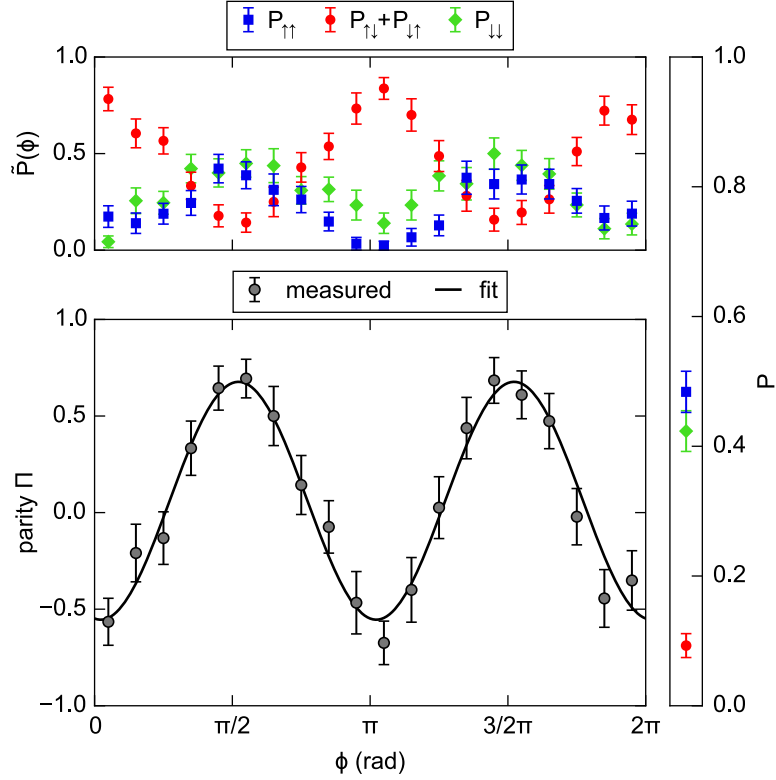
Figure 4.9.: Generation of the Bell state $|\Phi^-\rangle$ via the gate mechanism. The upper left plot shows the populations $\tilde{P}_{\uparrow\uparrow}$, $\tilde{P}_{\uparrow\downarrow} + \tilde{P}_{\downarrow\uparrow}$ and $\tilde{P}_{\downarrow\downarrow}$ oscillating with the phase ϕ of the analysis pulse. From these three curves, the lower left plot is derived which shows the parity Π as a function of ϕ. The error bars are standard deviations of the mean within the respective phase bin. The right column shows the direct population measurement of $P_{\uparrow\uparrow}$, $P_{\uparrow\downarrow} + P_{\downarrow\uparrow}$ and $P_{\downarrow\downarrow}$.

to the finite mode matching, there is a series of other sources of error that deteriorate the gate fidelity. These errors are summarized in table 4.2. Besides an erroneous state detection, multiphoton contributions are present in the weak pulses and cause an error

Table 4.2.: Sources of error in the atom-atom gate. Assuming an otherwise perfect gate operation, the numbers give the absolute fidelity reduction due to different sources of error.

Source of error	Fidelity reduction
finite mode matching	6%
errorneous state detection	4%
multi-photon contributions	3%
photon loss in the cavity	3%
heralding detector dark counts	2%
photon polarization inaccuracy	1%
atomic state preparation	1%
atomic state dephasing	1%

in the gate implementation. For an even photon number, the imprinted phase shift is a multiple of 2π and therefore equivalent to zero. In these cases, the produced state is separable. Experimentally, a mean photon number of $\bar{n} = 0.13$ was used and therefore there is a probability of 88%, 11% and 0.7% to observe zero, one and two photons in the pulse, respectively. The probability of two photons per pulse can be further reduced by employing an even weaker coherent pulse at the expense of gate efficiency and measurement time. Therefore, there is a tradeoff between the gate efficiency and the achieved fidelity. Additionally, the dark counts of the single-photon detectors dominate in the limit of vanishing $\bar{n}$. It is important to note that a single-photon source would not only eliminate the problem of the two-photon contributions, but also boost the efficiency of the gate as the strong zero photon contribution would be eliminated. Smaller sources of error include the imperfect photon polarization. It mainly results from cavity birefringence and was estimated to be in the 1% range. The last two sources of error are the imperfect atomic state preparation and the dephasing of the atomic state within the temporal window in which the gate is executed.

4.5. Independence of the Gate Mechanism on the Interatomic Distance

Generally, the implementation of a quantum gate between neutral atoms in their ground states is a difficult task because they do not interact over typical interatomic distances of a few micrometers. In the case of charged ions in a Paul trap, this problem was solved by employing an interaction via the shared vibrational modes in the trap [25]. However, this method is not applicable to neutral atoms. One way to circumvent this problem and make neutral atoms interact with each other is to promote them into highly excited electronic states, namely Rydberg states. In experiments demonstrating gates between Rydberg atoms, the principal quantum number n of such states is typically on the order of $n = 100$. Once excited into a Rydberg state, two atoms can influence each other over tens of micrometers via dipolar interactions, a principle that was used to implement the first quantum gate between neutral atoms back in 2010 [39]. One major difference of the gate presented in this thesis and the one based on atoms in Rydberg states [40] is that the spatial distance between the two atoms does not matter in the intracavity gate. As long as the atoms strongly couple to the cavity mode, the distance between them is irrelevant for the gate process. This property is beneficial when it comes to scaling up the number of qubits in the cavity. In contrast to the Rydberg gate, atoms do not have to be shuttled spatially and be brought in close proximity to execute a gate between them. This spatial proximity however is necessary for a Rydberg-based neutral atom gate.

In principle, many atoms could be trapped in the cavity mode and selectively addressed with laser beams impinging from a direction orthogonal to the cavity axis [44]. If a gate operation between two atoms out of a larger ensemble should be executed, they can be shifted into cavity resonance via an ac-Stark shift imparted by the addressing laser. Afterwards, a photon reflected from the cavity can execute the gate. Such an architecture allows for gates between any two spatially stationary atoms out of a larger ensemble in the

cavity. This would also allow for the construction of a quantum register inside a quantum network node. For such a quantum register, the implementation of an addressing system as described in [44] is a necessary prerequisite as it allows to tune two or more atoms from the register into cavity resonance and to detune the remaining atoms. An addressing system has already been built and tested in the Pistol experiment in the quantum dynamics division [44], but remains to be implemented in the QGate experiment. The availability of an addressing system would furthermore facilitate the generation of any desired separable set of two-qubit basis states as input states for the atom-atom gate. This also means that the carving technique is not necessary anymore as a preparatory step.

4.6. Theoretical Calculation of the Expected Gate Fidelity

In this section a theory is developed that allows to predict the overlap of states produced utilizing the atom-atom gate mechanism with expected ideal states. The theory is based on the cavity input-output formalism outlined in [113]. In this framework, an impinging photon $|p_{\text{in}}\rangle$ can end up in different mutually orthogonal output modes of the atom-atom-cavity system.

Ideally, the photon is reflected and leaves the system via the reflection mode $|p_{\text{r}}\rangle$. In this case, the gate between the two atoms inside the cavity is executed as desired. In a real system however, one has to consider a number of undesired output modes. One of these output modes describes the transmission through the cavity. It is labeled $|p_{\text{t}}\rangle$. With N being the number of coupling atoms in the cavity, the photon can also be scattered from the ith atom and end up in the scattered mode $|p_{\text{ai}}\rangle$. Furthermore, the photon can be scattered from the cavity mirrors and populate the mode $|p_{\text{m}}\rangle$. Figure 4.10 shows the different output channels of the atom-atom-cavity system graphically. The field amplitudes corresponding to the aforementioned modes are labeled as r, t, a and m. The cavity employed in the experiment has the parameters $(g, \kappa, \gamma) = 2\pi(7.8, 2.5, 3.0)\,\text{MHz}$ for $N = 1$ coupling atom (see section 2.3). The total cavity decay rate κ has three contributions, namely the decay through the incoupling mirror κ_{r}, the decay through the other cavity mirror κ_t and the scattering rate from the cavity mirrors κ_{m}. Thus, $\kappa = \kappa_{\text{r}} + \kappa_{\text{t}} + \kappa_{\text{m}}$. The respective decay rates are given by $\kappa_{\text{r}} = 2\pi \times 2.29\,\text{MHz}$, $\kappa_{\text{t}} = 2\pi \times 0.09\,\text{MHz}$ and $\kappa_{\text{m}} = 2\pi \times 0.13\,\text{MHz}$. The amplitudes of the different output modes can be calculated according to input-output theory [112, 113]. On resonance, the closed expressions for the different modes read

$$r(N) = \frac{Ng^2 + (\kappa - 2\kappa_r)\gamma}{Ng^2 + \kappa\gamma} \tag{4.14}$$

$$t(N) = \frac{2\sqrt{\kappa_r \kappa_t}\gamma}{Ng^2 + \kappa\gamma} \tag{4.15}$$

$$m(N) = \frac{2\sqrt{\kappa_r \kappa_m}\gamma}{Ng^2 + \kappa\gamma} \tag{4.16}$$

$$a(N) = \frac{2\sqrt{\kappa_r \gamma}\sqrt{N}g}{Ng^2 + \kappa\gamma}. \tag{4.17}$$

Table 4.3.: Field amplitudes of the different possible output modes.
The sign change in the reflection mode r(N) when changing from $N = 0$ to $N = 1$ is due to the phase shift mechanism in reflection. The transmission amplitude decreases for increasing N since the cavity is blocked by the coupling atoms. This is also the reason why the scattering from the cavity mirrors decreases with increasing N.

N	0	1	2
$r(N)$	-0.82	0.80	0.89
$t(N)$	0.36	0.04	0.02
$m(N)$	0.43	0.05	0.03
$a(N)$	0.00	0.60	0.45

These expressions can be evaluated for $N = 0,1,2$ coupling atoms in the cavity. The corresponding values for r, t, m and a are given in table 4.3. Importantly, the amplitudes fulfill the normalization condition $|r(N)|^2 + |t(N)|^2 + |m(N)|^2 + |a(N)|^2 = 1$.

As a next step, the reflection process of a photon from the atom-cavity system is investigated. Before the reflection, the atom and the photon can be considered as separable particles. In the basis of the two states $|\uparrow\rangle$ and $|\downarrow\rangle$, one can write down a basis for the two-atom Hilbert space: $|a_0\rangle = |\uparrow\uparrow\rangle$, $|a_1\rangle = |\uparrow\downarrow\rangle$, $|a_2\rangle = |\downarrow\uparrow\rangle$ and $|a_3\rangle = |\downarrow\downarrow\rangle$. The initial two-atom state is described by the density matrix ρ_a, whereas the initial photon state is described by $|p_{\text{in}}\rangle\langle p_{\text{in}}|$. Therefore, the atom-photon state before the reflection can be expressed as

$$\rho_a \otimes |p_{\text{in}}\rangle\langle p_{\text{in}}| = \sum_{i,j=0}^{3} a_{i,j} |a_i\rangle\langle a_j| \otimes |p_{\text{in}}\rangle\langle p_{\text{in}}| \,. \tag{4.18}$$

After the reflection process, this state becomes

$$\rho_{a,p} = \sum_{i,j=0}^{3} a_{i,j} |a_i\rangle\langle a_j| \otimes |p_i\rangle\langle p_j| \tag{4.19}$$
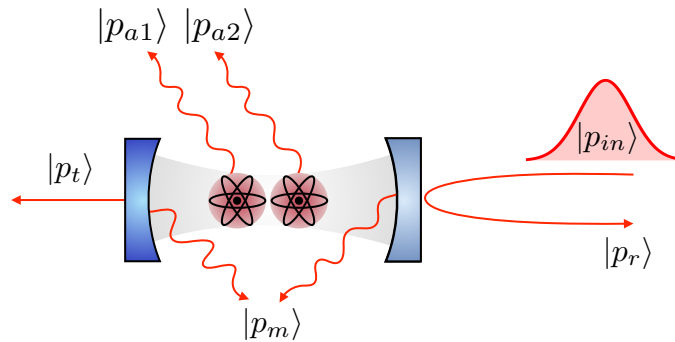
Figure 4.10.: Output modes of the atom-cavity system. An impinging photon $|p_{\text{in}}\rangle$ can be directed into four different output channels. The desired output mode is the reflection mode $|p_r\rangle$. However, the photon can also be transmitted through the cavity and populate the mode $|p_t\rangle$. Additionally, the photon can be scatterd by the atoms ($|p_{ai}\rangle$). Another scattering process is described by $|p_m\rangle$, the scattering of the photons from the cavity mirrors.

where the $|p_k\rangle$ with $k \in \{0,1,2,3\}$ are given by

$$|p_0\rangle = r(2) |p_r\rangle + t(2) |p_t\rangle + m(2) |p_m\rangle + \frac{a(2)}{\sqrt{2}} (|p_{a1}\rangle + |p_{a2}\rangle)$$
$$|p_1\rangle = r(1) |p_r\rangle + t(1) |p_t\rangle + m(1) |p_m\rangle + a(1) |p_{a1}\rangle$$
$$|p_2\rangle = r(1) |p_r\rangle + t(1) |p_t\rangle + m(1) |p_m\rangle + a(1) |p_{a2}\rangle$$
$$|p_3\rangle = r(0) |p_r\rangle + t(0) |p_t\rangle + m(0) |p_m\rangle . \tag{4.20}$$

Compared to the input state $\rho_a \otimes |p_{\text{in}}\rangle \langle p_{\text{in}}|$, the state after the reflection is in general an entangled state. After this state is generated, the photons are absorbed quickly. The desired scenario where the photon is detected in the reflected mode $|p_r\rangle$ is of special interest because single-photon detectors can measure these photons and a postselection on the cases in which a herald click was detected can be applied. In these cases, the state is projected onto

$$\rho_{a,out}^{\text{herald}} \mathcal{N} = \langle p_r| \rho_{a,p} |p_r\rangle \tag{4.21}$$
$$= \rho_a \circ \Big((r(2), r(1), r(1), r(0))^\dagger \cdot (r(2), r(1), r(1), r(0)) \Big) \tag{4.22}$$
$$=: \rho_a \circ G_{\text{herald}} \tag{4.23}$$
$$= \rho_a \circ \begin{pmatrix} 0.80 & 0.71 & 0.71 & -0.74 \\ 0.71 & 0.64 & 0.64 & -0.66 \\ 0.71 & 0.64 & 0.64 & -0.66 \\ -0.74 & -0.66 & -0.66 & 0.68 \end{pmatrix} . \tag{4.24}$$

The symbol $\circ$ denotes the elementwise product or Hadamard product[1] while $\mathcal{N}$ is a normalization factor which is defined by $\mathcal{N} = \text{Tr}(\rho_a \circ G_{\text{herald}})$. The elements on the diagonal of G_{herald} can be interpreted as the probability of a heralding event assuming a single-photon detector with unity efficiency. The probability to obtain such a heralding event depends on the number of coupling atoms in the cavity N. This number determines the amount of light reflected back from the cavity. N also determines the frequency difference between the two normal mode peaks in the reflection spectrum of the atom-cavity system. As there is a phase difference of π between the phase of the reflected light in the coupling and the non-coupling case, one obtains the minus signs on the off-diagonal in the fourth column and row of G_{herald}.

The second case to consider is the one where no postselection on the herald click is applied. In this case, the photon can leave into any of the possible output modes and is finally absorbed. In this situation, no postselection is performed and all measurement runs are

---

[1]The Hadamard product of two matrices A and B is defined as
$$A \circ B = (a_{ij} \cdot b_{ij}) = \begin{pmatrix} a_{11} \cdot b_{11} & \cdots & a_{1n} \cdot b_{1n} \\ \vdots & \ddots & \vdots \\ a_{m1} \cdot b_{m1} & \cdots & a_{mn} \cdot b_{mn} \end{pmatrix}$$

evaluated together. To obtain the eventual density matrix $\rho_{a,\text{out}}^{\text{total}}$ of the two atoms in the cavity, one has to trace over all possible photonic output modes and obtains

$$\rho_{a,\text{out}}^{\text{total}} = \text{Tr}_\rho \Big(\sum_{i,j=0}^{3} a_{i,j} \, |a_i\rangle \, \langle a_j| \otimes |p_i\rangle \, \langle p_j| \Big) \tag{4.25}$$

$$= \sum_{i,j=0}^{3} a_{i,j} \, |a_i\rangle \, \langle a_j| \, \langle p_j| \, p_i\rangle$$

$$:= \rho_a \circ G_{\text{total}}$$

$$= \rho_a \circ \begin{pmatrix} 1.00 & 0.90 & 0.90 & -0.72 \\ 0.90 & 1.00 & 0.64 & -0.62 \\ 0.90 & 0.64 & 1.00 & -0.62 \\ -0.72 & -0.62 & -0.62 & 1.00 \end{pmatrix}.$$

The elementwise multiplication with the matrix G_{total} has no influence on the populations on the diagonal, but reduces the off-diagonal elements of the density matrix. The reason for this is the leakage of information into all possible photonic modes and therefore eventually into the environment.

Input-output theory thus allows to calculate the density matrix describing the two-atom system after the reflection of a single photon. In practice, no single-photon source was employed to perform the experiments, but it is nevertheless worthwile to calculate the expected fidelity for the case of a single-photon source. There are two possible scenarios. On the one hand, the herald can be employed to make sure that the photon made its way back into the reflection mode of the cavity. On the other hand, the heralding can be suspended in which case the photon has a finite chance to be scattered into one of the undesired orthogonal output modes of the cavity. Experimentally, both atoms are initially prepared in an equal superposition state of $|\uparrow\rangle$ and $|\downarrow\rangle$. The two-atom state can be written as $|a_{in}\rangle = \frac{1}{2}(|\uparrow\uparrow\rangle - |\uparrow\downarrow\rangle - |\downarrow\uparrow\rangle + |\downarrow\downarrow\rangle)$. The initial two-atom density matrix $\rho_{a,\text{in}} = |a_{in}\rangle \, \langle a_{in}|$ is transformed into $\rho_{a,out}^{\text{herald}} = \rho_{a,in} \circ G_{\text{herald}} / \text{Tr}(\rho_{a,in} \circ G_{\text{herald}})$ or $\rho_{a,out}^{\text{total}} = \rho_{a,in} \circ G_{\text{total}}$ depending on whether the herald is applied or not. In the latter case, a $\pi/4$ rotation after the reflection of the photon from the cavity leads to a state whose fidelity with the maximally entangled state $|\Phi^-\rangle$ is given by

$$F = \langle \Phi^- | \, \rho_{a,\text{out}}^{\text{total}} \, | \Phi^- \rangle = 79.2\%. \tag{4.26}$$

Thus, a non-heralded application of the gate would lead to a decent fidelity if a single-photon source is applied. If the herald is applied, equation 4.24 allows to calculate the state after the photon reflection. If this state is rotated once again by a global $\pi/4$ pulse, the fidelity with the maximally entangled state $|\Phi^-\rangle$ is

$$F = \langle \Phi^- | \, \rho_{a,\text{out}}^{\text{herald}} \, | \Phi^- \rangle = 99.7\%. \tag{4.27}$$

In this case, the fidelity is close to unity as the herald makes sure that the photon is directed into the reflection mode and does not scatter from the atoms or the mirrors. The herald also ensures that it is not transmitted through the cavity. The deviation of the fidelity from unity stems from the slightly different reflectivity $|r(N)|^2$ for different numbers of

coupling atoms.

The previous calculations assumed a single photon impinging onto the cavity. In reality, the experiment was performed with weak coherent pulses in which the actual photon number is not well defined. The photon number distribution in such a pulse has a Poissonian statistics and the mean photon number per pulse can be adjusted with neutral density filters. The Poisson distribution can be expressed as $P(n) = (\bar{n}^n/n!)\,e^{-\bar{n}}$ and $\bar{n} = \sum_{n=0}^{\infty} n \cdot P(n)$. In the atom-atom gate experiment, a mean photon number of $\bar{n} = 0.13$ was chosen. To obtain an estimate on the different error sources in the experiment, different outcomes of the experiment have to be modeled and the resulting density matrix needs to be weighted with the probability to measure a click in the heralding single-photon detector. The resulting density matrix is a weighted sum of all possible combinations. As an example, a possible case is the one where no photon is present in the reflected pulse, but a dark count in the detector occurs. In this case, the final state results from a global $\pi/4$ rotation of $\frac{1}{2}(|\uparrow\uparrow\rangle - |\uparrow\downarrow\rangle - |\downarrow\uparrow\rangle + |\downarrow\downarrow\rangle)$ and its density matrix can be written as

$$\rho = \begin{pmatrix} 0.729 & -0.302 & -0.302 & 0.125 \\ -0.302 & 0.125 & 0.125 & -0.052 \\ -0.302 & 0.125 & 0.125 & -0.052 \\ 0.125 & -0.052 & -0.052 & 0.021 \end{pmatrix}. \tag{4.28}$$

This state has a fidelity of 1/4 with the maximally entangled Bell state $|\Phi^-\rangle$. When one photon is reflected two possible scenarios can occur. In the first scenario, the photon is not lost and makes its way to the single-photon detector. In this scenario, the operator G_{herald} applies. In the second case, the photon is lost in the reflection process and no heralding can be applied. Then, the operator G_{total} can be applied. When multiple photons are present in the reflected pulses, the respective operators have to be applied in a concatenation. The multiplication of the respective matrices leads to a density matrix with reduced coherence terms and therefore to a reduction of the fidelity. If one considers the total photon detection efficiency and the detector dark count rate of 0.002 per pulse, an entangled state fidelity of 91.1% can be reached. Additionally, the main experimental sources of error can be introduced in the model. These include the imperfect mode matching of the photonic mode to the cavity mode (92%), the imperfect state detection of the two atoms (3%) and the multiphoton contributions that lead to a single heralding event (8% for $\bar{n} = 0.13$). Furthermore, the photon polarization error is estimated to be 1%, just as the imperfect atomic state preparation via optical pumping along the cavity axis. The decoherence of the atomic qubit in the time interval of $14\,\mu s$ between preparation and readout is also on the order of 1%, limited by magnetic field fluctuations. Inclusion of all these error sources leads to an expected fidelity of 77% which is in good argement with the experimentally observed value of 76(2)%. The simulation can assign a value of the fidelity reduction for each of the discussed sources of error (see table 4.2). It shows that the finite mode matching is the biggest source of error and leads to a fidelity reduction of 6%. The state detection error leads to a fidelity reduction of 4%. To increase the gate fidelity, an improvement of the mode matching is therefore indispensable. It has been demonstrated recently that the mode matching can be increased from 92% to 98% in the Pistol experiment in the Rempe group. The simulation predicts that the expected fidelity would increase from 77% to 82% with this improvement.

4.7. Expected Fidelity and Efficiency with a Single Photon Source

As discussed in section 4.6, the experiment was performed with weak coherent pulses containing an average photon number of $\bar{n} = 0.13$. The high probability to observe zero photons in such a pulse leads to a severe reduction of the gate efficiency. Although decent fidelities with maximally entangled states can be achieved via postselection, the efficiency of the gate suffers from the low mean photon number in these pulses. In future applications of the gate it would therefore be beneficial to employ a single-photon source to boost the efficiency and the fidelity. Such a source needs the proper bandwidth characteristics to be compatible with the cavity bandwidth [46]. Only then, the phase shift mechanism employed to execute the gate would work as desired. When postselection on the photon in the reflected mode is applied, the fidelity increases from 76% (as measured in the experiment where the gate was executed with a weak coherent pulse) to 82% while the efficiency increases from 4.2% to 32%. A detailed calculation of the gate fidelity with a single-photon source can be found in the appendix C. If a single-photon source is available, the achievable gate efficiency is mainly limited by the reflection amplitude of the cavity and the detection efficiency of the single-photon detectors. Importantly, multiphoton contributions would be eliminated thereby. The elimination of these contributions is the main source for the increase of fidelity. Additionally, the fidelity would increase slightly because the heralding makes sure that the single photon is not lost in the reflection process.

To make the scheme deterministic in the experimental framework, the heralding process could be omitted entirely. Then, the cases in which the photon was lost in the reflection process would contribute to the experimental data. The simulation shows an expected fidelity of 68% and an efficiency of 100%. The reduction from 82% to 68% is dominated by the photon loss processes into the different loss channels, while additional errors are the imperfect mode matching and the imperfect state detection. The expected value for the fidelity is still higher than the classical threshold of $F = 50\%$.

To summarize the different scenarios with a single-photon source and with weak coherent pulses employed to execute the gate, table 4.4 lists the different possibilities with the corresponding efficiencies and fidelities.

A highly efficient gate would be of great importance for the achievable rate of an entanglement swapping protocol in a quantum repeater architecture [74].

Table 4.4.: Summary of different scenarios for the gate execution.
The table lists the different scenarios in which the gate is executed employing weak coherent pulses or a single-photon source. Also, the heralding can be switched on and off as a tradeoff between the gate efficiency and the fidelity with expected maximally entangled states.

Gate execution with	Postselection?	Fidelity with $\lvert \Phi^- \rangle$	Gate efficiency
coherent pulse ($\bar{n} = 0.13$)	yes	76%	4.2%
single-photon source	yes	82%	32%
single-photon source	no	68%	100%

4.8. Entanglement Swapping in a Quantum Repeater Protocol

The demonstrated quantum gate between two atoms can serve in an entanglement swapping protocol to generate entanglement between two distant network nodes over large distances. The corresponding theoretical proposal was outlined in [74]. In this protocol, the cavity containing two atoms assumes the role of a quantum repeater node [62] placed halfway between the remote nodes. To perform entanglement swapping on such a repeater node, individual addressing of the atoms and the application of the two-atom gate are necessary. As outlined in [74], the entanglement swapping is performed by a series of Hadamard gates on the individual atoms, interleaved with the two-atom gate. Eventually, state detection is applied to both of the two atoms and a classical feedback on one of the remote network nodes is performed. To increase the efficiency and the fidelity of the protocol, the atom-atom gate should be executed with single photons impinging onto the cavity. For the construction of such a single-photon source, vacuum-stimulated Raman adiabatic passage (vSTIRAP) with a single atom in an additional cavity can be employed. Using this technique, single-photon sources with photon generation efficiencies of 56% on the D_2 line of ^{87}Rb have been achieved [165].
Employing the gate in an entanglement swapping protocol in combination with individual addressing of the atoms would be a promising future application of the reflection mechanism.

5. Summary and Outlook

In this doctoral work the implementation of a quantum gate between two neutral atoms inside a high-finesse optical cavity was achieved (Welte et al. PRX 8, 011018 (2018) [43]). Furthermore, a heralded generation of entanglement based on the method of quantum state carving was established (Welte et al. PRL 118, 210503 (2017) [42]). A prerequisite for both experiments is the ability to trap, cool and globally manipulate two neutral atoms at the center of the cavity [166]. The presented protocols do not rely on the ability to individually address the two qubits. Experimental techniques to optically pump the atoms into parallel and antiparallel spin configurations were developed. Furthermore, a two-step protocol for state detection was developed that allows for a simultaneous readout. These tools were an essential prerequisite for the generation and characterization of the experimentally generated entangled two-atom states.

To execute the atom-atom quantum gate or the carving procedure, weak coherent optical pulses are reflected from the single-sided cavity. While the carving technique does not necessarily rely on single photons impinging onto the cavity, the atom-atom gate does. The latter can nevertheless be executed with weak coherent pulses in combination with a postselection on the cases in which a single photon was present in the pulse. This way of operating the atom-atom gate leads to a non-unity efficiency.

In future experiments, a single-photon source could be used. This would render postselection unnecessary and thus enhance the gate efficiency. Such a single-photon source would also increase the gate fidelity. The reason for this is that two-photon contributions in the employed coherent states lead to a phase shift of 2π instead of π and therefore to a degradation of the fidelity. The same holds for the higher even photon number contributions $|n\rangle$ which imprint a phase shift of $n\pi$. These higher photon number contributions could be eliminated by reflecting single photons to execute the gate.

A neutral atom in a second optical cavity can serve as a source of such photons [165] employing a vSTIRAP protocol [167]. An alternative approach to generate single photons is to use a second atom-cavity system and reflect weak coherent pulses from it. In this case, the atom in the cavity can act as a herald for the presence of a single photon in the optical pulse [168]. In this thesis a theory was developed that allows to estimate the expected fidelity of states generated with the gate mechanism employing a single-photon source. The theory predicts fidelities of 82% when postselection on succesful photon reflection is applied. When postselection is not applied, the model predicts a fidelity of 68% in combination with a gate efficiency of unity.

The execution time of the atom-atom gate is $2\,\mu s$, limited by the bandwidth of the employed cavity. This is faster than gates performed with neutral atoms prepared in

Rydberg states (7 µs) [39]. The construction of a spectrally broader cavity would allow for an even faster execution.

The quantum gate presented in this thesis opens the route towards novel applications within a quantum network. As an example, it establishes a valuable tool for the construction of a quantum repeater based on network nodes consisting of neutral atoms in optical cavities. In this architecture the atom-atom-cavity system can serve as quantum repeater station and the atom-atom gate allows for the distribution of entanglement over large distances [74]. Probabilistic entanglement swapping can be achieved with the carving technique. The atom-atom gate can furthermore be employed to implement superdense coding in quantum networks where two bits of classical information can be transmitted by sending only one qubit [169].

Network nodes that contain multiple qubits and exhibit the ability to perform gate operations between them offer the possibility of local quantum computation in a quantum network. In this context it is important to note that the demonstrated gate mechanism is scalable to qubit numbers larger than two. Therefore, a future experimental platform could be implemented with a register of several qubits in one cavity and an addressing system that allows to tune any desired qubit into and out of cavity resonance via application of an ac-Stark shift. In such a platform, gates between any subset of the register can be executed by tuning the respective atoms into cavity resonance and the subsequent reflection of a photon to execute the gate. The individual addressing of atoms inside a cavity has already been demonstrated in the Pistol experiment of the Rempe group where an addressing beam was used to deterministically prepare a desired number of atoms by 'shooting out' the undesired atoms selectively [44].

The experimental setup could be combined with the platform of optical tweezers [170–175]. Recent experiments with this platform have demonstrated that tens of atoms can be arranged in any desired spatial configuration [176]. To achieve this, two techniques can be employed. The first technique relies on an acousto-optical deflector (AOD) that is supplied with a signal containing many different frequency components. A laser beam passing the AOD is diffracted by the different tunable radiowaves and later focussed into a vacuum chamber where the generated tweezers are used as single-atom traps. The second technique relies on a spatial light modulator (SLM). A phase pattern can be imprinted electronically on this device that translates into an array of tweezers after being focussed into a vacuum chamber. In this setup an additional movable tweezer can be employed to sort atoms into the desired tweezers [172]. The Browaeys group in Paris has demonstrated that arbitrary arrangements of atoms in 1D, 2D and 3D can be realized experimentally [176]. The combination of a tweezer setup with an optical cavity would allow for unprecedented control of neutral atoms coupled to a single mode of light. To maximize the localization of the atomic wavepackets in the tweezers, ground state cooling can be applied [177]. This allows to localize the ground state wavepacket of the atoms in the transversal directions to a few tens of nanometers.

In a setup combining the optical tweezer platform with a cavity, hybrid gates between photons reflected from the cavity and several intracavity atoms could be realized. In the

simplest configuration, a Toffoli gate between one photon and two intracavity atoms could be implemented. Furthermore, a register of many atoms could be trapped in such a way that all of them spatially overlap with the antinodes of the cavity mode. The possibility to reload atoms out of a reservoir in case one of them is lost from a tweezer [173] would provide a quasi-permanently available set of register qubits. A possible way to decouple the atoms from the cavity mode relies on moving them from the antinodes of the cavity mode to the nodes. Alternatively, the amplitude of the radio frequency signals supplying the respective AOM could be used to impart an ac-Stark shift on desired atoms in the ensemble trapped in the cavity. Both methods can be used to tune two or more atoms out of an ensemble into cavity resonance. Once this step is completed, a photon can be reflected to execute a gate between these selected atoms. The ability to trap and couple three atoms in one cavity would furthermore allow for the experimental implementation of heralded quantum gates between two atoms where the additional atom serves as an ancilla [178, 179] indicating a successful gate operation. The gates performed with this method do not depend on the interatomic distance, a feature that distinguishes them from quantum gates and entanglement generation protocols based on the Rydberg blockade effect [39,40,122,180,181].

In the situation where only one atom is present in the cavity mode, a remote gate between two atoms in spatially separated cavities can be implemented in a future experiment. In a network, where single atoms are trapped in optical cavities, a photon can be reflected from two such atom-cavity systems in succession. Therefore, the phase shift mechanism is employed twice. Similar schemes have been proposed for neutral atoms [182] and rare earth ions [183]. The protocol to realize such a gate would be analogous to the protocol employed for a photon-photon gate [35] with inversed roles of atoms and photons. In the Rempe group, a remote gate could be implemented between the QGate and the Pistol setups. These two experiments have already been connected with an optical fiber (length: 60 m) for network experiments in 2012 [45]. An important prerequisite for such an experiment is the active stabilization of polarization drifts in the fiber connecting the two setups. This stabilization can be achieved with a polarization controller that was recently implemented and tested in the lab [184]. The polarization compensation method is based on the hardware also employed in the group of Weinfurter for a similar purpose [185, 186].

The versatile nature of the employed phase shift mechanism can be recognized by the fact that two groups in the field of superconducting qubits have recently used it to nondestructively detect microwave photons [107, 108] with a similar protocol to the one used in the optical domain [101]. This method to implement quantum gates can be transferred to any physical platform where three-level material quantum systems can be coupled to a cavity. Therefore, the protocol to execute the atom-atom gate presented in chapter 4 can also be employed with two superconducting qubits coupled to a microwave cavity. These examples demonstrate that the experiments outlined in this thesis pave the way towards further powerful tools in different implementations of quantum networks.

A. Detailed Level Structure of the ^{87}Rb D$_2$ and D$_1$ Lines

A detailed level scheme of the D_2 and D_1 lines of the employed ^{87}Rb atoms is presented in figure A.1. The levels relevant for the experiments described in this thesis are the two long-lived ground states $|F = 1\rangle$ and $|F = 2\rangle$ in the $5^2\mathrm{S}_{1/2}$ manifold. The magnetic substates $|F = 1, m_F = 1\rangle = |\downarrow\rangle$ and $|F = 2, m_F = 2\rangle = |\uparrow\rangle$ define a qubit in the atomic level structure. The qubit can be experimentally manipulated with a pair of Raman lasers. The excited state $|F' = 3\rangle$ is separated energetically by an optical transition at 780.24121 nm from the two ground states (D_2 line). The optical cavity is locked to the transition $|F = 2, m_F = 2\rangle \rightarrow |F' = 3, m_F = 3\rangle$. The other excited states in the $F' = 0,1,2$ manifolds are naturally detuned by hundreds of MHz and can therefore be neglected. The hyperfine energy splitting is 6.83468 GHz and sets the transition frequency of the employed qubit.
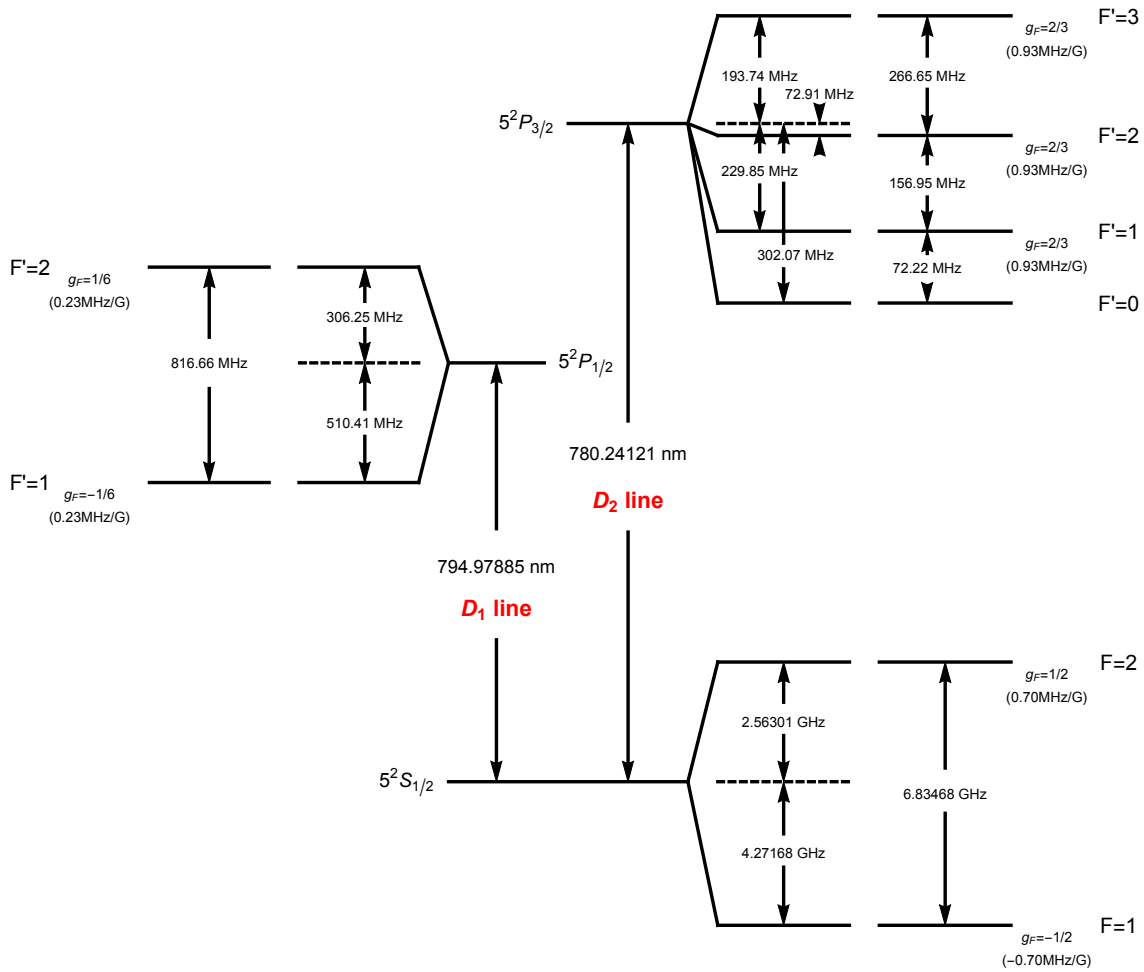
Figure A.1.: Level scheme of ^{87}Rb. The graphics (adapted from [187]) shows a detailed level scheme of the D_1 and the D_2 line. For the atom-atom gate and the carving technique, the two hyperfine states $|F = 1\rangle$ and $|F = 2\rangle$ are most relevant as the chosen atomic qubit is comprised of two Zeeman substates out of these two manifolds. Also, the excited state manifold $F' = 3$ is relevant as the cavity is tuned into resonance with the transition from $|F = 2, m_F = 2\rangle$ to $|F' = 3, m_F = 3\rangle$.

B. Experimental Setup in Detail
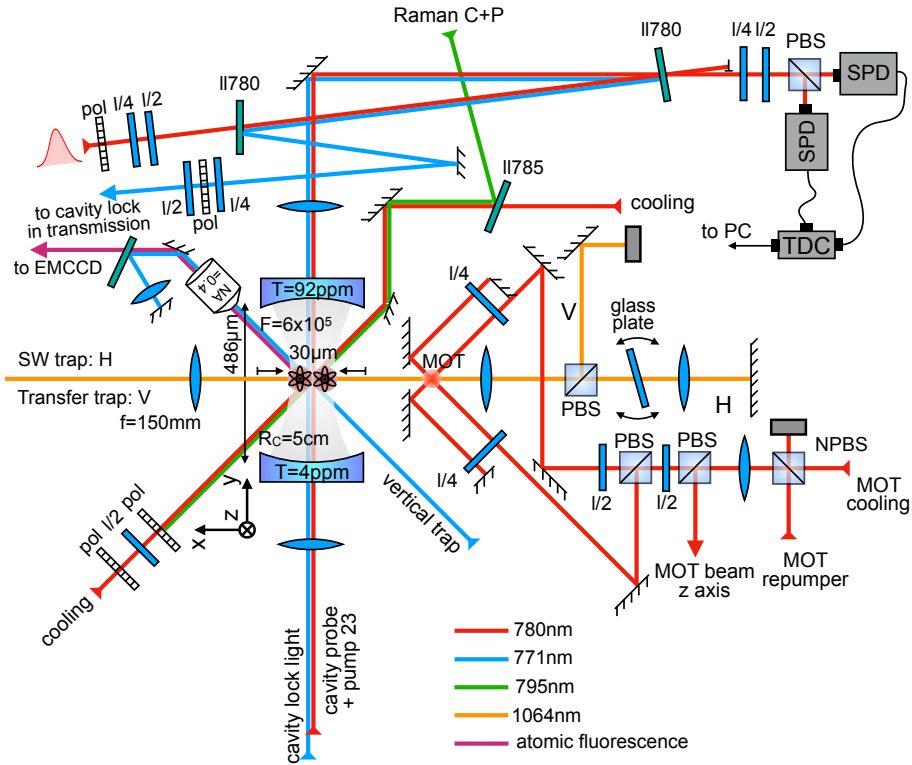
Figure B.1.: Experimental setup. A detailed sketch of the experimental setup is shown. The abbreviations used are (N)PBS for (non-)polarizing beam splitter, pol for polarizer and $l/2$ and $l/4$ for half-wave and quarter-wave plates, respectively. Furthermore, ll780 and ll785 are laser line filters from the manufacturer Semrock [188, 189]. A magneto-optical trap (MOT) is employed to trap a cloud of cold atoms. The vertical MOT beam is not shown. The atoms are transferred into the cavity with a vertically (V) polarized laser beam focussed halfway between the MOT position and the cavity center. The transport mechanism is lossy and an appropriate adjustment of the MOT size allows to transfer only one or two atoms into the cavity on average. Once the atom arrives at the cavity center, the 770 nm and 1064 nm standing wave traps are switched on. A glass plate in the 1064nm dipole trap beam path is placed on a galvanometric scanner and can be employed to position the atoms to the center of the cavity mode. The atoms are monitored with an EMCCD camera via a high NA objective. Light coming out of the cavity (positive y direction) generates voltage pulses in the single-photon detectors (SPDs). These voltage pulses are digitized with a time-to-digital converter (TDC) and the resulting files are processed with an evaluation software. Weak coherent pulses (upper left corner) are extracted via a ll780 filter and impinge on the cavity mirror with the higher transmission. These pulses are employed to execute the atom-atom gate.

C. Expected Fidelity of Entangled States Employing a Single-Photon Source

In this chapter, the expected fidelity of an entangled state with an ideally expected Bell state is calculated. The entangled state is produced with the atom-atom gate mechanism and a (hypothetical) ideal single-photon source is assumed for the execution of the gate. When such a single-photon source is available, two scenarios are possible. In the first scenario, the gate is performed without postselection on the cases in which the photon bounces off the cavity and generates a click in a single-photon detector monitoring the cavity reflection mode. In this case, the efficiency of the atom-atom gate is unity at the expense of the gate fidelity. The fidelity is reduced since there are cases in which the photon is scattered into one of the loss modes of the cavity. In the second scenario, these cases can be excluded by applying the heralding process such that only the cases are considered in which the photon is successfully reflected from the atom-atom-cavity system. Here, the fidelity of the gate will increase at the expense of gate efficiency. The theoretically expected fidelities and efficiencies are calculated to obtain an intuition for the performance of the gate in both scenarios. As the calculations show, entangled states with a fidelity of 68% with ideally expected Bell states can be generated with an efficiency of unity when a single-photon source is employed and the heralding process is switched off. If the heralding is switched on, an entangled state with a fidelity of 82% can be generated with an efficiency of 32%.

C.1. Expected State Fidelity Employing a Single-Photon Source Without Heralding

For the calculation, the framework of cavity input-output theory is employed. This theory predicts amplitudes for the reflectivity r and the transmission t of the cavity, the scattering of light from the atoms a and the mirror losses m for different numbers of coupling atoms N. The absolute squared value of these complex quantities gives the respective intensity[1]. The reflected and the transmitted light is accessible for the experimenter while the light

---

[1]As an example, the absolute squared value of the reflection amplitude $|r(N)|^2$ was studied in the normal mode spectroscopy measurements in section 3.4.1.

scattered from the atoms and the cavity mirrors cannot be measured easily. The closed expressions for the respective amplitudes on resonance are [112, 113]

$$r(N) = \frac{Ng^2 + (\kappa - 2\kappa_r)\gamma}{Ng^2 + \kappa\gamma} \tag{C.1}$$

$$t(N) = \frac{2\sqrt{\kappa_r \kappa_t}\gamma}{Ng^2 + \kappa\gamma} \tag{C.2}$$

$$m(N) = \frac{2\sqrt{\kappa_r \kappa_m}\gamma}{Ng^2 + \kappa\gamma} \tag{C.3}$$

$$a(N) = \frac{2\sqrt{\kappa_r \gamma}\sqrt{N}g}{Ng^2 + \kappa\gamma}. \tag{C.4}$$

Note that in the case of no coupling atom $a(N = 0) = 0$ as expected. Also, it should be pointed out that $|t(N)|^2$ decreases with increasing N as the coupled atom-cavity system is shifted further and further away from the frequency of the impinging photons if N is increased. The reason for this behavior is the coupling of the atoms to the cavity described theoretically by the Tavis-Cummings Hamiltonian (see section 2.1).

For the employed cavity and $N = 1$, the relevant parameters describing the coupled system are $g = 2\pi \times 7.8\,\text{MHz}$, $\gamma = 2\pi \times 3.0\,\text{MHz}$, $\kappa_r = 2\pi \times 2.29\,\text{MHz}$, $\kappa_t = 2\pi \times 0.09\,\text{MHz}$, $\kappa_m = 2\pi \times 0.13\,\text{MHz}$, and $\kappa = \kappa_r + \kappa_t + \kappa_m = 2\pi \times 2.51\,\text{MHz}$. The total rate κ is the sum of the loss rates through the outcoupling mirror κ_r, the other (high reflection) cavity mirror κ_t and the rate describing loss via absorption and scattering on the cavity mirrors κ_m. While κ_r is the desired decay channel of photons in the cavity, the rates κ_t and κ_m are undesired and further increase the total cavity linewidth.

In the following, two atoms trapped inside the cavity are considered. Employing optical pumping and global qubit rotations, the two atoms are initially prepared in a pure state of the form

$$|\psi_{\text{atom}}\rangle = a_0 \,|\uparrow\uparrow\rangle + a_1 \,|\uparrow\downarrow\rangle + a_2 \,|\downarrow\uparrow\rangle + a_3 \,|\downarrow\downarrow\rangle \tag{C.5}$$

where $|a_0|^2 + |a_1|^2 + |a_2|^2 + |a_3|^2 = 1$. If photons are injected onto the outcoupling cavity mirror, they will be transferred into one of the corresponding photonic states $|p_0\rangle$, $|p_1\rangle$, $|p_2\rangle$ or $|p_3\rangle$. These states are not orthogonal. However, they can be written in a basis of orthogonal states corresponding to the different photonic output modes of the system. These modes are the reflected mode $|p_r\rangle$, the mode describing scattering from the first/second atom $|p_{a1/a2}\rangle$, the mode describing scattering losses at a mirror $|p_m\rangle$, and the mode describing the transmission through the cavity $|p_t\rangle$. As an example, one can calculate the different components of these modes for the two-atom states $\{|\uparrow\uparrow\rangle, |\uparrow\downarrow\rangle, |\downarrow\uparrow\rangle, |\downarrow\downarrow\rangle\}$ that form a basis. These configurations are listed in table C.1 and the corresponding amplitudes for $|p_r\rangle$, $|p_t\rangle$, $|p_{a1/a2}\rangle$ and $|p_m\rangle$ are calculated according to equation 4.20. After impinging the photons onto the cavity, their state is entangled with the state of the atom. The combined atom-light state can be expressed as

$$|\psi_{\text{a,p}}\rangle = a_0 \,|p_0\rangle \,|\uparrow\uparrow\rangle + a_1 \,|p_1\rangle \,|\uparrow\downarrow\rangle + a_2 \,|p_2\rangle \,|\downarrow\uparrow\rangle + a_3 \,|p_3\rangle \,|\downarrow\downarrow\rangle = \sum_{i=0}^{3} a_i \,|p_i\rangle \,|a_i\rangle. \tag{C.6}$$

Table C.1.: Photon components after the reflection process.
For the four different input spin configurations of the two atoms, the respective photonic state is calculated. Note the minus sign in front of the $|p_r\rangle$ component for the scenario in which the atoms occupy the state $|\downarrow\downarrow\rangle$. This sign changes into plus for a non-vanishing number of coupling atoms in the cavity mode ($N > 0$). When no coupling atoms are present in the cavity mode ($N = 0$), the modes $|p_{a1}\rangle$ and $|p_{a2}\rangle$ are not populated as no scattering from an atom can occur.

N	Atomic state	Photonic state
0	$\|\downarrow\downarrow\rangle$	$\|p_3\rangle = -0.825\|p_r\rangle + 0.362\|p_t\rangle + 0.435\|p_m\rangle$
1	$\|\downarrow\uparrow\rangle$	$\|p_2\rangle = 0.783\|p_r\rangle + 0.043\|p_t\rangle + 0.619\|p_{a2}\rangle + 0.435\|p_m\rangle$
1	$\|\uparrow\downarrow\rangle$	$\|p_1\rangle = 0.783\|p_r\rangle + 0.043\|p_t\rangle + 0.619\|p_{a1}\rangle + 0.435\|p_m\rangle$
2	$\|\uparrow\uparrow\rangle$	$\|p_0\rangle = 0.884\|p_r\rangle + 0.023\|p_t\rangle + 0.329\|p_{a1}\rangle + 0.329\|p_{a2}\rangle + 0.028\|p_m\rangle$

Alternatively, it can be expressed as a density matrix of the form

$$\rho_{\mathrm{a,p}} = |\psi_{\mathrm{a,p}}\rangle\langle\psi_{\mathrm{a,p}}| = \sum_{i,j=0}^{3} a_{i,j} |a_i\rangle\langle a_j| \otimes |p_i\rangle\langle p_j|. \tag{C.7}$$

The photon can be transferred into different output modes. However, when it is destroyed it is traced out of the combined density matrix. What remains is a modified atomic density matrix that can be expressed as

$$\rho_{\mathrm{a}} = \mathrm{Tr}_{\mathrm{photon}}(\rho_{\mathrm{a,p}}) = \sum_{i,j=0}^{3} a_i a_j^* \langle p_j|p_i\rangle |a_i\rangle\langle a_j|. \tag{C.8}$$

This expression is almost the same as the atomic density matrix $|\psi_{\mathrm{atom}}\rangle\langle\psi_{\mathrm{atom}}|$ with the modification of the overlap factor $\langle p_j|p_i\rangle$ in front of the respective atomic states. To evaluate expression C.8, the scalar products of the form $\langle p_j|p_i\rangle$ need to be calculated. Table C.2 shows an evaluation of the different photonic factors corresponding to the respective atomic projectors $|a_i\rangle\langle a_j|$ with $i,j \in \{0,1,2,3\}$.

Employing the calculated expressions for $\langle p_j|p_i\rangle$ with the respective cavity parameters yields the matrix

$$\mathrm{M}_{\mathrm{gate}} = \sum_{i,i\in\{0,1,2,3\}} \langle p_j|p_i\rangle |a_i\rangle\langle a_j| = \begin{pmatrix} 1.000 & 0.905 & 0.905 & -0.717 \\ 0.905 & 1.000 & 0.640 & -0.622 \\ 0.905 & 0.640 & 1.000 & -0.622 \\ -0.717 & -0.622 & -0.622 & 1.000 \end{pmatrix} \tag{C.9}$$

in the basis $\{|\uparrow\uparrow\rangle, |\uparrow\downarrow\rangle, |\downarrow\uparrow\rangle |\downarrow\downarrow\rangle\}$. A density matrix describing the initial state of the two-atom pair in the cavity can be multiplied to this matrix with the elementwise Hadamard product to obtain the resulting density matrix if no heralding is applied. In the limit of vanishing losses, the matrix describing the gate process converges to

$$\mathrm{M}_{\mathrm{gate,\,ideal}} = \begin{pmatrix} 1.000 & 1.000 & 1.000 & -1.000 \\ 1.000 & 1.000 & 1.000 & -1.000 \\ 1.000 & 1.000 & 1.000 & -1.000 \\ -1.000 & -1.000 & -1.000 & 1.000 \end{pmatrix}. \tag{C.10}$$

Table C.2.: Atomic projectors and corresponding photonic correction factors.
The table shows the correction factors in the density matrix that arise when performing the trace operation over all possible photonic output modes of the system. These factors modify the density matrix defined in equation C.8 and result in a fidelity that will deviate from unity. The numerical values of the closed expressions in this table appear as the entries of the matrix M_{gate} defined in equation C.9.

$|a_i\rangle \langle a_j|$	Corresponding photonic factor$\langle p_j| p_i\rangle$
$|\uparrow\uparrow\rangle \langle\uparrow\uparrow|$	1
$|\uparrow\uparrow\rangle \langle\uparrow\downarrow|$	$r(2)r(1) + t(2)t(1) + 1/\sqrt{2}(a(2)a(1)) + m(2)m(1)$
$|\uparrow\uparrow\rangle \langle\downarrow\uparrow|$	$r(2)r(1) + t(2)t(1) + 1/\sqrt{2}(a(2)a(1)) + m(2)m(1)$
$|\uparrow\uparrow\rangle \langle\downarrow\downarrow|$	$r(2)r(0) + t(2)t(0) + m(2)m(0)$
$|\uparrow\downarrow\rangle \langle\uparrow\uparrow|$	$r(2)r(1) + t(2)t(1) + 1/\sqrt{2}(a(2)a(1)) + m(2)m(1)$
$|\uparrow\downarrow\rangle \langle\uparrow\downarrow|$	1
$|\uparrow\downarrow\rangle \langle\downarrow\uparrow|$	$r(1)r(1) + t(1)t(1) + m(1)m(1)$
$|\uparrow\downarrow\rangle \langle\downarrow\downarrow|$	$r(1)r(0) + t(1)t(0) + m(1)m(0)$
$|\downarrow\uparrow\rangle \langle\uparrow\uparrow|$	$r(2)r(1) + t(2)t(1) + 1/\sqrt{2}(a(2)a(1)) + m(2)m(1)$
$|\downarrow\uparrow\rangle \langle\uparrow\downarrow|$	$r(1)r(1) + t(1)t(1) + m(1)m(1)$
$|\downarrow\uparrow\rangle \langle\downarrow\uparrow|$	1
$|\downarrow\uparrow\rangle \langle\downarrow\downarrow|$	$r(1)r(0) + t(1)t(0) + m(1)m(0)$
$|\downarrow\downarrow\rangle \langle\uparrow\uparrow|$	$r(2)r(0) + t(2)t(0) + m(2)m(0)$
$|\downarrow\downarrow\rangle \langle\uparrow\downarrow|$	$r(1)r(0) + t(1)t(0) + m(1)m(0)$
$|\downarrow\downarrow\rangle \langle\downarrow\uparrow|$	$r(1)r(0) + t(1)t(0) + m(1)m(0)$
$|\downarrow\downarrow\rangle \langle\downarrow\downarrow|$	1

The negative signs on the off-diagonal elements in this matrix are reminiscent of the phase shift mechanism in the reflection process.

The fidelity of the experimentally generated states with the ideally expected states can now be calculated. This calculation is performed for an ideally expected Bell state $|\Phi^-\rangle = \frac{1}{\sqrt{2}}(|\uparrow\uparrow\rangle - |\downarrow\downarrow\rangle)$. Besides the scattering of photons into undesired loss modes, there is a series of additional effects that influence the fidelity of the generated states. These additional effects are imperfect state preparation (1%), imperfect matching of the impinging photons to the cavity mode (8%) and imperfect qubit rotations (3%).

For a calculation of the fidelity, the density matrix C.8 is admixed with erroneous contributions. When taking into account the imperfect mode matching, the density matrix after the reflection is given by $(1 - 0.92)\rho_{\text{non-interacting}} + 0.92 M_{\text{gate}} \rho_{\text{interacting}}$. Performing similar calculations for the other sources of error (state preparation and qubit rotation errors) yields the expected density matrix

$$\rho_{\exp} = \begin{pmatrix} 0.49 & -0.04 & -0.04 & -0.30 \\ -0.04 & 0.08 & -0.016 & -0.03 \\ -0.04 & -0.016 & 0.08 & -0.03 \\ -0.30 & -0.03 & -0.03 & 0.35 \end{pmatrix}. \tag{C.11}$$

This is the density matrix of the generated state before the measurement process. It has a fidelity of $F = \langle\Phi^-| \rho_{\exp} |\Phi^-\rangle = 72\%$ with the ideal $|\Phi^-\rangle$ state.

Table C.3.: Errors of the state detection process.
The table shows the populations measured in the double state detection protocol (see section 2.4.3.3) after a certain initial state (left column) was generated via optical pumping. The deviations of the desired populations from unity lead to an error associated to the state detection process.

Prepared state	$P_{\downarrow\downarrow}$	$P_{\downarrow\uparrow}$	$P_{\uparrow\downarrow}$	$P_{\uparrow\uparrow}$
$\lvert\downarrow\downarrow\rangle$	0.974	0.013	0.013	0.000
$\lvert\uparrow\downarrow\rangle\,/\,\lvert\downarrow\uparrow\rangle$	0.035	0.931/0.000	0.000/0.931	0.035
$\lvert\uparrow\uparrow\rangle$	0.000	0.015	0.015	0.970

The imperfect state detection process introduces another source of error. These errors were characterized in a separate measurement. In the characterization measurement, certain well defined two-atom states were prepared by optical pumping before the double state detection protocol (section 2.4.3.3) was applied. The outcome of the respective characterization measurement is listed in table C.3.

The fidelity of the measured state with the ideal Bell state $\lvert\Phi^-\rangle$ can be calculated by utilizing the populations of the expected density matrix ρ_{exp} before the detection process (C.11) and a subsequent evaluation of the expected outcome after the state detection measurement. For this, the respective measurements in table C.3 are employed. For a calculation of the fidelity, the parity signal including the state detection errors needs to be evaluated as well. The calculation shows that when including the state detection errors, this signal has an oscillation amplitude of 0.55. This value is slightly lower than the amplitude of 0.61 obtained from the parity oscillation signal from the density matrix ρ_{exp} before the state detection process. From the amplitude of 0.55, the measured off-diagonal element in the density matrix $\rho_{\uparrow\uparrow,\downarrow\downarrow}$ can be inferred. The calculation of the fidelity is performed with equation 4.8 and yields a value of 68%. Thus, a fidelity of 68% is expected in the case of a single-photon source and no heralding. This number is higher than the classical threshold of 50% and includes all experimental sources of error. As no heralding is applied, the efficiency of the scheme is unity and the atom-atom gate is deterministic in this case. The calculated fidelity of 68% is lower than the experimentally measured value of 76% where weak coherent pulses were used in combination with the postselection process.

The absence of postselection in the calculated case is responsible for the biggest contribution to the fidelity reduction. The cases in which the single photon is scattered into one of the loss modes are not suppressed as the heralding process is switched off. However, the efficiency of the gate is unity in this case. In a scenario when a high fidelity is needed, it is beneficial to sacrifice the high efficiency for a higher fidelity by postselecting the data on the cases in which the photon arrives at the detectors monitoring the reflection mode.

C.2. Expected State Fidelity Employing a Single-Photon Source With Heralding

To calculate the expected fidelity including the heralding process, the combined atom-photon density matrix C.7 needs to be projected onto the reflected photonic mode $|p_r\rangle$. The heralding process physically performs this projection operation on the initially generated density matrix $\rho_{a,p}$. The result can be expressed in the form

$$\langle p_r | \rho_{a,p} | p_r \rangle = \rho_a \circ \begin{pmatrix} r(2)^2 & r(2)r(1) & r(2)r(1) & r(2)r(0) \\ r(2)r(1) & r(1)^2 & r(1)^2 & r(1)r(0) \\ r(2)r(1) & r(1)^2 & r(1)^2 & r(1)r(0) \\ r(2)r(0) & r(1)r(0) & r(1)r(0) & r(0)^2 \end{pmatrix} \tag{C.12}$$

$$= \rho_a \circ \begin{pmatrix} 0.797 & 0.712 & 0.712 & -0.736 \\ 0.712 & 0.636 & 0.636 & -0.657 \\ 0.712 & 0.636 & 0.636 & -0.657 \\ -0.736 & -0.657 & -0.657 & 0.680 \end{pmatrix}. \tag{C.13}$$

In an analog calculation to the one in section C.1, the errors associated to mode matching, state preparation, rotation and detection can be included. A calculation of the expected fidelity with an ideal $|\Phi^-\rangle$ state yields a value of 82%.

This value is higher than in the scenario where the heralding was not used. The reason for this lies in the fact that the scattering events of the photons into the loss modes can be removed from the data. This is done at the expense of the gate efficiency. Due to the postselection process, the corresponding efficiency decreases from unity to a value of 32%. This efficiency is dominated by the finite cavity reflectivity on resonance (67%) and the detection efficiency of the employed single-photon detectors (55%). Nevertheless, it is 7.6 times higher than in the scenario in which weak coherent pulses were employed. Here, an efficiency of 4.2% was achieved at a mean photon number of $\bar{n} = 0.13$. A summary of the different possibilities for the postselection process is given in table 4.4.

D. List of Abbreviations

- AOD: Acousto-optical deflector
- AOM: Acousto-optical modulator
- BD: Beam dump
- BS: Beam splitter
- Cavity QED: Cavity quantum electrodynamics
- Cps: Counts per second
- EMCCD: Electron multiplying charge-coupled device
- EOM: Electro-optical modulator
- FORT: Far-off-resonance trap
- FSR: Free spectral range
- FWHM: Full width at half maximum
- MOT: Magneto-optical trap
- NA: Numerical aperture
- NPBS: Non-polarizing beam splitter
- PBS: Polarizing beam splitter
- PD: Photodiode
- QIP: Quantum information processing
- QKD: Quantum key distribution
- Qubit: Quantum bit
- SLM: Spatial light modulator
- SPD: Single-photon detector
- TDC: Time-to-digital converter
- vSTIRAP: Vacuum-stimulated Raman adiabatic passage

Bibliography

[1] Planck, M. *Zur Theorie des Gesetzes der Energieverteilung im Normalspectrum.* *Verhandlungen der deutschen physikalischen Gesellschaft* **2**, 237–245 (1900).

[2] Bohr, N. *On the constitution of atoms and molecules I.* *The London, Edinburgh, and Dublin Philosophical Magazine and Journal of Science* **26**, 1–25 (1913).

[3] De Broglie, L. *Recherches sur la théorie des quanta.* Ph.D. Thesis, Migration-université en cours d'affectation (1924).

[4] Einstein, A., Podolsky, B. & Rosen, N. *Can Quantum-Mechanical Description of Physical Reality Be Considered Complete?* *Physical Review* **47**, 777–780 (1935).

[5] Heisenberg, W. *Über den anschaulichen Inhalt der quantentheoretischen Kinematik und Mechanik.* *Zeitschrift für Physik* **43**, 172–198 (1927).

[6] Schrödinger, E. *Die gegenwärtige Situation in der Quantenmechanik.* *Die Naturwissenschaften* **23**, 807–812 (1935).

[7] Schrödinger, E. *Are there quantum jumps? Part II.* *The British Journal for the Philosophy of science* **III**, 233–242 (1952).

[8] Maiman, T. H. *Stimulated Optical Radiation in Ruby.* *Nature* **187**, 493–494 (1960).

[9] Neuhauser, W., Hohenstatt, M., Toschek, P. E. & Dehmelt, H. *Localized visible* Ba^+ *mono-ion oscillator.* *Physical Review A* **22**, 1137–1140 (1980).

[10] Wineland, D. J. *Nobel Lecture: Superposition, entanglement, and raising Schrödinger's cat.* *Reviews of Modern Physics* **85**, 1103–1114 (2013).

[11] Sauter, T., Neuhauser, W., Blatt, R. & Toschek, P. E. *Observation of Quantum Jumps.* *Physical Review Letters* **57**, 1696–1698 (1986).

[12] Bergquist, J. C., Hulet, R. G., Itano, W. M. & Wineland, D. J. *Observation of Quantum Jumps in a Single Atom.* *Physical Review Letters* **57**, 1699–1702 (1986).

[13] Haroche, S. *Nobel Lecture: Controlling photons in a box and exploring the quantum to classical boundary.* *Reviews of Modern Physics* **85**, 1083–1102 (2013).

[14] Rempe, G., Walther, H. & Klein, N. *Observation of quantum collapse and revival in a one-atom maser.* *Physical Review Letters* **58**, 353–356 (1987).

[15] Brune, M., Hagley, E., Dreyer, J., Maître, X., Maali, A., Wunderlich, C., Raimond, J. M. & Haroche, S. *Observing the Progressive Decoherence of the "Meter" in a Quantum Measurement.* *Physical Review Letters* **77**, 4887–4890 (1996).

[16] Lett, P. D., Watts, R. N., Westbrook, C. I., Phillips, W. D., Gould, P. L. & Metcalf, H. J. *Observation of Atoms Laser Cooled below the Doppler Limit. Physical Review Letters* **61**, 169–172 (1988).

[17] Chu, S. *Nobel Lecture: The manipulation of neutral particles. Reviews of Modern Physics* **70**, 685–706 (1998).

[18] Cohen-Tannoudji, C. N. *Nobel Lecture: Manipulating atoms with photons. Reviews of Modern Physics* **70**, 707–719 (1998).

[19] Phillips, W. D. *Nobel Lecture: Laser cooling and trapping of neutral atoms. Reviews of Modern Physics* **70**, 721–741 (1998).

[20] Nußmann, S., Murr, K., Hijlkema, M., Weber, B., Kuhn, A. & Rempe, G. *Vacuum-stimulated cooling of single atoms in three dimensions. Nature Physics* **1**, 122–125 (2005).

[21] Feynman, R. P. *Simulating physics with computers. International journal of theoretical physics* **21**, 467–488 (1982).

[22] Deutsch, D. *Quantum theory, the Church–Turing principle and the universal quantum computer. Proceedings of the Royal Society of London. A. Mathematical and Physical Sciences* **400**, 97–117 (1985).

[23] Shor, P. W. *Polynomial-time algorithms for prime factorization and discrete logarithms on a quantum computer. SIAM review* **41**, 303–332 (1999).

[24] Grover, L. K. *Quantum Computers Can Search Arbitrarily Large Databases by a Single Query. Physical Review Letters* **79**, 4709–4712 (1997).

[25] Cirac, J. & Zoller, P. *Quantum Computations with Cold Trapped Ions. Physical Review Letters* **74**, 4091–4094 (1995).

[26] Sørensen, A. & Mølmer, K. *Quantum Computation with Ions in Thermal Motion. Physical Review Letters* **82**, 1971–1974 (1999).

[27] Monroe, C., Meekhof, D. M., King, B. E., Itano, W. M. & Wineland, D. J. *Demonstration of a Fundamental Quantum Logic Gate. Physical Review Letters* **75**, 4714–4717 (1995).

[28] Schmidt-Kaler, F., Häffner, H., Riebe, M., Gulde, S., Lancaster, G. P., Deuschle, T., Becher, C., Roos, C. F., Eschner, J. & Blatt, R. *Realization of the Cirac–Zoller controlled-NOT quantum gate. Nature* **422**, 408–411 (2003).

[29] Leibfried, D. *et al. Experimental demonstration of a robust, high-fidelity geometric two ion-qubit phase gate. Nature* **422**, 412–415 (2003).

[30] Debnath, S., Linke, N. M., Figgatt, C., Landsman, K. A., Wright, K. & Monroe, C. *Demonstration of a small programmable quantum computer with atomic qubits. Nature* **536**, 63–66 (2016).

[31] Yamamoto, T., Pashkin, Y. A., Astafiev, O., Nakamura, Y. & Tsai, J.-S. *Demonstration of conditional gate operation using superconducting charge qubits. Nature* **425**, 941–944 (2003).

[32] Devoret, M. H. & Schoelkopf, R. J. *Superconducting circuits for quantum information: an outlook. Science* **339**, 1169–1174 (2013).

[33] O'Brien, J. L., Pryde, G. J., White, A. G., Ralph, T. C. & Branning, D. *Demonstration of an all-optical quantum controlled-NOT gate. Nature* **426**, 264–267 (2003).

[34] Kok, P., Munro, W. J., Nemoto, K., Ralph, T. C., Dowling, J. P. & Milburn, G. J. *Linear optical quantum computing with photonic qubits. Reviews of Modern Physics* **79**, 135–174 (2007).

[35] Hacker, B., Welte, S., Rempe, G. & Ritter, S. *A photon-photon quantum gate based on a single atom in an optical resonator. Nature* **536**, 193–196 (2016).

[36] Ritter, S., Hacker, B., Welte, S. & Rempe, G. *Recheneinheit für zwei Photonen. Physik in unserer Zeit* **47**, 268–269 (2016).

[37] Tiarks, D., Schmidt-Eberle, S., Stolz, T., Rempe, G. & Dürr, S. *A photon-photon quantum gate based on Rydberg interactions. Nature Physics* **15**, 124–126 (2019).

[38] Van der Sar, T., Wang, Z., Blok, M., Bernien, H., Taminiau, T., Toyli, D., Lidar, D., Awschalom, D., Hanson, R. & Dobrovitski, V. *Decoherence-protected quantum gates for a hybrid solid-state spin register. Nature* **484**, 82–86 (2012).

[39] Isenhower, L., Urban, E., Zhang, X. L., Gill, A. T., Henage, T., Johnson, T. A., Walker, T. G. & Saffman, M. *Demonstration of a Neutral Atom Controlled-NOT Quantum Gate. Physical Review Letters* **104**, 010503 (2010).

[40] Saffman, M., Walker, T. G. & Mølmer, K. *Quantum information with Rydberg atoms. Reviews of Modern Physics* **82**, 2313–2363 (2010).

[41] DiVincenzo, D. P. *The physical implementation of quantum computation. Fortschritte der Physik: Progress of Physics* **48**, 771–783 (2000).

[42] Welte, S., Hacker, B., Daiss, S., Ritter, S. & Rempe, G. *Cavity Carving of Atomic Bell States. Physical Review Letters* **118**, 210503 (2017).

[43] Welte, S., Hacker, B., Daiss, S., Ritter, S. & Rempe, G. *Photon-Mediated Quantum Gate between Two Neutral Atoms in an Optical Cavity. Physical Review X* **8**, 011018 (2018).

[44] Neuzner, A. *Resonance Fluorescence of an Atom Pair in an Optical Resonator.* Ph.D. Thesis, Max-Planck-Institut für Quantenoptik / Technische Universität München (2016).

[45] Ritter, S., Nölleke, C., Hahn, C., Reiserer, A., Neuzner, A., Uphoff, M., Mücke, M., Figueroa, E., Bochmann, J. & Rempe, G. *An elementary quantum network of single atoms in optical cavities. Nature* **484**, 195–200 (2012).

[46] Kalb, N., Reiserer, A., Ritter, S. & Rempe, G. *Heralded Storage of a Photonic Quantum Bit in a Single Atom. Physical Review Letters* **114**, 220501 (2015).

[47] Cirac, J. I., Zoller, P., Kimble, H. J. & Mabuchi, H. *Quantum State Transfer and Entanglement Distribution among Distant Nodes in a Quantum Network. Physical Review Letters* **78**, 3221–3224 (1997).

[48] Gisin, N., Ribordy, G., Tittel, W. & Zbinden, H. *Quantum cryptography. Reviews of Modern Physics* **74**, 145–195 (2002).

[49] Duan, L.-M., Lukin, M. D., Cirac, J. I. & Zoller, P. *Long-distance quantum communication with atomic ensembles and linear optics. Nature* **414**, 413–418 (2001).

[50] Nölleke, C., Neuzner, A., Reiserer, A., Hahn, C., Rempe, G. & Ritter, S. *Efficient Teleportation Between Remote Single-Atom Quantum Memories. Physical Review Letters* **110**, 140403 (2013).

[51] Buhrman, H. & Röhrig, H. Distributed quantum computing. In *International Symposium on Mathematical Foundations of Computer Science*, 1–20 (Springer, Berlin, Heidelberg, 2003).

[52] Monroe, C., Raussendorf, R., Ruthven, A., Brown, K. R., Maunz, P., Duan, L.-M. & Kim, J. *Large-scale modular quantum-computer architecture with atomic memory and photonic interconnects. Physical Review A* **89**, 022317 (2014).

[53] Brown, K. R., Kim, J. & Monroe, C. *Co-designing a scalable quantum computer with trapped atomic ions. npj Quantum Information* **2**, 16034 (2016).

[54] Kielpinski, D., Monroe, C. & Wineland, D. J. *Architecture for a large-scale ion-trap quantum computer. Nature* **417**, 709–711 (2002).

[55] Kimble, H. J. *The quantum internet. Nature* **453**, 1023–1030 (2008).

[56] Yin, J. *et al. Satellite-based entanglement distribution over 1200 kilometers. Science* **356**, 1140–1144 (2017).

[57] Liao, S.-K. *et al. Satellite-to-ground quantum key distribution. Nature* **549**, 43–47 (2017).

[58] Wehner, S., Elkouss, D. & Hanson, R. *Quantum internet: A vision for the road ahead. Science* **362**, eaam9288 (2018).

[59] Courtland, R. *China's 2,000-km quantum link is almost complete. IEEE Spectrum* **53**, 11–12 (2016).

[60] Delteil, A., Sun, Z., Gao, W.-b., Togan, E., Faelt, S. & Imamoğlu, A. *Generation of heralded entanglement between distant hole spins. Nature Physics* **12**, 218–223 (2016).

[61] Bouwmeester, D., Pan, J.-W., Mattle, K., Eibl, M., Weinfurter, H. & Zeilinger, A. *Experimental quantum teleportation. Nature* **390**, 575–579 (1997).

[62] Briegel, H. J., Dür, W., Cirac, J. I. & Zoller, P. *Quantum Repeaters: The Role of Imperfect Local Operations in Quantum Communication. Physical Review Letters* **81**, 5932–5935 (1998).

[63] Luong, D., Jiang, L., Kim, J. & Lütkenhaus, N. *Overcoming lossy channel bounds using a single quantum repeater node. Applied Physics B* **122**, 96 (2016).

[64] Körber, M., Morin, O., Langenfeld, S., Neuzner, A., Ritter, S. & Rempe, G. *Decoherence-protected memory for a single-photon qubit. Nature Photonics* **12**, 18–21 (2018).

[65] Bernien, H. *et al. Heralded entanglement between solid-state qubits separated by three metres. Nature* **497**, 86–90 (2013).

[66] Hensen, B. *et al. Loophole-free Bell inequality violation using electron spins separated by 1.3 kilometres. Nature* **526**, 682–686 (2015).

[67] Lodahl, P. *Quantum-dot based photonic quantum networks. Quantum Science and Technology* **3**, 013001 (2017).

[68] Reiserer, A. & Rempe, G. *Cavity-based quantum networks with single atoms and optical photons. Reviews of Modern Physics* **87**, 1379–1418 (2015).

[69] Reiserer, A., Kalb, N., Rempe, G. & Ritter, S. *A quantum gate between a flying optical photon and a single trapped atom. Nature* **508**, 237–240 (2014).

[70] Bechler, O. *et al. A passive photon-atom qubit swap operation. Nature Physics* **14**, 996–1000 (2018).

[71] Shomroni, I., Rosenblum, S., Lovsky, Y., Bechler, O., Guendelman, G. & Dayan, B. *All-optical routing of single photons by a one-atom switch controlled by a single photon. Science* **345**, 903–906 (2014).

[72] Rosenblum, S., Bechler, O., Shomroni, I., Lovsky, Y., Guendelman, G. & Dayan, B. *Extraction of a single photon from an optical pulse. Nature Photonics* **10**, 19–22 (2016).

[73] Wootters, W. K. & Zurek, W. H. *A single quantum cannot be cloned. Nature* **299**, 802–803 (1982).

[74] Uphoff, M., Brekenfeld, M., Rempe, G. & Ritter, S. *An integrated quantum repeater at telecom wavelength with single atoms in optical fiber cavities. Applied Physics B* **122**, 46 (2016).

[75] Duan, L.-M., Wang, B. & Kimble, H. J. *Robust quantum gates on neutral atoms with cavity-assisted photon scattering. Physical Review A* **72**, 032333 (2005).

[76] Lin, X.-M., Zhou, Z.-W., Ye, M.-Y., Xiao, Y.-F. & Guo, G.-C. *One-step implementation of a multiqubit controlled-phase-flip gate. Physical Review A* **73**, 012323 (2006).

[77] Casabone, B., Stute, A., Friebe, K., Brandstätter, B., Schüppert, K., Blatt, R. & Northup, T. E. *Heralded Entanglement of Two Ions in an Optical Cavity. Physical Review Letters* **111**, 100505 (2013).

[78] Casabone, B., Friebe, K., Brandstätter, B., Schüppert, K., Blatt, R. & Northup, T. E. *Enhanced Quantum Interface with Collective Ion-Cavity Coupling. Physical Review Letters* **114**, 023602 (2015).

[79] Majer, J. *et al. Coupling superconducting qubits via a cavity bus. Nature* **449**, 443–447 (2007).

[80] Sørensen, A. S. & Mølmer, K. *Probabilistic Generation of Entanglement in Optical Cavities. Physical Review Letters* **90**, 127903 (2003).

[81] Jaynes, E. T. & Cummings, F. W. *Comparison of quantum and semiclassical radiation theories with application to the beam maser. Proceedings of the IEEE* **51**, 89–109 (1963).

[82] Birnbaum, K. M., Boca, A., Miller, R., Boozer, A. D., Northup, T. E. & Kimble, H. J. *Photon blockade in an optical cavity with one trapped atom. Nature* **436**, 87–90 (2005).

[83] Kubanek, A., Ourjoumtsev, A., Schuster, I., Koch, M., Pinkse, P. W. H., Murr, K. & Rempe, G. *Two-Photon Gateway in One-Atom Cavity Quantum Electrodynamics. Physical Review Letters* **101**, 203602 (2008).

[84] Hamsen, C., Tolazzi, K. N., Wilk, T. & Rempe, G. *Two-Photon Blockade in an Atom-Driven Cavity QED System. Physical Review Letters* **118**, 133604 (2017).

[85] Tavis, M. & Cummings, F. W. *Exact Solution for an N-Molecule—Radiation-Field Hamiltonian. Physical Review* **170**, 379–384 (1968).

[86] Neuzner, A., Körber, M., Morin, O., Ritter, S. & Rempe, G. *Interference and dynamics of light from a distance-controlled atom pair in an optical cavity. Nature Photonics* **10**, 303–306 (2016).

[87] Reimann, R., Alt, W., Kampschulte, T., Macha, T., Ratschbacher, L., Thau, N., Yoon, S. & Meschede, D. *Cavity-modified collective Rayleigh scattering of two atoms. Physical Review Letters* **114**, 023601 (2015).

[88] Nußmann, S. *Kühlen und Positionieren eines Atoms in einem optischen Resonator.* Ph.D. Thesis, Max-Planck-Institut für Quantenoptik / Technische Universität München (2006).

[89] Drever, R. W. P., Hall, J. L., Kowalski, F. V., Hough, J., Ford, G. M., Munley, A. J. & Ward, H. *Laser phase and frequency stabilization using an optical resonator. Applied Physics B: Lasers and Optics* **31**, 97–105 (1983).

[90] Hohmann, L. *Using optical fibre cavities to create multi-atom entanglement by quantum zeno dynamics.* Ph.D. Thesis, l'École Normale Supérieure (2015).

[91] Dür, W., Vidal, G. & Cirac, J. I. *Three qubits can be entangled in two inequivalent ways. Physical Review A* **62**, 062314 (2000).

[92] Steck, D. A. Rubidium 87 D line data (2001).

[93] Reiserer, A. *A controlled phase gate between a single atom and an optical photon.* Ph.D. Thesis, Max-Planck-Institut für Quantenoptik / Technische Universität München (2014).

[94] Hacker, B. *Atom-cavity based photonic quantum information processing.* Ph.D. Thesis, Max-Planck-Institut für Quantenoptik / Technische Universität München (2019).

[95] Nölleke, C. *Quantum state transfer between remote single atoms.* Ph.D. Thesis, Max-Planck-Institut für Quantenoptik / Technische Universität München (2013).

[96] Specht, H. P. *Einzelatom-Quantenspeicher für Polarisations-Qubits.* Ph.D. Thesis, Max-Planck-Institut für Quantenoptik / Technische Universität München (2010).

[97] Grimm, R., Weidemüller, M. & Ovchinnikov, Y. B. *Optical dipole traps for neutral atoms. Advances in Atomic, Molecular and Optical Physics* **42**, 95–170 (2000).

[98] Reiserer, A., Nölleke, C., Ritter, S. & Rempe, G. *Ground-State Cooling of a Single Atom at the Center of an Optical Cavity. Physical Review Letters* **110**, 223003 (2013).

[99] Nußmann, S., Murr, K., Hijlkema, M., Weber, B., Kuhn, A. & Rempe, G. *Vacuum-stimulated cooling of single atoms in three dimensions. Nature Physics* **1**, 122–125 (2005).

[100] Uphoff, M. *State manipulation of single atoms in an optical cavity.* Diploma Thesis, Max-Planck-Institut für Quantenoptik / Technische Universität München (2010).

[101] Reiserer, A., Ritter, S. & Rempe, G. *Nondestructive detection of an optical photon. Science* **342**, 1349–1351 (2013).

[102] Gehr, R., Volz, J., Dubois, G., Steinmetz, T., Colombe, Y., Lev, B. L., Long, R., Estève, J. & Reichel, J. *Cavity-Based Single Atom Preparation and High-Fidelity Hyperfine State Readout. Physical Review Letters* **104**, 203602 (2010).

[103] Bochmann, J., Mücke, M., Guhl, C., Ritter, S., Rempe, G. & Moehring, D. L. *Lossless State Detection of Single Neutral Atoms. Physical Review Letters* **104**, 203601 (2010).

[104] Purcell, E. M., Torrey, H. C. & Pound, R. V. *Resonance Absorption by Nuclear Magnetic Moments in a Solid. Physical Review* **69**, 37–38 (1946).

[105] Tiecke, T., Thompson, J. D., de Leon, N. P., Liu, L., Vuletić, V. & Lukin, M. D. *Nanophotonic quantum phase switch with a single atom. Nature* **508**, 241–244 (2014).

[106] Volz, J., Scheucher, M., Junge, C. & Rauschenbeutel, A. *Nonlinear π phase shift for single fibre-guided photons interacting with a single resonator-enhanced atom. Nature Photonics* **8**, 965–970 (2014).

[107] Kono, S., Koshino, K., Tabuchi, Y., Noguchi, A. & Nakamura, Y. *Quantum non-demolition detection of an itinerant microwave photon. Nature Physics* **14**, 546–549 (2018).

[108] Besse, J.-C., Gasparinetti, S., Collodo, M. C., Walter, T., Kurpiers, P., Pechal, M., Eichler, C. & Wallraff, A. *Single-Shot Quantum Nondemolition Detection of Individual Itinerant Microwave Photons. Physical Review X* **8**, 021003 (2018).

[109] Duan, L.-M. & Kimble, H. J. *Scalable Photonic Quantum Computation through Cavity-Assisted Interactions. Physical Review Letters* **92**, 127902 (2004).

[110] Wang, B. & Duan, L.-M. *Engineering superpositions of coherent states in coherent optical pulses through cavity-assisted interaction. Physical Review A* **72**, 022320 (2005).

[111] Hacker, B., Welte, S., Daiss, S., Shaukat, A., Ritter, S., Li, L. & Rempe, G. *Deterministic creation of entangled atom-light Schrödinger-cat states. Nature Photonics* **13**, 110–115 (2019).

[112] Walls, D. & Milburn, G. J. *Quantum Optics* (Springer Berlin Heidelberg, 2008).

[113] Kuhn, A. Cavity Induced Interfacing of Atoms and Light. In *Engineering the Atom-Photon Interaction*, 3–38 (Springer, 2015).

[114] Freedman, S. J. & Clauser, J. F. *Experimental Test of Local Hidden-Variable Theories. Physical Review Letters* **28**, 938–941 (1972).

[115] Aspect, A., Dalibard, J. & Roger, G. *Experimental Test of Bell's Inequalities Using Time-Varying Analyzers. Physical Review Letters* **49**, 1804–1807 (1982).

[116] Wang, X.-L. *et al. Experimental Ten-Photon Entanglement. Physical Review Letters* **117**, 210502 (2016).

[117] Turchette, Q. A., Wood, C. S., King, B. E., Myatt, C. J., Leibfried, D., Itano, W. M., Monroe, C. & Wineland, D. J. *Deterministic Entanglement of Two Trapped Ions. Physical Review Letters* **81**, 3631–3634 (1998).

[118] Sackett, C. A. *et al. Experimental entanglement of four particles. Nature* **404**, 256–259 (2000).

[119] Moehring, D. L., Maunz, P., Olmschenk, S., Younge, K. C., Matsukevich, D. N., Duan, L.-M. & Monroe, C. *Entanglement of single-atom quantum bits at a distance. Nature* **449**, 68–71 (2007).

[120] Lin, Y., Gaebler, J., Reiter, F., Tan, T. R., Bowler, R., Sørensen, A., Leibfried, D. & Wineland, D. J. *Dissipative production of a maximally entangled steady state of two quantum bits. Nature* **504**, 415–418 (2013).

[121] Hagley, E., Maître, X., Nogues, G., Wunderlich, C., Brune, M., Raimond, J. M. & Haroche, S. *Generation of Einstein-Podolsky-Rosen Pairs of Atoms. Physical Review Letters* **79**, 1–5 (1997).

[122] Wilk, T., Gaëtan, A., Evellin, C., Wolters, J., Miroshnychenko, Y., Grangier, P. & Browaeys, A. *Entanglement of Two Individual Neutral Atoms Using Rydberg Blockade. Physical Review Letters* **104**, 010502 (2010).

[123] Levine, H., Keesling, A., Omran, A., Bernien, H., Schwartz, S., Zibrov, A. S., Endres, M., Greiner, M., Vuletić, V. & Lukin, M. D. *High-Fidelity Control and Entanglement of Rydberg-Atom Qubits. Physical Review Letters* **121**, 123603 (2018).

[124] Kaufman, A., Lester, B., Foss-Feig, M., Wall, M., Rey, A. & Regal, C. *Entangling two transportable neutral atoms via local spin exchange. Nature* **527**, 208–211 (2015).

[125] Steffen, M., Ansmann, M., Bialczak, R. C., Katz, N., Lucero, E., McDermott, R., Neeley, M., Weig, E. M., Cleland, A. N. & Martinis, J. M. *Measurement of the entanglement of two superconducting qubits via state tomography. Science* **313**, 1423–1425 (2006).

[126] Pfaff, W., Taminiau, T. H., Robledo, L., Bernien, H., Markham, M., Twitchen, D. J. & Hanson, R. *Demonstration of entanglement-by-measurement of solid-state qubits. Nature Physics* **9**, 29–33 (2013).

[127] Kurpiers, P. *et al. Deterministic quantum state transfer and remote entanglement using microwave photons. Nature* **558**, 264–267 (2018).

[128] Axline, C. J. *et al. On-demand quantum state transfer and entanglement between remote microwave cavity memories. Nature Physics* **14**, 705–710 (2018).

[129] Humphreys, P. C., Kalb, N., Morits, J. P., Schouten, R. N., Vermeulen, R. F., Twitchen, D. J., Markham, M. & Hanson, R. *Deterministic delivery of remote entanglement on a quantum network. Nature* **558**, 268–273 (2018).

[130] Moehring, D. L., Madsen, M. J., Blinov, B. B. & Monroe, C. *Experimental Bell Inequality Violation with an Atom and a Photon. Physical Review Letters* **93**, 090410 (2004).

[131] Wilk, T., Webster, S. C., Kuhn, A. & Rempe, G. *Single-atom single-photon quantum interface. Science* **317**, 488–490 (2007).

[132] Moehring, D. L., Madsen, M. J., Younge, K. C., Kohn, J., Maunz, P., Duan, L.-M., Monroe, C. & Blinov, B. B. *Quantum networking with photons and trapped atoms (Invited). J. Opt. Soc. Am. B* **24**, 300–315 (2007).

[133] Julsgaard, B., Kozhekin, A. & Polzik, E. S. *Experimental long-lived entanglement of two macroscopic objects. Nature* **413**, 400–403 (2001).

[134] Chen, W., Hu, J., Duan, Y., Braverman, B., Zhang, H. & Vuletić, V. *Carving Complex Many-Atom Entangled States by Single-Photon Detection. Physical Review Letters* **115**, 250502 (2015).

[135] Nielsen, M. A. & Chuang, I. L. *Quantum Computation and Quantum Information* (Cambridge University Press, 2000), 1 edn.

[136] Wootters, W. K. *Entanglement of Formation of an Arbitrary State of Two Qubits. Physical Review Letters* **80**, 2245–2248 (1998).

[137] Husimi, K. *Some formal properties of the density matrix. Proceedings of the Physico-Mathematical Society of Japan. 3rd Series* **22**, 264–314 (1940).

[138] Agarwal, G. S. *State reconstruction for a collection of two-level systems. Physical Review A* **57**, 671–673 (1998).

[139] Cahill, K. E. & Glauber, R. J. *Density Operators and Quasiprobability Distributions. Physical Review* **177**, 1882–1902 (1969).

[140] Haas, F., Volz, J., Gehr, R., Reichel, J. & Estève, J. *Entangled states of more than 40 atoms in an optical fiber cavity. Science* **344**, 180–183 (2014).

[141] Radcliffe, J. *Some properties of coherent spin states. Journal of Physics A: General Physics* **4**, 313 (1971).

[142] Zhang, W.-M., Feng, D. H. & Gilmore, R. *Coherent states: Theory and some applications. Reviews of Modern Physics* **62**, 867–927 (1990).

[143] Ospelkaus, C., Warring, U., Colombe, Y., Brown, K., Amini, J., Leibfried, D. & Wineland, D. *Microwave quantum logic gates for trapped ions. Nature* **476**, 181–184 (2011).

[144] Thompson, R. J., Rempe, G. & Kimble, H. J. *Observation of normal-mode splitting for an atom in an optical cavity. Physical Review Letters* **68**, 1132–1135 (1992).

[145] Dotsenko, I., Alt, W., Kuhr, S., Schrader, D., Müller, M., Miroshnychenko, Y., Gomer, V., Rauschenbeutel, A. & Meschede, D. *Application of electro-optically generated light fields for Raman spectroscopy of trapped cesium atoms. Applied Physics B* **78**, 711–717 (2004).

[146] Duan, L.-M. & Kimble, H. J. *Scalable Photonic Quantum Computation through Cavity-Assisted Interactions. Physical Review Letters* **92**, 127902 (2004).

[147] Uphoff, M., Brekenfeld, M., Rempe, G. & Ritter, S. *Frequency splitting of polarization eigenmodes in microscopic Fabry–Perot cavities. New Journal of Physics* **17**, 013053 (2015).

[148] Barontini, G., Hohmann, L., Haas, F., Estève, J. & Reichel, J. *Deterministic generation of multiparticle entanglement by quantum Zeno dynamics. Science* **349**, 1317–1321 (2015).

[149] McConnell, R., Zhang, H., Hu, J., Ćuk, S. & Vuletić, V. *Entanglement with negative Wigner function of almost 3,000 atoms heralded by one photon. Nature* **519**, 439–442 (2015).

[150] Řeháček, J., Hradil, Z. & Ježek, M. *Iterative algorithm for reconstruction of entangled states. Physical Review A* **63**, 040303 (2001).

[151] Lvovsky, A. *Iterative maximum-likelihood reconstruction in quantum homodyne tomography. Journal of Optics B: Quantum and Semiclassical Optics* **6**, S556 (2004).

[152] Haas, F. *Création d'états intriqués d'un ensemble d'atomes dans une cavité optique.* Ph.D. Thesis, l'École Normale Supérieure (2014).

[153] Kwiat, P. G., Berglund, A. J., Altepeter, J. B. & White, A. G. *Experimental verification of decoherence-free subspaces. Science* **290**, 498–501 (2000).

[154] Northup, T. & Blatt, R. *Quantum information transfer using photons. Nature Photonics* **8**, 356–363 (2014).

[155] Wallraff, A., Schuster, D. I., Blais, A., Frunzio, L., Huang, R.-S., Majer, J., Kumar, S., Girvin, S. M. & Schoelkopf, R. J. *Strong coupling of a single photon to a superconducting qubit using circuit quantum electrodynamics. Nature* **431**, 162–167 (2004).

[156] Dousse, A., Lanco, L., Suffczyński, J., Semenova, E., Miard, A., Lemaître, A., Sagnes, I., Roblin, C., Bloch, J. & Senellart, P. *Controlled Light-Matter Coupling for a Single Quantum Dot Embedded in a Pillar Microcavity Using Far-Field Optical Lithography. Physical Review Letters* **101**, 267404 (2008).

[157] Russo, C. *et al. Raman spectroscopy of a single ion coupled to a high-finesse cavity. Applied Physics B* **95**, 205–212 (2009).

[158] Stute, A., Casabone, B., Brandstätter, B., Friebe, K., Northup, T. E. & Blatt, R. *Quantum-state transfer from an ion to a photon. Nature Photonics* **7**, 219–222 (2013).

[159] Kaupp, H., Deutsch, C., Chang, H.-C., Reichel, J., Hänsch, T. W. & Hunger, D. *Scaling laws of the cavity enhancement for nitrogen-vacancy centers in diamond. Physical Review A* **88**, 053812 (2013).

[160] Lodahl, P., Mahmoodian, S. & Stobbe, S. *Interfacing single photons and single quantum dots with photonic nanostructures. Reviews of Modern Physics* **87**, 347–400 (2015).

[161] Takahashi, H., Kassa, E., Christoforou, C. & Keller, M. *Strong coupling of a single ion to an optical cavity. arXiv preprint arXiv:1808.04031* (2018).

[162] Gallego, J., Alt, W., Macha, T., Martinez-Dorantes, M., Pandey, D. & Meschede, D. *Strong Purcell Effect on a Neutral Atom Trapped in an Open Fiber Cavity. Physical Review Letters* **121**, 173603 (2018).

[163] Poyatos, J. F., Cirac, J. I. & Zoller, P. *Complete Characterization of a Quantum Process: The Two-Bit Quantum Gate. Physical Review Letters* **78**, 390–393 (1997).

[164] Peres, A. *Separability Criterion for Density Matrices. Physical Review Letters* **77**, 1413–1415 (1996).

[165] Mücke, M., Bochmann, J., Hahn, C., Neuzner, A., Nölleke, C., Reiserer, A., Rempe, G. & Ritter, S. *Generation of single photons from an atom-cavity system. Physical Review A* **87**, 063805 (2013).

[166] Brakhane, S., Alt, W., Kampschulte, T., Martinez-Dorantes, M., Reimann, R., Yoon, S., Widera, A. & Meschede, D. *Bayesian feedback control of a two-atom spin-state in an atom-cavity system. Physical Review Letters* **109**, 173601 (2012).

[167] Kuhn, A. & Ljunggren, D. *Cavity-based single-photon sources. Contemporary Physics* **51**, 289–313 (2010).

[168] Daiss, S., Welte, S., Hacker, B., Li, L. & Rempe, G. *Single-Photon Distillation via a Photonic Parity Measurement Using Cavity QED. Physical Review Letters* **122**, 133603 (2019).

[169] Bennett, C. H. & Wiesner, S. J. *Communication via one- and two-particle operators on Einstein-Podolsky-Rosen states. Physical Review Letters* **69**, 2881–2884 (1992).

[170] Ashkin, A. *Trapping of Atoms by Resonance Radiation Pressure. Physical Review Letters* **40**, 729–732 (1978).

[171] Labuhn, H., Barredo, D., Ravets, S., De Léséleuc, S., Macrì, T., Lahaye, T. & Browaeys, A. *Tunable two-dimensional arrays of single Rydberg atoms for realizing quantum Ising models. Nature* **534**, 667–670 (2016).

[172] Barredo, D., De Léséleuc, S., Lienhard, V., Lahaye, T. & Browaeys, A. *An atom-by-atom assembler of defect-free arbitrary 2d atomic arrays. Science* **354**, 1021–1023 (2016).

[173] Endres, M., Bernien, H., Keesling, A., Levine, H., Anschuetz, E. R., Krajenbrink, A., Senko, C., Vuletic, V., Greiner, M. & Lukin, M. D. *Atom-by-atom assembly of defect-free one-dimensional cold atom arrays. Science* **354**, 1024–1027 (2016).

[174] Bernien, H. *et al. Probing many-body dynamics on a 51-atom quantum simulator. Nature* **551**, 579–584 (2017).

[175] Cooper, A., Covey, J. P., Madjarov, I. S., Porsev, S. G., Safronova, M. S. & Endres, M. *Alkaline-Earth Atoms in Optical Tweezers. Physical Review X* **8**, 041055 (2018).

[176] Barredo, D., Lienhard, V., de Léséleuc, S., Lahaye, T. & Browaeys, A. *Synthetic three-dimensional atomic structures assembled atom by atom. Nature* **561**, 79–82 (2018).

[177] Kaufman, A. M., Lester, B. J. & Regal, C. A. *Cooling a Single Atom in an Optical Tweezer to Its Quantum Ground State. Physical Review X* **2**, 041014 (2012).

[178] Borregaard, J., Kómár, P., Kessler, E. M., Sørensen, A. S. & Lukin, M. D. *Heralded Quantum Gates with Integrated Error Detection in Optical Cavities. Physical Review Letters* **114**, 110502 (2015).

[179] Borregaard, J., Kómár, P., Kessler, E. M., Lukin, M. D. & Sørensen, A. S. *Long-distance entanglement distribution using individual atoms in optical cavities. Physical Review A* **92**, 012307 (2015).

[180] Lukin, M. D., Fleischhauer, M., Cote, R., Duan, L. M., Jaksch, D., Cirac, J. I. & Zoller, P. *Dipole Blockade and Quantum Information Processing in Mesoscopic Atomic Ensembles. Physical Review Letters* **87**, 037901 (2001).

[181] Zeng, Y., Xu, P., He, X., Liu, Y., Liu, M., Wang, J., Papoular, D. J., Shlyapnikov, G. V. & Zhan, M. *Entangling Two Individual Atoms of Different Isotopes via Rydberg Blockade. Physical Review Letters* **119**, 160502 (2017).

[182] Cohen, I. & Mølmer, K. *Deterministic quantum network for distributed entanglement and quantum computation. Physical Review A* **98**, 030302 (2018).

[183] Xiao, Y.-F., Lin, X.-M., Gao, J., Yang, Y., Han, Z.-F. & Guo, G.-C. *Realizing quantum controlled phase flip through cavity QED. Physical Review A* **70**, 042314 (2004).

[184] Nadonly, T. *Automatic compensation of polarization drifts in an optical fiber.* Bachelor Thesis, Max-Planck-Institut für Quantenoptik / Ludwig-Maximilians-Universität München (2018).

[185] Hofmann, J., Krug, M., Ortegel, N., Gerard, L., Weber, M., Rosenfeld, W. & Weinfurter, H. *Heralded Entanglement Between Widely Separated Atoms. Science* **337**, 72–75 (2012).

[186] Rosenfeld, W., Burchardt, D., Garthoff, R., Redeker, K., Ortegel, N., Rau, M. & Weinfurter, H. *Event-Ready Bell Test Using Entangled Atoms Simultaneously Closing Detection and Locality Loopholes. Physical Review Letters* **119**, 010402 (2017).

[187] Steck, D. A. Rubidium 87 D Line Data (2015).

[188] *Semrock laser line filter LL01-780. www.semrock.com/FilterDetails.aspx?id=LL01-780-12.5* .

[189] *Semrock laser line filter LL01-785. www.semrock.com/FilterDetails.aspx?id=LL01-785-12.5* .

Acknowledgements